Multiphoton Flow Cytometry for Enhanced-Throughput Analysis and Sorting of Microtissues

By

David G. Buschke

A dissertation submitted in partial fulfillment of

the requirements for the degree of

Doctor of Philosophy

(Biomedical Engineering)

at the

UNIVERSITY OF WISCONSIN-MADISON

2012

Date of final oral examination: 12/11/12

The dissertation is approved by the following members of the Final Oral committee:

Brenda Ogle, Associate Professor, Biomedical Engineering
Naomi Chesler, Associate Professor, Biomedical Engineering
Kevin Eliceiri, Director, Laboratory for Optical and Computational Instrumentation
Gary Lyons, Professor, Cell and Regenerative Biology
William Murphy, Associate Professor, Biomedical Engineering
Justin Williams, Associate Professor, Biomedical Engineering

Dedication & Acknowledgements

I would first like to thank my advisor, Brenda Ogle, for all of her guidance, patience, passion and dedication throughout my time as a graduate student. For all of the time she has invested in making me a successful researcher, writer, speaker, and person, I will be forever in her debt. Next, I'd like to thank my co-advisor, Kevin Eliceiri, for his hard work and dedication to his job, his integral role in the success in this project, and always making time for me for troubleshooting or an idea session no matter how busy he was. I would also like to thank my other committee members, Justin Williams, William Murphy, Naomi Chesler, and Gary Lyons, all of whom have provided thoughtful ideas for this project at one time or another, have directly collaborated on this project and/or have been great teachers of mine. My lab mates have been great to me from day 1, helping me on projects, providing camaraderie, just being there to bounce ideas off of and celebrating accomplishments: I would especially like to thank Jayne Squirrell, for all the projects we have worked on together and all the lessons she has taught me, Nick Kouris, for being a great role model and friend, and Pedro Resto, for great discussions and his help with the design of our final flow cell.

I would not have arrived at this point in my life without tremendous support from my family and friends. My parents, Greg and Patti Buschke, have provided me with every opportunity in life to succeed and have taught me that hard work and a character can take you anywhere. My sisters, Tricia and Kristen, and my brother-in-law, Joel, have been there every step of the way, supporting me, providing advice and keeping me on the right path. And lastly, to my wife, Bonnie, for being there in the good times and the bad, and being the best friend anyone could ever ask for, I dedicate this work to you.

Much Love,

David G. Buschke

Table of Contents

List of Figures and Tables

List of Abbreviations

3D: Three-Dimensional
αMHC: alpha Myosin Heavy Chain
a.i.u.: Arbitrary Intensity Units
ATP: Adenosine-5'-triphosphate

BC: Background-Corrected
BMP-4: Bone Morphogenetic Protein 4
BSA: Bovine Serum Albumin

cTnT: Cardiac Troponin T

DAQ: Data Acquisition
DMEM: Dulbecco's Modified Eagle Medium

EBs: Embryoid Bodies
ESCs: Embryonic Stem Cells

FACS: Fluorescence-Activated Cell Sorting
FAD: Flavin Adenine Dinucleotide
FBS: Fetal Bovine Serum
FLIM: Fluorescence Lifetime Imaging Microscopy
FSB: Floating Stir Bar

GFP: Green Fluorescent Protein

HBSS: Hank's Buffered Salt Solution

iPSC: Induced Pluripotent Stem Cells

LaPSD: Large Particle Sorting Device
LCC: Live Cell-Corrected
LIF: Leukemia Inhibitory Factor
LOCI: Laboratory for Optical and Computational Instrumentation

MACS: Magnetic-Activated Cell Sorting
MPFC: Multiphoton Flow Cytometer
MPFE: Multiphoton Fluorescence Excitation
MPLSM: Multiphoton Laser Scanning Microscopy
MSCs: Mesenchymal Stem Cells

NIH: National Institutes of Health
NADH: Nicotinamide Adenine Dinucleotide

PAR-4: Prostate Apoptosis Response 4
PBS: Phosphate Buffered Saline
PCR: Polymerase Chain Reaction
PDMS: Polydimethylsiloxane
PVC: Polyvinyl Chloride

ROI: Region of Interest

SHG: Second-Harmonic Generation

CHAPTER 1
Introduction

1.1 Research Problem Description

The unique ability of stem cells to exist in multiple states (i.e., pluripotent, multipotent, mature) provides a powerful tool for developmental biology, pharmaceutical science and regenerative medicine. Ironically, this same property hinders rapid progress in these fields due to the current lack of experimental control to maintain stem cells or their progeny in a specified state. One primary challenge is defining and executing screening protocols that can non-invasively monitor the status (i.e., viability, proliferative capacity, functional competence) of a given population of cells. The complexity of such screening is amplified in biologically relevant three-dimensional constructs, where not only is accessing the cells for screening more difficult but the status of cells can be altered if they are removed from the construct for characterization [1-2]. In addition, certain characterization approaches, such as those involving antibody or peptide binding either require the use of fixed tissue or can alter stem cell state, thereby limiting clinical use [3-4]. Continued advances in stem cell research depend on the development of new technologies that meet the following design criteria: This instrument should A) avoid disaggregation to preserve the microenvironment and maintain cell viability, B) acquire an accurate measurement by quantifying a representative fraction of the volume, (C) avoid the use of exogenous labels so as not to influence phenotype and (D) allow sorting based on any measurement made on the system. The goal of this project is to develop an instrument that meets these criteria (summarized in **Figure 1.1**).

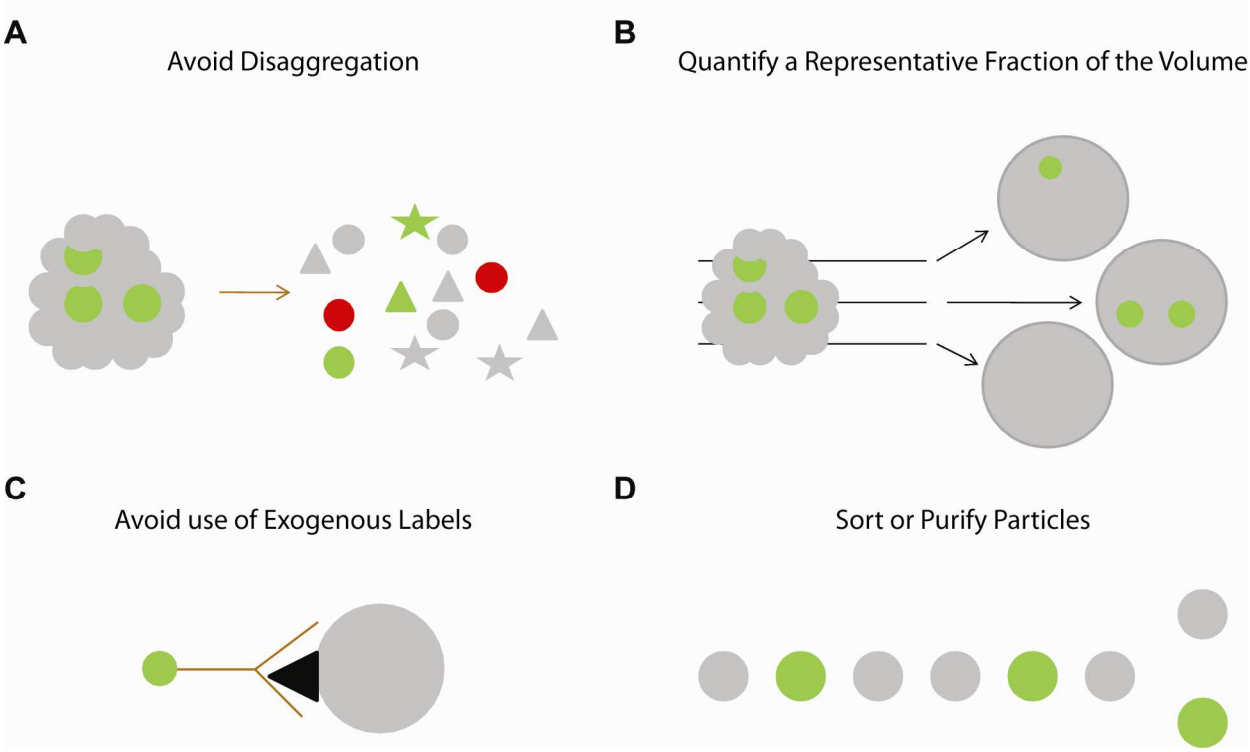

Figure 1.1 Schematic of ideal design criteria for analysis of 3-D microtissues. A) Must avoid disaggregation to preserve the microenvironment and maintain cell viability. B) Should acquire an accurate measurement by quantifying a representative fraction of the volume. C) Avoids the use of exogenous labels so as not to influence phenotype. D) Allows sorting based on any measurement made on the system.

1.2 Specific Objectives and Hypotheses

Specific Objective 1: To develop a proof of concept Multiphoton Flow Cytometry (MPFC) system. **Hypothesis. A novel optical arrangement including multiphoton excitation could be used to enhance the ability of flow cytometry systems to accurately and non-invasively probe cells in the interior of microtissues in an enhanced throughput fashion (thereby addressing design criteria A and B).** To test this hypothesis, a modular microfluidic device was developed to stream microtissues in a controlled manner past a point of optical interrogation (Chapter 3). The device was incorporated onto a Multiphoton Laser Scanning Microscope (MPLSM) and detection software was developed. Together, these components formed the basis for an instrument capable of measuring microtissue characteristics in an enhanced throughput fashion. The utility of the resultant system, named multiphoton flow cytometry (MPFC), was assessed by quantifying microtissue size and fluorescence intensity, and comparing results to those attained with conventional static imaging techniques [5].

Specific Objective 2: To sort multicellular entities based on characteristics detected using MPFC. **Hypothesis. A novel, microfluidic-based sorting mechanism can be incorporated into the MPFC design to purify populations of large particles (thereby addressing criterion D).** To test this hypothesis, several iterations of the 1st generation MPFC flow cell were developed, allowing sorting of large particles based on user-defined criteria. To identify the best iteration, designs were tested by sorting fluorescent beads. Assessment criteria were 1) purity of desired particles, 2) enrichment ratio, 3) accessibility and 4) ease of use (Chapter 4). The optimal large particle sorting device (LaPSD) was further validated by sorting fluorescently stained embryoid bodies (EBs) and assessing the viability and long-term function of cells of the EB [6].

Specific Objective 3: To use the MPFC system to non-invasively purify populations of microtissues and to assess the functional capacity of sorted populations. For final validation of the MPFC as both a research tool and to demonstrate potential for clinical transplantation, microtissues were sorted based on extrinsic and intrinsic fluorescent indicators of cell state. **Hypothesis. Purified populations of EBs, detected and sorted on the MPFC based on fluorescent indicators of size, cell phenotype and viability, will have higher percentages of cells adopting a cardiac phenotype (Chapters 5 & 6) than unsorted populations of EBs (thereby addressing criterion C)**. Conventional methods for assessing cell phenotype and function were performed to test this hypothesis [7].

CHAPTER 2
Background

2.1 Introduction to Flow Cytometry

Flow cytometry is a relatively mature, high-throughput biological and clinical technique used for characterizing large populations of single cells [8]. Unlike RNA and protein-based approaches (i.e., RNA or protein microarrays, reverse transcriptase-polymerase chain reaction, Western blot or ELISA), flow cytometry can be used to analyze intact cells, permitting the study of analyzed populations over time. A myriad of measurements can be rapidly made using flow cytometry systems including but not limited to cell count, viability, size, granularity, as well as DNA/RNA content, surface sugars and protein expression. Commercial flow cytometers consist of a fluidic delivery component that focuses a sample stream composed of single cells onto a light interrogation point within a flow cell (**Figure 2.1**). Principles of laminar flow allow for a buffered solution, commonly known as sheath fluid, to physically focus cells into a confined stream. This so-called hydrodynamic focusing effect is most commonly implemented with sheath fluid in commercial systems, but has recently been accomplished in micro-flow cytometry applications with electric fields [9-11] and acoustic waves [12-14]. Light excitation in commercial systems is typically supplied by mercury lamps, along with argon and krypton ion lasers. The incorporation of optical excitation filters increases the sensitivity and selectivity of the instrument by delivering light at a wavelength that caters to the excitation spectrum of the fluorophores being used. Following excitation, longer wavelength photons are emitted from the fluorophore and directed to specific detectors, typically photomultiplier tubes (PMTs), where they are amplified and digitized to an electric pulse that will be analyzed by the software. Emission filters and other spectral approaches are also used to further discriminate the fluorophores seen at detection. Many of these instruments include the capability of detecting other cellular parameters based exclusively on light scatter. Slightly deflected light, known as forward scatter, gives a measure of cell size, while light that is deflected perpendicular to the light source, or side-scatter, measures the granularity of a cell. Some modern instruments incorporate the ability to analyze up to 19 parameters simultaneously [15].

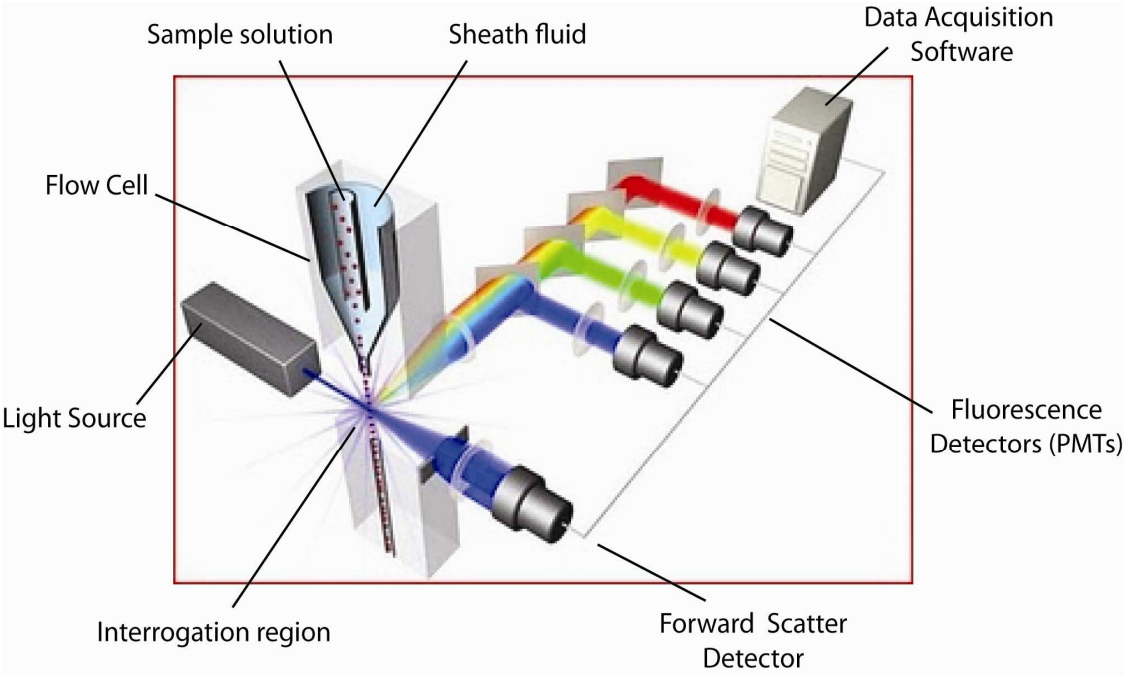

Figure 2.1 Schematic of a traditional flow cytometry system. Adapted from original artwork by Life Technologies (www.lifetechnologies.com).

2.2 Fluorescent Activated Cell Sorting of Single Cells (FACS)

One of the great advantages of flow cytometry is its unrivaled ability to sort cells based on the aforementioned cellular characteristics. Fluorescence-activated cell sorting (FACS) instruments accomplish sorting by creating uniformly sized droplets leaving the sample injection nozzle by way of an ultrasonic nozzle vibrator [16-17]. While in the nozzle (flow cell), each individual cell passes through the laser beam and is detected as a positive or negative event based on its expression of an associated fluorescent probe. If the cell is detected as a positive event, the droplet that is formed housing that cell is given a positive charge, whereas if no cell is present or a cell is deemed to be a negative event, a negative charge is given to the droplet. Those droplets then pass through an electric field which deflects the droplets based on their charge, effectively sorting cells based on fluorescence levels. Although very effective in commercial systems, this method has inherent limitations as particle sizes increase. Cell induced surface disturbances can alter the predictability of droplet formations and this effect is amplified as particle size increases [18]. In addition, the mass increase associated with large particles decreases the angle of deflection induced by the electric field and greatly increases the variability in droplet displacement [19]. Thus, charged-based droplet sorting is not a viable option for large particle sorting.

2.3 Large Particle Flow Analyzers

Large particle flow cytometers were first engineered in the late 1980's for analyzing and sorting samples of aquatic phytoplankton [20-21] as well as pancreatic islets [22]. The first instrument was developed de novo and was capable of analyzing a broad range of phytoplankton particles (0.5 – 500 μm in diameter, and over 2,000 μm in length), while the second instrument made modifications to a PARTEC PAS II cell sorter to distinguish pancreatic islets from exocrine tissue. Scaling up flow cytometry instruments to accommodate large particles requires major adjustments to the fluidic and optical components. The fluidic components must be carefully designed to minimize clogging, fouling and shearing of sample particles. Electrical and optical components must be adjusted to accommodate longer delay pulses for events, as well as detect fluorescence measurements that are representative of an entire particle.

The Complex Object Parametric Analyzer and Sorter (COPAS), built by Union Biometrica, was the first commercial, custom built system for high throughput analysis of large particles. COPAS incorporated the ability to analyze up to five parameters at once on particles up to 1500 μm in diameter. This instrument is capable of probing

large cellular entities such as pancreatic islets [23], stem-cell clusters [24], three-dimensional (3D) tissue constructs [25], *D. melanogaster* embryos and larvae [26-27], and *C. elegans* [28]. The primary limitation of the instrument is the inability to discern optical attributes of cells deep within an aggregate. This can be problematic for analyzing 3-D constructs since differences in viability, cell-type, and matrix composition can differ relative to position within a tissue or cell aggregate. This instrument is also expensive and not openly accessible to laboratories working with tissue constructs or multicellular aggregates.

2.4 Large Particle Sorting Systems

COPAS, as previously mentioned, was the first commercial high throughput large particle flow cytometer which also patented a sorting mechanism capable of purifying particles up to 1500 µm in diameter [19]. The mechanism consists of a solenoid valve located outside of the flow cell that is air pressurized and actuated (opened) in response to defined optical parameters. Unwanted particles are diverted into a waste container, while desired particles move freely through the system and are ultimately dispensed into microtiter plates. The system is a tremendous advance for sorting large particles, but purification is still limited by single photon optics that may not discern optical attributes deep within a particle. Additionally, the closed nature of the system limits the accessibility and flexibility desired for many basic research applications.

Microfluidic platforms have been utilized for several years to improve efficiency, accessibility and flexibility of systems designed to purify small particles [29-33] and have been utilized more recently to purify large particles based on particle size [34-35]. In particular, a microfluidic 1 mm glass capillary sorting mechanism was developed using diode laser bars to optically trap or deflect particles up to 200 µm in diameter [34]. Theoretically, different size particles can be sorted by size into different compartments based on the supplied laser power. However, since the length of the laser bar must increase to accommodate increasingly large particles, practical application of this approach to particles larger than 400 µm is limited. In addition, the impact of required laser power on the viability and function of biologic particles in this system is unknown. Another approach utilizes a physical separation scheme to sort large particles based on size in a microfluidic device. In this case, mouse EBs could be separated into three size groups without compromised viability [35].

2.5 Multiphoton Laser Scanning Microscopy (MPLSM)

MPLSM is a nonlinear optical sectioning technique that requires simultaneous absorption of two or more low-energy photons in the near infrared range for effective fluorophore excitation [36]. To ensure the simultaneous excitation of a fluorophore it is necessary to deliver an extremely high flux of photons to the sample. This is typically accomplished using pulsed lasers, such as titantium sapphire systems, that provide 100 femtosecond pulses at a repetition rate of 80MHz. Sufficient energy for two-photon excitation is only present at the plane of focus such that, unlike other fluorescence microscopy approaches, no out-of-plane signal interference or photobleaching occurs. Along with the fact that these longer wavelengths of light are more immune to scattering and are less phototoxic [37], the effective imaging depth can greatly exceed conventional confocal microscopy [38]. Imaging depth is especially important in the context of cellular aggregates (i.e. embryoid bodies (EBs)), where the typical size range is approximately 100 – 500 microns in diameter. Fluorescence signals beneath the surface of an aggregate are difficult to detect with current epifluorescence microscopes or flow cytometry systems, but can be resolved with MPLSM.

In addition to the aforementioned benefits, MPLSM also has the ability to detect many features of a cell without the use of extrinsic probes (i.e. intrinsically fluorescent structures) [39]. Two-photon excitation makes the detection of cellular intrinsic fluorophores, such as nicotinimide adenine dinucleotide (NADH) and flavin adenine dinucleotide (FAD), possible due to its improved signal-to-noise ratio and avoidance of ultraviolet exposure, which may be cytotoxic [40]. Both NADH and FAD play pivotal roles in energy metabolism, and thus provide information about the energetic state of the cellular microenvironment. While these fluorophores are excited in a similar fashion to extrinsic tags, non-linear optical effects other than multiphoton fluorescence excitation can also occur at the very high photon densities attained at the focus of the scanning excitation beam on the MPLSM.

Molecular assemblies with high-order structure, such as collagen matrices, can generate a second harmonic (SH) signal at half the wavelength of the excitation [41-42]. Unlike the case in MP imaging, the SH signal has a narrow spectral line-width (determined by the excitation source) and a zero lifetime. These characteristics allow SH signals to be distinguished from MP signals in a laser-scanning microscope with high peak intensity, ultrafast pulse excitation, even if there are fluorescence signals which overlap the SH signal. These features make SH imaging a very useful adjunct to MP imaging when[i] observing cells that are imbedded in an extra-cellular matrix, providing additional information about a tissue microenvironment. .

Another tool accessible on the MPLSM that is diagnostic of the microenvironment of a fluorophore is fluorescence lifetime imaging microscopy (FLIM) [43]. Factors such as ionic strength, hydrophobicity, oxygen concentration, binding to macromolecules and the proximity of molecules that can deplete the excited state by resonance energy transfer can all modify the lifetime of a fluorophore. Measurements of lifetimes can therefore be used as indicators of these parameters. Fluorescence lifetime measurements are generally absolute, being independent of the concentration of the fluorophore. Furthermore, lifetime properties may be particularly useful in identifying fluorophores with significantly overlapping spectral properties. Fluorescence lifetime imaging has been characterized and the potential of this technique has been demonstrated [44-46], including its importance to stem cell biology [47-50].

CHAPTER 3

Validation of a Multiphoton Flow Cytometer (MPFC) for Analysis of Cellular Aggregates

3.1 Specific Objective 1: To develop a proof of concept Multiphoton Flow Cytometry (MPFC) system

Hypothesis: A novel optical arrangement including multiphoton excitation could be used to enhance the ability of flow cytometry systems to accurately and non-invasively probe cells in the interior of microtissues in an enhanced throughput fashion (thereby addressing design criteria A and B).

Given the unique properties of MPLSM and corresponding potential for stem cell imaging, we hypothesized that a novel multiphoton fluorescence excitation flow cytometry instrument (MPFC) could be developed to accurately probe cells deep in the interior of multicellular aggregates or tissue constructs in an enhanced-throughput manner. Furthermore, if this system is used to excite endogenous fluorophores of cells as potential intrinsic biomarker candidates, the application of exogenous fluorescent labels is thereby avoided and fixation is unnecessary. Others have considered the possibility of a multiphoton flow instrument (or multiphoton flow cytometry) [51-53] for analysis of cells and cellular aggregates in turbid and nonuniform flow conditions, such as may be encountered in blood vessels *in vivo*. In the future, our intent is to devise a fluid-controlled *in vitro* system such that cellular and multicellular entities might not only be analyzed but also sorted based on endogenous fluorescent properties. Cells sorted with this system would, in principle, be viable and their cell-to-cell contacts unperturbed, unlike the output of current flow cytometry sorting systems, and so could be used directly for clinical application.

The instrument we have developed is comprised of a *flow cell* through which large particles stream past a light interrogation point, an *optics system* with two-photon excitation capability and *data acquisition software* to quantify the data (**Figure 3.1**). In the course of constructing this proof-of-concept MPFC instrument, we sought to incorporate an open frame hardware system structure and modular acquisition software package to yield an accurate, non-invasive and enhanced-throughput system to assess stem cell state (including metabolic, viability and functional status) at a three-dimensional level. Here we describe the instrument design as well as validate the proof of concept prototype, in terms of integrity of the width of the sample stream, particle recovery, speed of image capture, accuracy of image capture and accuracy of measured fluorescence intensity. The latter analyses were conducted on

both synthetic fluorescent beads and stem cell aggregates, including analysis of both extrinsic and intrinsic fluorescence.

3.2 Materials and Methods

3.2.1 Construction of Flow Cell

The flow cell was constructed using standard photolithographic and soft lithography techniques [54-58]. Two 500 μm layers of SU-8 2150 negative photo resist were spun onto a silicon wafer substrate by manipulating spin speed and spin time. Soft bakes and post exposure bakes of the photo resist layer were performed according to manufacturer's specifications (Microchem, Newton, MA). Liquid phase polydimethylsiloxane (PDMS) (Sylgard 184, Dow Corning, Midland, MI) mixed at a 10:1 base to curing agent ratio was poured over the silicon master and heated for one hour at 95 degrees Celsius. Three inlet ports (two for sheath channels, one for sample) and one outlet were cored out of the PDMS device using a 16 gauge blunt needle. Polyvinyl choloride (PVC) Tygon tubing (0.1 cm I.D., 0.2 cm O.D.) created a leak-free seal when inserted into the inlet and outlet ports of the elastomeric PDMS. A 0.15 mm thick glass cover slip was irreversibly bonded to the PDMS by oxygen plasma treatment [59]. The sheath syringe fed into a three way mechanical valve that split the stream to the left and right inputs of the flow cell (**Figure 3.2A, B**). The three way valve was implemented to temporarily flush the flow cell of air bubbles and manually calibrate the focused stream with fluorescein dye before testing. The sheath inlet channels were designed to be 2 mm in width, the sample channel 1 mm in width, and the outlet channel 5 mm in width and 76 mm in length (**Figure 3.2 A, B**). The large width of the outlet channel was designed to decrease the average (and maximum) velocity of the large particles, to accommodate a particle scanning speed of 2-3 frames/second.

3.2.2 Integration of Flow Cell on Multiphoton Laser Scanning Microscopy System

Two separate programmable syringe pumps (Braintree Scientific Inc., Braintree, MA, model BS-8000/9000), housed 20 cc syringes to drive sheath and sample liquids through the attached tubing and flow cell. The flow cell was mounted on a length-wise adjustable stage insert compatible with most microscope stages, and therefore easily adjusted via the xy stage controller and z-focus. The sheath to sample rate ratio, α, is reported as the summed volumetric flow rates of both sheath ports over the volumetric flow rate of the sample port. The ratio utilized throughout this work was $\alpha = 2.0$ and maximum volumetric flow rate of the outlet channel equal to 900

µl/min. Samples were interrogated with either 890 nm or 780 nm wavelength light and images collected with Nikon lenses (Nikon, Melville, NY), either a 1.0 mm WD, 0.75 NA, 20X air lens or a 1.2 mm WD, 0.75 NA, 10X air lens with a typical scan speed of approximately 2.33 frames/second and resolution of 256 x 256.

3.2.3 Validation of Flow Stream Widths

Five drops of fluorescein dye was added to 20 ml of deionized water and loaded into the sample syringe to verify the boundaries of the focused sample stream in the flow channel. Focused stream widths were recorded on the MPFC set up and measured with ImageJ (http://rsbweb.nih.gov/ij/) [60]. Theoretical stream widths were calculated based on previous studies of hydrodynamic focusing in rectangular microchannels [61]. By conservation of mass, the width of the focused stream can be determined using:

$$\frac{w_f}{w_0} = \frac{Q_i}{\gamma(Q_i+Q_s)}$$

where w_f is the width of the focused stream, w_0 is the width of the outlet channel, Q_i is the volumetric flow rate of the sample inlet and Q_s is the volumetric flow rate of the two sheath inlets combined. γ represents the velocity ratio, $\frac{v_f}{v_0}$, where $\boldsymbol{v_f}$ and $\boldsymbol{v_0}$ correspond to the average flow velocities in the focused stream and the outlet channel, respectively. Nine different sheath to sample ratios within a pertinent range were analyzed while testing three different volumetric flow rates for each data point to ensure reproducibility at different Reynold's numbers 0.9 - 9.0.

3.2.4 Validation of Size and Fluorescence Intensity using Polystyrene Fluorescent Microspheres

Fluorescent microspheres, approximately 100, 200, and 400 µm in diameter (Duke Scientific Corporation, Palo Alto, CA) were suspended in 1X phosphate buffered saline (PBS) containing 0.1% Triton X-100. These microspheres were used to calibrate optical parameters and verify proper functioning of the fluidic component.

3.2.5 Cell Culture and EB Formation

Mouse embryonic stem cell (ESC) lines used were D3 [62] and HM1 αMHC::GFP. The αMHC::GFP cell line was generated by transfecting (Lipofectamine, Invitrogen, Carlsbad, CA) a plasmid containing the 5.5 kb promoter region of the αMyosin Heavy Chain gene driving EGFP [63] into HM1 ES cells [64] to express GFP in cardiac myocytes. ESCs were cultured in Dulbecco's Modified Eagle Medium (DMEM) with 10% FBS with the addition of Leukemia Inhibitory Factor (LIF, Millipore/Chemicon, Billerica, MA) at 2000 U/ml and Bone

Morphogenic Protein 4 (BMP-4, R&D Systems, Minneapolis, MN) at 10ng/ml [65] in 5% CO2 at 37^{o}C. Embryoid bodies (EBs) were made via the hanging drop method [66]. Briefly, ESCs were trypsinized and resuspended in DMEM with 10% FBS (no LIF or BMP-4) to 1.6 X 10^4 cell/ml. This cell suspension was used to make 30 µl hanging drops in 100mm Petri dishes over PBS. EBs were harvested on days 8 and 12 after formation of hanging drops, placed into a 50ml conical tube and allowed to settle. Supernatant was removed and EBs were resuspended in 20 ml DMEM with 10% FBS and remained in suspension, at 37^{o}C until used in the flow cell (<4 hrs). A small number of EBs used were plated onto 60mm gelatinized culture dishes to confirm the ability of those EBs to attach and form contracting cardiomyocytes.

3.2.6 Static Imaging of NADH Fluorescence Intensity in EBs on MPLSM and confocal microscope

Measurements of NADH fluorescence intensity throughout the EB volume were made on both the MPLSM and a Nikon Eclipse Ti inverted confocal microscope (Prairie Technologies, Middleton, WI) by taking serial optical sections of EBs at 1µm intervals beginning at the coverslip (z=0) and moving toward the center of the cell aggregates (z=50µm). NADH was measured with MPLSM by tuning the Ti:Sapphire laser to 780nm and collecting fluorescence emission through a 457/50 bandpass emission filter (Chroma Technology Corporation, Rockingham, VT), while NADH was measured with confocal microscopy at an excitation wavelength of 405 and a 460/50 nm bandpass filter (Chroma Technology Corporation, Rockingham, VT) with a 80 µm pinhole. Images on both systems were taken at a resolution of 512x512, with the same 1.0 mm WD, 0.75 NA, 20X air lens (Nikon TE2000, Melville, NY). The power measurements at the sample were 1 mW and 30mW, for the confocal microscope and MPLSM, respectively. EBs were imaged in 9 x 2 ibidi microslides (ibidi, Martinsried, Germany), and cultured after imaging, to assess morphology and attachment on the following day.

3.2.7 Analysis of EBs on MPFC

Deionized water was loaded into the sample and sheath syringes and run through the system for 5 minutes. Subsequently, 10 ml of 1X PBS containing 0.2% bovine serum albumin (BSA), was loaded into the sample syringe, and run through the sample tubing and the flow cell. BSA was used to bind nonspecific protein binding sites in the tubing and flow cell and so prevents cell adhesion to the biomaterials present in the system. EBs were counted by the observer before being suspended in 10 ml of DMEM complete medium, and loaded into the sample syringe. The

MPLSM Ti:Sapphire laser (Spectra Physics Tsunami, Newport Corporation, Palo Alto, CA) was tuned at 780 nm excitation for NADH detection and 890 nm excitation (with a 520/35 bandpass emission filter, Chroma Technology Corporation, Rockingham, VT) for GFP detection (excitation 489 nm, emission 509 nm). Power and gain settings of the laser were set such that less than 5% of pixels were saturated and background noise was kept to a minimum. Sheath to sample ratios were kept constant at 2, with a total volumetric flow rate (combined sheath and sample volumetric flow rates) of 600 μl/min. A sample volumetric flow rate of 200 μl/min was used when analyzing EBs. Bright field and intensity images were collected using in-house developed software (WiscScan) for both acquisition and quantitative and morphological analysis. A subpopulation of EBs were imaged statically in a glass bottom dish (MatTek Corporation, Ashland, MA) before and after MPFC analysis, under the same imaging conditions used for flow conditions. Fluorescence and size measurements of EBs were made using ImageJ software [60]. For analysis, threshold values were set such that less than 0.1% of pixels on a background image were saturated for all conditions.

3.2.8 Statistical Analyses

For comparison of size and fluorescence intensity levels of beads and cell aggregates under static and flow (MPFC system) conditions, a normal distribution was assumed and one-way analyses of variance (ANOVA) and Student *t*-test for unpaired samples were used. Data were analyzed with JMP 5.0.1 for Windows (SAS Institute, Inc., Carey, NC). A 95% confidence ($P < 0.05$) interval was applied as the criterion to determine statistically significant differences.

3.3 Design of Instrument

The MPFC system integrates three components: fluidics, optics and data acquisition. These components are linked as illustrated in the comprehensive schematic (**Figure 3.1**).

3.3.1 Fluidic Components

The fluidic components of a flow cytometer require careful design considerations, as they can adversely impact cell phenotype and viability. This especially holds true when flowing large cellular aggregates that are more

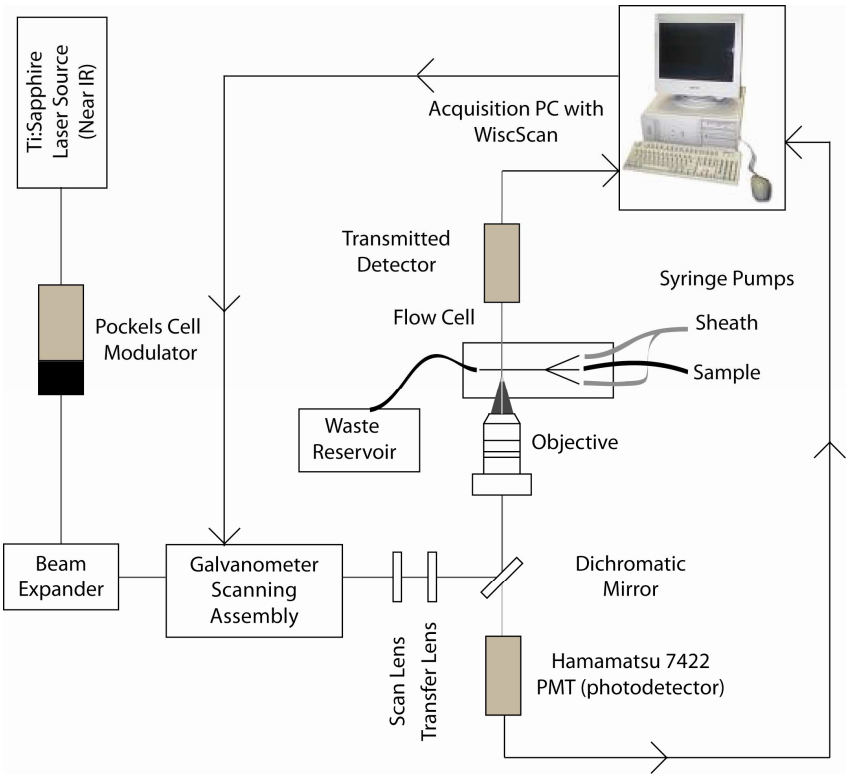

Figure 3.1 Schematic diagram of the MPFC system. A microfabricated flow cell is placed on a multiphoton laser scanning microscope equipped with a Ti:Sapphire laser for excitation, photomultipliers, and scanning optics and electronics for signal collection. Sample fluid (i.e., biological specimens or beads) and sheath fluid are introduced into the microchannels using syringe pumps and associated tubing. See the Materials and Methods and the Results sections for additional details.

prone to shearing and clogging than single cells. The need for a gentle flow mechanism is also heightened when considering use of cell aggregates for therapeutic use following imaging, assessment and sorting. For this reason, the MPFC employs a horizontal flow cell made from PDMS microchannels plasma-bonded to a glass coverslip (**Figure 3.2A, B**) [57, 67]. At the point of light interrogation, the chamber width of the flow cell is 5 mm, the chamber height is 0.7 mm. Sample and sheath volumes were typically delivered using syringe pumps connected to the flow cell with Tygon tubing (0.1 cm I.D., 0.2 cm O.D.) at rates of 50-500 μl/min and 100-1000 μl/min, respectively.

3.3.2 Optical Components

The MPFC system was built on an existing MPLSM platform designed for static (i.e., non-flow) imaging located in the Laboratory for Optical and Computational Instrumentation (LOCI), University of Wisconsin at Madison [68-70]. While the MPLSM systems at LOCI have advanced instrumentation for spectral lifetime collection, adaptive optics, and second harmonic generation, the heart of the MPLSM system is a standard inverted microscope (Nikon TE2000, Melville, NY) with Cambridge galvos (Cambridge Technology, Billerica, MA) for scanning, Tsunami (Spectra Physics, Palo Alto, CA) Ti:Sapphire laser, a Hamamatsu H7422 GaAsP Photomultiplier detector (Hamamatsu Photonics, Bridgewater, NJ) for fluorescence intensity detection and a sensitive silicon photodiode detector (Bio-Rad, Hercules, CA) for simultaneous transmission image collection. The purpose of detecting a transmitted image simultaneously has advantages inherent with collecting an image, namely, morphological analysis and detection of localized fluorescence within a multicellular entity. With no penalty in regards to acquisition speed or signal sensitivity, there was no reason not to collect a bright field image in addition to the quantifiable fluorescence intensity image. The MPFC has been intentionally designed as a microscope stage insert such that it can readily be deployed on other MPLSMs including commercial systems.

3.3.3 Data Acquisition Components

The MPFC was designed to be a modular system that could interface with existing laser-scanning systems, either home built or commercially available. MPLSMs have extensive proprietary electronic and software scanning routines that would be expensive and unnecessary for the MPFC software to replicate. Instead, the MPFC software is built as a modular set of libraries that can be called by or interfaced with a commercial package. For the prototype

system we used a laser scanning software package, WiscScan, developed at LOCI and deployed in a wide range of biological studies [71-74]. While WiscScan does have some novel features that are particularly well suited for our application, the majority of the core acquisition functionality is representative of a commercial MPLSM package. Thus the WiscScan-MPFC integration is useful not only as a standalone entity but also as a case study for deployment with other MPLSM control systems.

The majority of the MPFC features, such as simultaneous acquisition of transmitted images and multiphoton fluorescence data, image zoom and integration (averaging) functionality are standard components of any MP system (including the LOCI instruments). The majority of the MPFC software development involved adding a real time quantitative readout of the flow stream on the MPFC for real-time morphology and intensity analysis. The MPFC departs from traditional flow cytometers in that an image is displayed in real time of the flow stream rather than a plot of the intensity alone. This is advantageous but a quantitative readout of the intensity and other particle properties is still needed. Rather than develop a proprietary solution for this, that is "hard coded" into WiscScan, we opted to develop an open source module for MPFC display and analysis that could interface with any MPLSM software package (using WiscScan as the test case). This module provides a real-time software analysis display so that when the multiphoton images are collected of the flow stream, a quantitative readout is displayed simultaneously. The open source ImageJ software package (NIH) was chosen as the toolkit for this module development because this popular package already provided most of the functionality for this type of analysis and had the added advantage that any developed code could be run within WiscScan at runtime, or offline as a plug-in within ImageJ. Other analysis functionality including existing flow cytometer analysis approaches from the community at large, can easily be added by using the same conduit and existing plug-in and macro functionality of ImageJ.

3.4 Instrument Validation

In order to validate the functionality of the MPFC design, a variety of tests to examine the physical characteristics of the system as well as the applicability of the MPFC were performed to assess fluorescence of large particles. Fluorescent beads were used as uniformly sized, non-biological standards while mouse EBs were used as an example of cell aggregates, or microtissues.

3.4.1 Control of Sample Stream Width via Hydrodynamic Focusing

Hydrodynamic focusing is the process by which two fluids under laminar flow and in common containment, remain as separate streams based on differences in density, viscosity, the dimensions of the containment vessel and/or velocity. This process is commonly used in flow cytometry to alter sample stream dimensions within a flow cell without constructing multiple flow cells of different dimensions. Here, a horizontal flow cell was microfabricated as described above (**Figure 3.2A**). Sheath and sample fluids were delivered using syringe pumps connected to the flow cell with tygon tubing at rates of 100 – 1000 µl/min and 50 – 500 µl/min respectively. To determine the range and variability of the sample streams possible in our flow cell, we modified the sheath to sample velocity ratio from 2 to 15 and measured the width of the resulting sample stream. The sample stream was distinguished from the flow stream by incorporating fluorescein into the sample fluid (**Figure 3.2C**). Sample streams of 300 – 1600 µm could be reliably achieved and precisely corresponded to modeled predictions (**Figure 3.2D**, $R^2 = 0.98$) [61].

3.4.2 Validation of Optical Acquisition using Polystyrene Beads

Intensity image data acquired from a sample flowing through the MPFC system may vary from static measurements of the same sample if the data acquisition rate is slower than the sample speed per unit time or if the fluidic system mechanically disturbs the sample as it passes through the flow cell. To test the former, we introduced polystyrene beads of known diameter (100, 200 and 400 µm) into the MPFC system at maximum volumetric flow rate (300 µl/min, ratio of sheath to sample = 2) and measured the diameter of bright field images of flowing beads. Increased bead dimensions would indicate an insufficient image capture speed. Using acquired bright field images, we compared the average diameter of the flowing populations of beads to the average diameter of the same populations prior to introduction into the MPFC system. For all bead populations, the MPFC mean diameter (114 $\pm$ 9.2, 207 $\pm$ 8.9 and 408 $\pm$ 17.1) did not vary significantly from the static mean diameter (115 $\pm$ 6.4, 207 $\pm$ 8.6 and 402 $\pm$ 15.8: $P = 0.69$, $P = 0.91$, $P = 0.08$, respectively); **Figure 3.3A-C**). To further confirm that the electronics and data acquisition system provided appropriate acquisition speed to accommodate the maximum flow of the MPFC system (and to ensure events are not missed) we measured the mean intensity of individual polystyrene beads labeled with

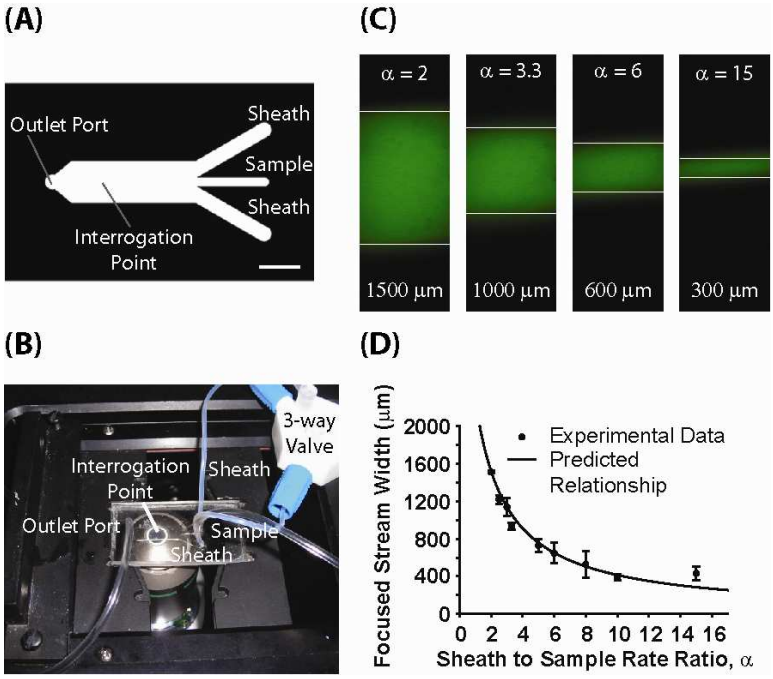

Figure 3.2 A microfabricated flow cell to accommodate large particles. Sheath and sample volumes were introduced into a PDMS microfabricated flow cell and flow rates were controlled via syringe pumps. A) Top-down view of the microfabricated flow cell. Features of the flow cell include waste output/reservoir drop, sample input and sheath input, and an interrogation point where optical analysis occurs. Scale bar, 5 mm. B) Top-down photograph of the flow cell housed in the modular stage insert. Features of the stage insert include a series of tubing adaptors that allow the flow cell to be easily added to and removed from the MPLSM system. C) Hydrodynamic control of the sample path. Images captured using the WiscScan software illustrate how varying the sheath to sample flow velocity ratios, α, alter the width of the sample stream. D) Comparison of the predicted focused width with experimental data at different ratios of sheath volumetric flow rate to sample volumetric flow rate (100–1,000 and 50–500 μL/min, respectively). Model predictions were based on those previously published [61].

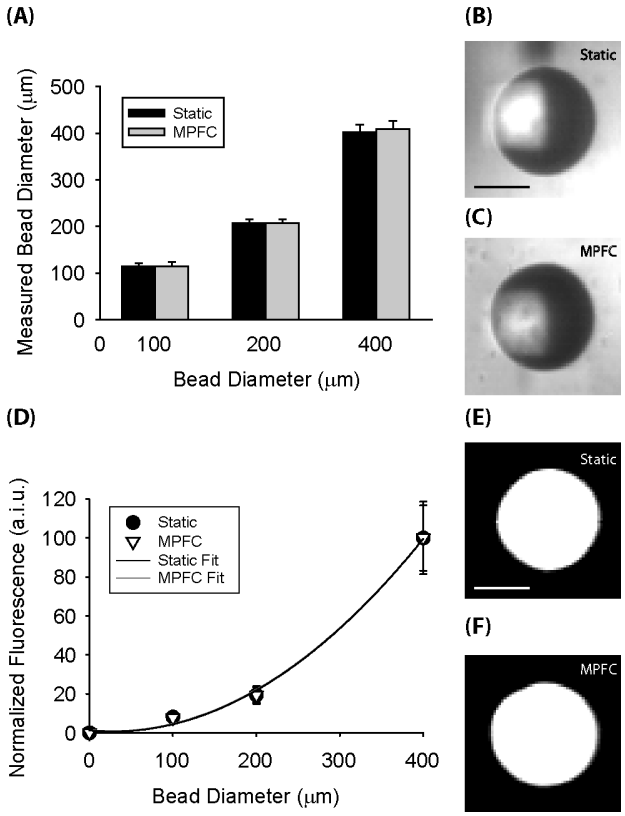

Figure 3.3 Size and intensity of fluorescent, polystyrene beads using the MPFC system. A) Accuracy and precision, using bright-field optics, of bead size using MPFC compared to bead size discerned using the MPLSM system without flow (i.e., static). Bead size measured under static conditions did not vary from bead size when measured on the MPFC system (P = 0.69, P = 0.91, P = 0.08). B) Bright-field image of a 400 µm bead under static conditions. C) Bright-field image of a 400 µm bead using MPFC. Lack of warping and elongation indicate data acquisition rates were similar to the fluidic sample speed per unit time and that the microspheres experienced minimal mechanical disturbance. D) Relationship between bead diameter and normalized fluorescence intensity. Best fit regression analysis was applied to the datasets and both static and MPFC conditions yielded second-order exponential relationships; R^2 values of 0.99 and 0.99, respectively. E) Fluorescence intensity image of a 400 µm bead (same bead as B) under static conditions. Static images were captured at the location corresponding to the maximum total intensity. F) Fluorescence intensity image of a 400 µm bead using MPFC (same bead as C). Mean fluorescence intensity did not vary between static and MPFC acquisition modes for each bead size (P = 0.58, P = 0.72, P = 0.74). a.i.u, arbitrary intensity units. Scale bar, 200 µm.

fluorescein. As before, polystyrene beads of known diameter (100, 200 and 400 µm) were introduced into the MPFC system at maximum volumetric flow rate (300 µl/min, ratio of sheath to sample = 2) and the mean intensity of flowing beads was determined. The mean intensity values of the flowing populations were compared to the mean intensity values of the center-most plane of the same populations prior to introduction into the MPFC system. For all bead populations (100, 200 and 400 µm), the MPFC normalized fluorescence measurements (8.1 $\pm$ 1.3, 19.4 $\pm$ 3.8 and 100 $\pm$ 18.6) did not vary significantly from the static normalized fluorescence measurements (7.7 $\pm$ 1.3, 19.4 $\pm$ 4.5 and 100 $\pm$ 16.7, $P = 0.58$, $P = 0.72$, $P = 0.74$); **Figure 3.3D-F**). The fact that intensity values in the flow system did not differ from those in static images indicates sufficient image capture speed. In addition, these results suggest there is limited sample movement within the Z focal plane during fluidic delivery.

3.4.3 Validation of Detection Depth

To determine whether the MPFC system was capable of generating information related to the interior portion of large entities by deep optical assessment, we mapped the mean fluorescence intensity as a function of bead size using the data obtained above. If detection of fluorescence in the interior of the microsphere were possible, one would expect an exponential trend between the size of the fluorescent sphere and the emitted fluorescent signal, by capturing a true representative cross sectional area, and not simply surface fluorescence. One of the unique aspects of multiphoton fluorescence excitation is its ability to probe deep into tissue sections, which can be attributed to the fact that light scatter varies as an inverse function of wavelength. As a result, the infrared light used in MPFC obtains much higher depths of penetration than single photon excitation. Other commercial flow systems with fluidics capable of handling large particles cannot detect fluorescence in the interior of large entities and so the relationship between size and fluorescence is linear (Union Biometrica, COPAS system [23]). These results indicated that the COPAS system is able to assess light emission corresponding to cross-sectional circumference and not cross sectional surface area. When conducted with the MPFC, an exponential relationship was observed (**Figure 3.3D**), confirming the ability of the system to non-invasively probe the interior of large entities in an enhanced-throughput manner.

3.5 Assessment of Biological Applicability

3.5.1 Capacity of the MPFC to Analyze Stem Cell Aggregates

Cells are dynamic entities that are susceptible to mechanical forces and so the analysis of cells in the MPFC may differ dramatically from that of polymer beads. For example, cells are impacted by shear forces generated as a consequence of flow. Multicellular aggregates are particularly susceptible as intercellular connections can be disrupted by forces of ~ 0.6 µdynes/connection or approximately 6 µdynes/cell [75-76]. If such connections are disrupted, biologic activity and ultimately therapeutic utility might be compromised. Thus the MPFC system was designed to reduce shear forces to less than or equal to 0.6 µdynes/cell. In addition, cells, especially stem cells, express many cellular and extracellular binding receptors (i.e., cadherins, integrins) which can make them "sticky" as they are transported through the flow system. To determine whether stem cell aggregates would be mechanically disrupted using the MPFC system, we generated mouse EBs and measured the diameter of each EB before, during and after introduction into the MPFC system. EBs used in these studies were 8 - 12 days old. Because EBs can vary in size due to variation in seeding density, time in suspension and user technique, the measured diameter was normalized to the mean diameter of EB populations on each day of analysis (**Figure 3.4**). The normalized size distribution did not vary significantly for EBs analyzed during (1.06 ± 0.04, $P = 0.05$) or after flow (1.02 ± 0.03 $P = 0.29$) when compared to EBs prior to introduction into the MPFC system. Standard deviation for EB size was less than 13% of the total size, indicating high precision of the MPFC system given the biologic nature of the samples. In addition, bright field images were examined for evidence of frayed (disrupted) cell aggregates. The mean fraction of EBs exhibiting fraying or loss of a defined border affecting at least 25% of the perimeter was slightly higher in samples examined post-MPFC compare to samples examined pre-MPFC (13% $\pm$ 12%, pre-MPFC, n = 177 and 25% $\pm$ 12%, post-MPFC, n = 171, in 5 trials) but this difference was not statistically significant ($P = 0.18$). Thus, the composition of the fluidics system inflicts minimal mechanical disruption to these multicellular entities.

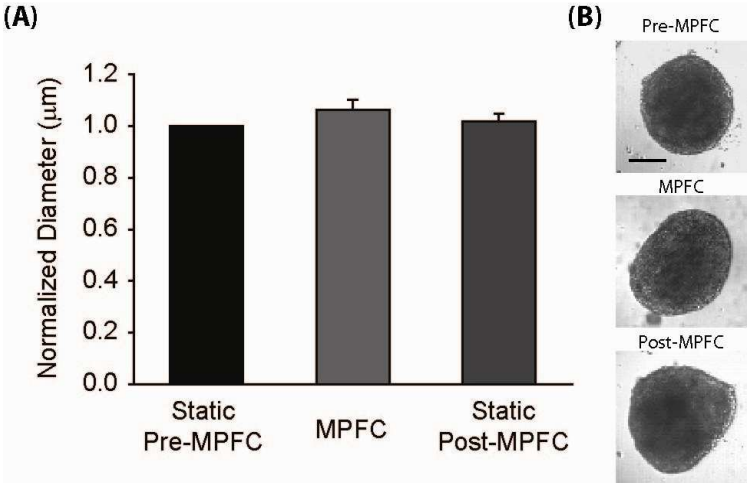

Figure 3.4 Size of EBs using the MPFC system. A) Accuracy and precision of EB size using MPFC compared to EB size discerned using the MPLSM system without flow (i.e., static). Measurements of EB size, using bright-field optics, were made prior, during, and following introduction of the EBs into the MPFC system. Standard deviation for EB size was less than 13% of the total size. EB size discerned under static conditions after MPFC did not vary from EB size discerned using the MPFC system (P = 0.05 (pre versus MPFC), P = 0.29 (pre versus post), P = 0.13 (flow versus post)). EBs were introduced into the MPFC at a volumetric flow rate of 200 μL/min, which remained consistent between experiments. B) Bright field images of pre-MPFC static, MPFC, and post-MPFC static EBs. Multicellular aggregates maintained original morphology and defined peripheral border during and after analysis with MPFC. Scale bar, 200 μm.

3.5.2 Detection depth of MPLSM

Three dimensional tissues are difficult to analyze without disaggregating or sacrificing the specimen, due to their relatively dense compositions and high scatter properties. Using confocal microscopy as a well-defined technology for deep optical sectioning, we sought to compare the depth at which MPLSM is capable of exciting and detecting NADH endogenous fluorescence intensity within EBs. Serial z-stack images were acquired from the surface (i.e. coverslip) to the center of the EBs using a Nikon Eclipse Ti inverted confocal microscope (Prairie Technologies, Middleton, WI) and our MPLSM. EBs were imaged individually in 9x2 microwell slides to assess their morphology and attachment overnight after laser exposure on both systems. Normalized average intensity was measured in regions of interest where fluorescence intensity is diminished the most when imaging deeper into microtissues. The maximum values of mean fluorescence intensity per unit area were found to be 12 µm and 16 µm, on the confocal microscope and MPLSM, respectively (**Figure 3.5**). Half of that maximum average intensity was lost at 22 µm on the confocal, while half of the maximum is lost on the MPLSM 38 microns into the EB. In addition to deeper optical penetration, all EBs exposed to multiphoton excitation attached to microwell plates overnight, whereas those exposed to single photon excitation at 405nm did not attach to microwells, indicative of aggregates containing a significant amount of cell death. Though signal attenuation due to scattering is a hurdle to analyzing cell aggregates due to their tight packing and density, MPLSM can probe deeper than a confocal microscope when measuring NADH in EBs, while also preserving EB viability, allowing for long-term culture and functional assessment of populations.

3.5.3 Comparison of Mean Intensity per unit Area vs. Mean Intensity per unit Volume in EBs

To determine the z-plane that would most accurately reflect the fluorescence intensity of an EB throughout its volume, we took serial z-stacks from the coverslip (z=0) to 35 µm deep (where signal loss at the center of an EB can be observed) probing for the intrinsic fluorophore, NADH. The intensity of every pixel throughout the 35 z-sections was averaged for the volume measurement and subsequently compared to the average intensity measured at single optical sections of 5, 20, and 30 µm deep. We found the z-slice at a depth of 30 µm was the most accurate estimation of the volume measurement, with a linear slope of 1.03 and an $R^2 = 0.99$, whereas measurements at the surface of the EB were an underestimation and measurements at 20µm were an overestimation (**Figure 3.6**).

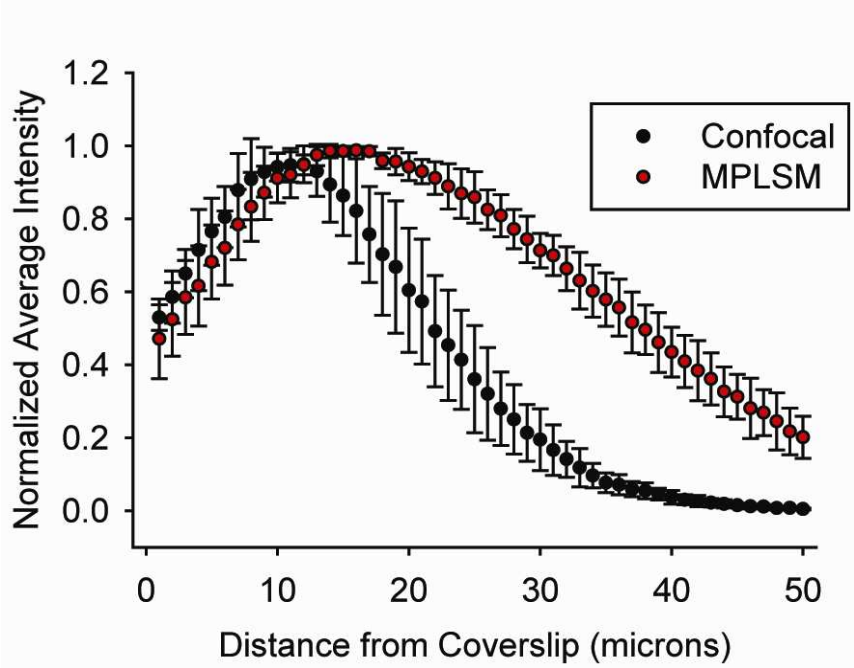

Figure 3.5 Comparing depth of optical penetration using MPLSM versus confocal microscopy. NADH fluorescence intensity was detected in optical sections of EBs taken at 1 µm increments from the coverslip of imaging dishes to 50 deep into EBs. The graph depicts that the maximum fluorescence intensity is acquired deeper into the specimen using MPLSM when compared to confocal microscopy.

To determine the total area measured at such a z-section we applied the following formula measuring the radius, r_1, of a cross section of height h within a sphere of radius r:

$$r = \frac{(h^2 + r_1^2)}{2h}$$

For example, at a height of 30 µm within a 200µm sphere, $r_1 = 0.71r$, corresponding to an area 51% smaller than the center plane of this sphere. As particles get bigger this area at 30 um becomes smaller, and less representative of the volume measurement, while measuring particles smaller than 200 µm in diameter will result in a greater area compared to the center plane and becomes more representative of the particle.

3.5.4 Analysis of Extrinsic Fluorescence of Multicellular Aggregates via MPFC

One of the primary challenges of stem cell research and clinical application is the generation of purified, mature cell types after differentiation. To this end, many researchers have established reporter stem cell lines coupled to lineage-specific promoters. While exceedingly valuable, lacking is the ability to detect these reporters in multicellular aggregates (including EBs) in an enhanced-throughput manner and to sort based on this detection. The MPFC system has potential to address this need. To determine whether extrinsic fluorescent reporters of stem cell differentiation could be detected in EBs, mean fluorescence intensity of alpha-Myosin Heavy Chain (α-MHC)::GFP transfected EBs and non-transfected EBs, was determined using the MPFC. Alpha-MHC expression in this case indicates differentiation of a subset of embryonic stem cells to spontaneously contracting cardiomyocytes. Using the culture protocol described in the methods section, an estimated 30-70% of EBs undergo cardiac differentiation and so will contain GFP^+ regions (data not shown). GFP fluorescence was detected with the laser set for 890nm excitation wavelength and a 525/30 band pass emission filter. Mean fluorescence intensity of transfected EBs did not differ significantly before, during or after MPFC (46.1 $\pm$ 24.6, 42.5 $\pm$ 24.7, 39.6 $\pm$ 29.3 respectively, $P = 0.47$ (pre vs. MPFC), $P = 0.24$ (pre vs. post), $P = 0.60$ (MPFC vs. post); **Figure 3.7**). In addition, the data were analyzed to determine whether the GFP^+ fraction detected with MPFC corresponded to that detected using static MPLSM. To this end, a gate based on mean fluorescence intensity was established to exclude ~ 95% of non-transfected EBs; thus events exceeding the mean fluorescence intensity of the gate value (dotted vertical line on histogram plots, **Figure 3.7**) were deemed GFP^+. The fraction of GFP^+ events of the EBs from the α-MHC::GFP line, pre-MPFC, MPFC, and post-MPFC were 66%, 60%, and 46%, respectively (**Figure 3.7**). The post-MPFC fraction is substantially less that the pre-MPFC and MPFC values and likely reflects the suboptimal conditions in which the EBs were

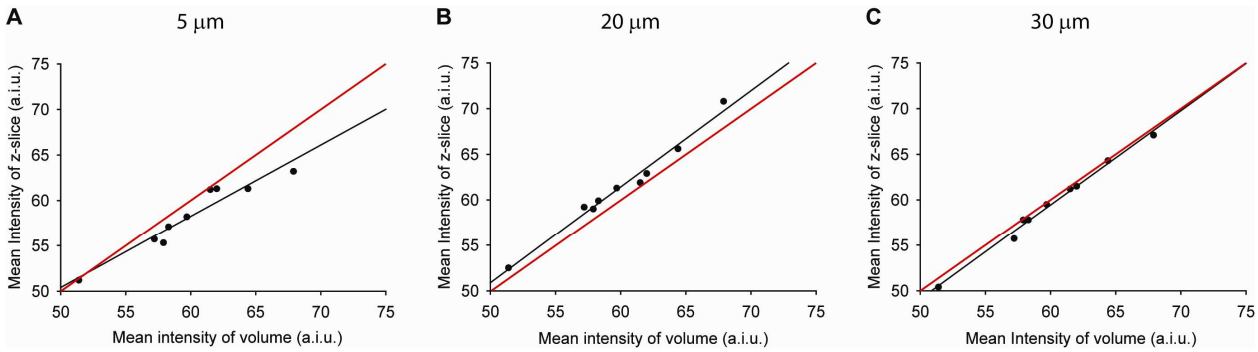

Figure 3.6 Comparison of mean intensity per unit area vs. mean intensity per unit volume in EBs. Images measuring NADH fluorescence intensity were taken at 1µm increments from the coverslip of imaging dishes to a depth of 35µm into EBs. The mean intensity of 2-D slices at A) 5 µm, B) 20 µm, and C) 30 µm deep were compared to the mean intensity of the volume spanning a depth of 35 µm and linear regression lines (black lines) were assigned to the corresponding scatter plots. The red line corresponds to a linear regression of 1, which represents an ideal scenario of estimating the volumetric fluorescence intensity with a single optical section.

maintained after flow. These conditions include diluted media as a consequence of merging sheath and sample streams in the collection vessel and uncontrolled temperature and gas exposure in the collection vessel. The similarity in proportion of detected fluorescent aggregates between the pre-MPFC and during MPFC conditions indicates that extrinsic fluorescence of stem cell aggregates can be reliably detected by the MPFC system in an enhanced throughput manner. Future adaptations to incorporate a sterile sorting mechanism with controlled nutrient, temperature and gas exposure will prove very useful for the generation of mature cell types for analytical study and clinical application.

3.5.5 Analysis of Intrinsic Fluorescence of Stem Cell-Derived EBs via MPFC

Continued advances in stem cell research and clinical application depend on the discovery of non-invasive endogenous biomarkers (as opposed to extrinsic, invasive markers, including the GFP reporter system described above) to discern stem cell status and differentiation state at both the single cell and three-dimensional (i.e., cell aggregate or tissue construct) level and to sort populations based on this assessment. Multiphoton Fluorescence Excitation (MPFE) based approaches have been shown to be able to detect differences in the intensity of intrinsic fluorescence between cells in different functional states [73, 77-78], including between stem cells and mature cells [79-80]. So, in principle, the MPFC system should be capable of the same in enhanced-throughput. To test this possibility, we introduced 8 – 12 day EBs into the MPFC system and probed for intrinsic fluorescence, most likely from NADH, using 780nm two-photon excitation. Mean fluorescence intensity was determined for EBs in this context before, during and after MPFC analysis. Mean intrinsic fluorescence did not vary between conditions (91.8 $\pm$ 35.0, 86.8 $\pm$ 36.7 and 85.2 $\pm$ 34.7 respectively: $P = 0.55$ (pre vs. MPFC), $P = 0.46$ (pre vs. post), $P = 0.89$ (MPFC vs. post); **Figure 3.8A**), however the standard deviation was substantially high. Variation was not a consequence of manipulation or an artifact of the MPFC system as the intensity distribution was similar for all conditions (**Figure 3.8B, C**). Indeed, high variability was anticipated as EBs cultured in this manner begin maturation in an uncontrolled temporal and spatial fashion and therefore would be expected to elicit different metabolic demands depending on the phase of development. It is precisely these differences that we hope to capitalize upon to employ intrinsic fluorescence as an indicator of stem cell viability and differentiation status.

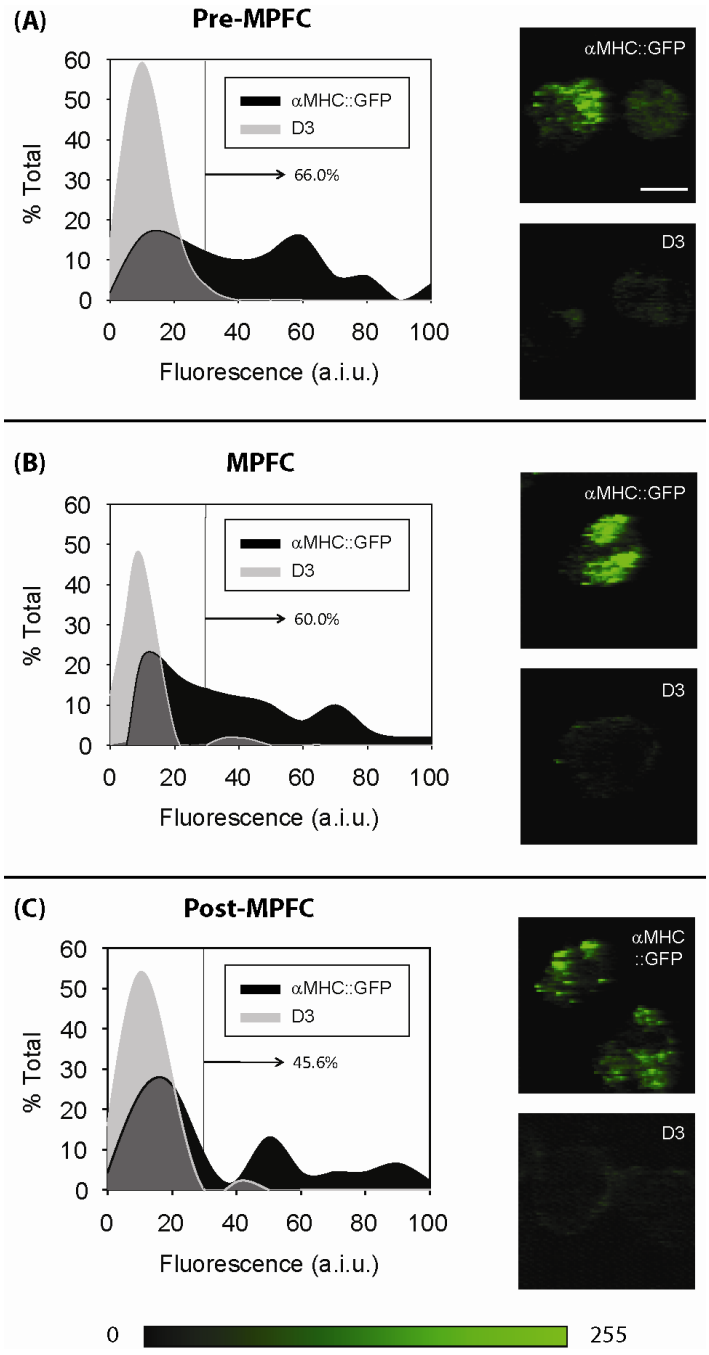
(A)
Pre-MPFC
αMHC::GFP
D3
66.0%
% Total
Fluorescence (a.i.u.)
αMHC::GFP
D3
(B)
MPFC
αMHC::GFP
D3
60.0%
% Total
Fluorescence (a.i.u.)
αMHC::GFP
D3
(C)
Post-MPFC
αMHC::GFP
D3
45.6%
% Total
Fluorescence (a.i.u.)
αMHC ::GFP
D3
0
255

Figure 3.7 Extrinsic fluorescence intensity of EBs using the MPFC system. The Ti-Sapphire laser was tuned to 890 nm to excite GFP and a 520/35 band-pass emission filter was used to exclude autofluorescence. A nontransfected mESC cell line (D3) and an α-MHC::GFP transfected mESC cell line were used to generate EBs. Histogram analysis of GFP expression of EBs A) pre-MPFC, B) MPFC, and C) post-MPFC. Two separate experiments were conducted and approximately 50 EBs were analyzed per condition (i.e., before, during, and after MPFC). The maximum background intensity was defined such that 95% of the nontransfected EBs expressed mean fluorescence intensity levels below this intensity level (line in histogram). The percentage shown, indicating the fraction of EBs derived from transfected cells expressing GFP, was determined based on the background level. Representative images of D3 and α-MHC::GFP mESC-derived EBs, located directly adjacent to the corresponding plot, are provided for each condition. Color bar represents quantified intensity levels from 0 (black) to 255 (green). a.i.u., arbitrary intensity units. Scale bar, 200 μm.

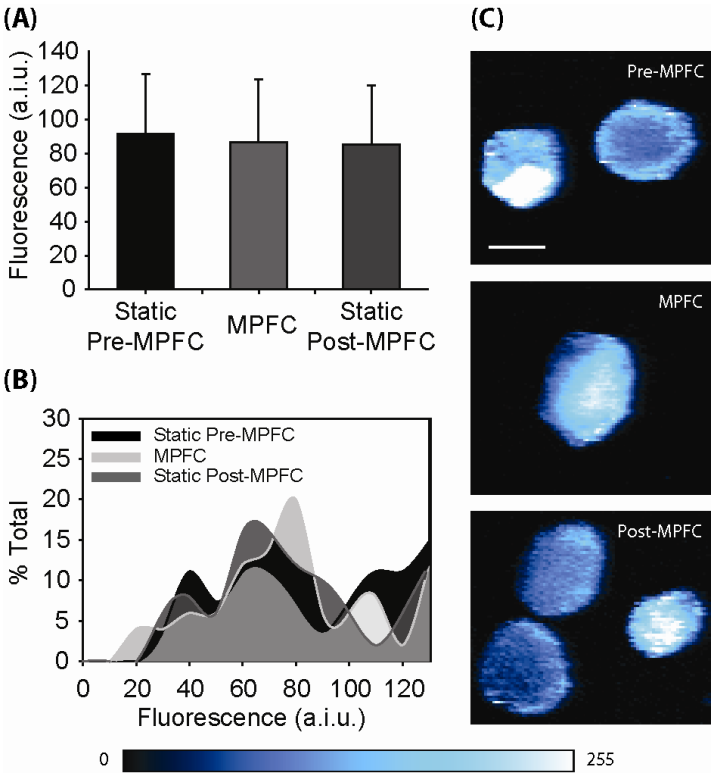

Figure 3.8 Intrinsic fluorescence intensity of EBs using the MPFC system. The Ti:Sapphire laser was tuned to 780 nm to excite the intrinsic fluorescent metabolite, NADH. A) Mean fluorescence intensity of EBs before, during, and after analysis with the MPFC system. Mean fluorescence intensity of EBs did not vary between acquisition conditions (P = 0.55 (pre versus MPFC), P = 0.46 (pre versus post), P = 0.89 (flow versus post)). B) NADH fluorescence intensity distributions before, during, and after analysis. Standard deviations within each condition described in panel A were large, and so the distribution of intensity between samples was compared. Though the distribution was large, the distribution profile did not vary substantially between conditions. C) Representative images depict NADH intensity acquired pre-MPFC, MPFC, and post-MPFC. Localized differences in intrinsic fluorescence were detected in all three conditions. The color bar represents quantified intensity levels from 0 (black) to 255 (white). a.i.u., arbitrary intensity units. Scale bar, 200 µm.

3.6 Discussion

Motivated by the unique challenges of studying stem cells, we generated and validated a proof-of-concept multiphoton flow cytometry (MPFC) instrument, capable of accurate, non-invasive and enhanced-throughput optical analyses of living single cells and multicellular aggregates or bioengineered constructs. The instrument is composed of a flow cell through which large particles stream past a light interrogation point, an optics system with simultaneous transmitted and multiphoton excitation capability and data acquisition software to provide a real-time qualitative and quantitative readout data. In this first study with the MPFC, we focused on analysis of stem cells, however the system is equally capable of analyzing other cell types including pancreatic islets and lymphoblastoid cell lines (data not shown). The components of the system were explicitly designed to garner easy access to the system by both research and clinical laboratories. The integrity of a range of widths (300 - 1600 µm) of the sample stream, speed of image capture and accuracy of image capture were confirmed. In addition, we show reliable determination of expression of GFP, a fluorophore extrinsically incorporated into the cell genome, as well as NADH, a key metabolic coenzyme endogenously expressed in cells. Moreover, NADH fluorescence intensity was measured using both the MPLSM and confocal microscopy, and it was determined that the MPLSM could, in fact, probe significantly deeper into the stem cell aggregate. Additionally, MPLSM could maintain signal in the center of particles at a greater distance from the coverslip than the confocal microscope. Lastly, serial z-sections were compared to single optical z-sections, and it was determined that at a depth of 30 µm, mean intensity of the volume compared to the area measurement were strongly correlated ($R^2 > 0.99$).

The MPFC system can detect extrinsic and intrinsic fluorescence deep in the interior of beads and cell aggregates. This ability is particularly useful for stem cell research because one of the primary challenges of the field is the generation of purified, mature cell types after differentiation in a three-dimensional organization, whether that be part of a multicellular embryoid body or culture in three-dimensional constructs, such as polymer and extracellular matrix-based substrates of a bioengineered tissue construct. To this end, many have established reporter stem cell lines coupled to lineage-specific promoters. While exceedingly valuable, lacking is the ability to detect these reporters in the culture modalities currently used to most efficiently generate differentiated cells because traditional sorting techniques rely on single cell methodologies. Removal of cells from the culture modalities for traditional analyses is known to alter cell fate [81-82] thus a system, such as the MPFC system which can optically characterize the cells prior to removal, is a substantial advance. Here we show that extrinsic fluorescent reporters of

cardiac differentiation of embryonic stem cells can be detected within EBs. The noninvasive depth of penetration and excellent signal to noise ratio afforded by multiphoton excitation yields fluorescence images that are more representative of the entire EB than those obtained with standard epifluorescence microscopy or confocal microscopy. The MPFC retains the 3D benefits of MPLSM and harnesses this in a flow context.

We have characterized the functionality of the MPFC and its applicability to flow analysis of cellular aggregates. The biomedical and clinical application of the MPFC system will be significantly enhanced by the added capacity to sort cells and multicellular entities based on optical properties discerned by the system. For example, EBs expressing lineage-specific reporters (as described above) at high levels could be purified from their counterparts. Molecular profiling could then be conducted on the purified population to discern altered gene and protein expression levels which could be further employed to better understand stem cell biology, and, more practically, to develop better means to efficiently induce and control stem cell differentiation.

CHAPTER 4

Validation and Optimization of Microfluidic Sorting Mechanism

4.1 Specific Objective 2: To sort multicellular entities based on characteristics detected using MPFC

Hypothesis: A novel, microfluidic-based sorting mechanism can be incorporated into the MPFC design to purify populations of large particles (thereby addressing criterion D).

Analysis of cell populations within aggregates or 3D matrices have been mostly limited to low-throughput technologies, which typically require destruction of the sample (e.g., immunofluorescent staining and imaging, western blot, PCR). Still needed are accessible platforms for purification or sorting of large particles based on analysis parameters. Purification of cell aggregates or 3D engineered tissues would be beneficial for many basic biomedical research and clinical applications; examples include, enabling large-scale screens of 3D phenotypes and transplantation of more refined, therapeutically beneficial cell fractions.

For several decades, single cells have been efficiently purified using fluidic sorting techniques, however purification of intact cellular aggregates or 3D microtissues (i.e., large particles, > 100 µm) has been difficult. Purification of large particles requires a coordinated interplay between controlled particle delivery, detection of particles or attributes of particles, and subsequent movement of particles based on those detection parameters. Common cell separation techniques such as magnetic activated cell sorting (MACS) and affinity chromatography columns rely on antibodies or capture molecules to sort cells. Typically, size exclusion prohibits antibodies or other capture molecules from penetrating the center of large particles, which limits labeling to cells at or near the surface. Consequently, purification is based on characteristics of cells at or near the surface and does not necessarily accurately reflect the characteristics of the entire particle. For these reasons, sorting of large particles has been restricted to characteristics derived from optical-based, cellular resolution detection of basic extrinsic cues (i.e. cell permeant dyes [23]), genetically modified cell lines expressing fluorescent reporters or intrinsic properties (i.e. size, shape, autofluorescence).

Despite the limitations in measuring and sorting 3D microtissues, there are ongoing efforts to design efficient large particle sorting mechanisms, in both commercial instruments [19] and microfluidic devices [34-35] (as reviewed in Chapter 2). Future improvements to purify large particles would include sorting based on optical detection of fluorescent labels or autofluorescent molecules of cells of large particles. Microfluidic technology is a

promising approach for optical-based, large particle sorting because (1) the microfluidic flow cell is inexpensive and fabrication is accessible to many research laboratories and (2) the flow cell can easily be added to a wide range of microscopy systems. We are particularly interested in developing a sorting system that can be coupled to our recently developed, enhanced-throughput multiphoton flow cytometry (MPFC) system which is capable of deep optical penetration of large aggregates in the context of flow [5]. In this study, we focus on a microfluidic-based, electromechanical device for sorting large particles (i.e., large particle sorting device, LaPSD) that has the modularity and versatility needed in order to be coupled with our MPFC system and other custom and commercial microscopy platforms. This new device is capable of efficient large particle sorting while maintaining cell viability and long-term function.

4.2 Materials and Methods

4.2.1 Device Description

The LaPSD consists of a single sample input port and two output ports (main and sorting) (**Figure 4.1A-C**). Prior to entering the device, particles are gently and continuously mixed by a floating, PDMS stir bar in a 50 mL conical tube to ensure homogeneous delivery of particles to the flow cell (**Supplementary Figure 1, Appendix**). Particles are drawn through the flow cell via a software controlled syringe pump in reverse mode coupled to the outlet ports (described below). Once delivered to the flow cell, particles are subjected to asymmetric curving channels that use hydrodynamic forces to self-focus and separate particles [83]. This approach has been used successfully for analyzing small particles. The design reduces reagent consumption, reduces the complexity of the setup, and allows for higher throughput. We have modified the design to accommodate large particles, based on practical design rules for inertial focusing previously described [84]. The height of the channel is 1 mm, the typical flow rates utilized range between 400 – 1000 µl/min (adjusted to obtain a particle speed between 1.5-2.0 mm/s), the length of the channel is 6.6 cm and maximum and minimum radius of curvature of the curving channels are 2 mm and 0.3 mm respectively. Theoretically, these flow rates and dimension parameters will accommodate particles in the range of 140 µm to 500 µm [84]. The maximum particle size is limited only by the height of the channel and thus larger particles could be accommodated with altered channel dimensions. The procession of particles passes the optical interrogation point and upon optical detection of a desired event, sorting is triggered. Actuation of sorting is delayed to allow the particle to reach the outlet bifurcation. At the time of actuation, the main outlet closes

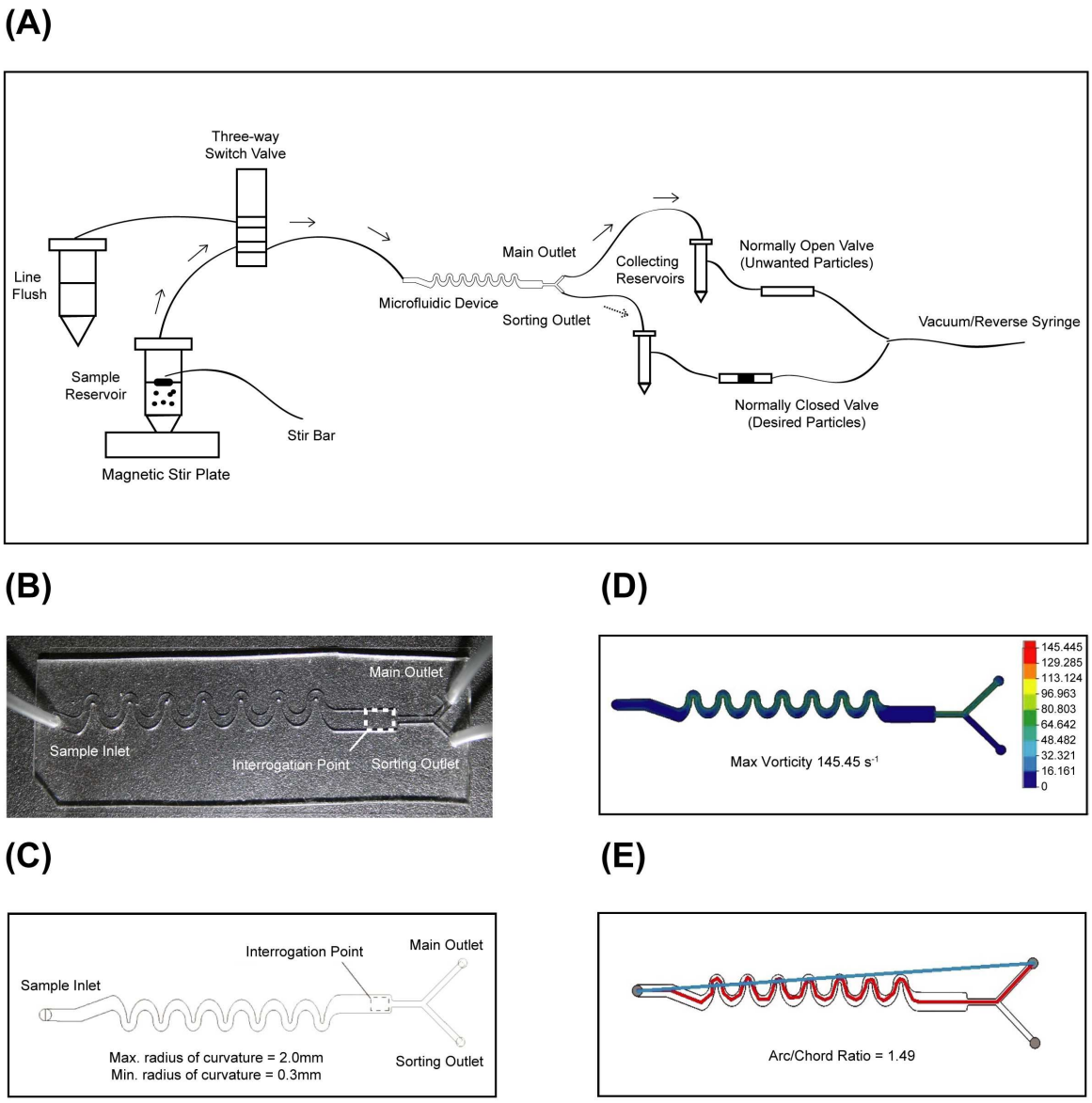

Figure 4.1 Characterization of the LaPSD. A) Schematic depicting the particle flow path. Black arrows denote particle path during main flow. Dotted arrows denote particle path during a sorting event. B) Top view of the LaPSD design consisting of one inlet port, an interrogation region, a main outlet port, and a sorting outlet port. C) Photograph depicting the fabricated LaPSD device, formed by bonding PDMS to glass cover slip. D) 2D colorimetric vorticity plot of the LaPSD. The maximum vorticity during main flow (analogous to sorting flow) is 145 s^{-1}. E) Tortuosity of the LaPSD as defined by the arc to chord ratio is 1.49.

and the sorting outlet opens (1-3 s, time delay; 0.1-1.0 s, actuation time). Main and sorting outlets are opened and closed via software-controlled microvalves that are linked to the syringe pump by way of an in-line y-connector. After sorting, the sorting outlet closes and main outlet opens. Sorted and unsorted particles are collected in reservoirs coupled to the fluidic lines prior to the microvalves to avoid clogging of the valves. The collection reservoirs are 15ml conical tubes, which are filled with 1X phosphate buffered saline (PBS) to maintain driving pressure by avoiding air compression. A software controlled three-way solenoid pinch valve (Cole Parmer, Vernon Hills, IL) is used to rinse the flow cell and fluidic lines between large particle samples.

4.2.2 Sorting Efficiency

Two separate polystyrene bead mixtures were employed to test the sorting efficiency of the LaPSD. For Solution 1, the initial bead population consisted of ~16% fluorescent beads and ~84% nonfluorescent beads, for solution 2 the initial bead population consisted of ~31% fluorescent beads and ~67% nonfluorescent beads. Both solutions were prepared by mixing fluorescent polystyrene beads with non-fluorescent polystyrene beads measuring 160 µm in nominal diameter (Duke Scientific Corporation, Palo Alta, CA). Aliquots of solution 1 were counted with an Axiovert 40 CFL inverted fluorescence microscope (Zeiss, Thornwood, NY) and the concentration of fluorescent beads was determined to be 16% $\pm$ 11%. The total concentration of beads of solution 1 was determined to be 18 $\pm$ 5 beads/ml. Aliquots of solution 2 were also counted and the concentration of fluorescent beads determined to be 31% $\pm$ 3%. The total concentration of beads of solution 2 was 16 $\pm$ 5 beads/ml. Solutions were loaded into the sample reservoir of the LaPSD and the LaPSD was positioned on the stage to correspond to the interrogation point of a multiphoton microscopy system as previously described. Fluorescence levels of beads were determined using WiscScan acquisition software (http://loci.wisc.edu/software/wiscscan) of the MPFC system with the following software and hardware modifications to accommodate electromechanical switching mechanisms required for sorting. In particular, particle size and intensity parameters were set to identify "positive" events. When positive events were detected, the software sent a 5V signal to the DAQ card (National Instruments, Austin, TX), which rapidly (0.3 ms) switched the microvalve state. A user defined positive event cued both outputs to switch states for a specified amount of time (actuation time). The time-delay functionality allowed a user to delay the switch of channel state up to 3 seconds (with millisecond discrimination) after optical interrogation. After sorting, beads were collected from sorting or main flow outlets and counted on a fluorescence microscope. Sorting

efficiency or purity was defined as the number of desired particles divided by the total number of particles in the sorting outlet reservoir. To account for the initial concentrations of desired particles, we also report an enrichment ratio defined as the ratio of desired particles to undesired particles in the sorting outlet reservoir divided by the ratio of desired particles to undesired particles introduced into the sample inlet (determined by counting particles collected in both outlet ports, **Table 4.1** [85]). The average sorting efficiency and the average enrichment ratio were established by first determining the efficiency or enrichment per trial and then calculating the average.

4.2.3 Preparation of Cell Aggregates

HM1 mouse embryonic stem cells (Open Biosystems, Huntsville, AL) were used to generate embryoid bodies (EBs) as previously described [5]. Briefly, EBs were left in hanging drops for 3 days and then introduced into the microfluidic device. Approximately one third of all harvested EBs were stained using CellTracker^{TM} green (Molecular Probes, Eugene, OR). Briefly, EBs were rinsed in 1X PBS, and next incubated for 30 minutes at 37^{o}C and 5% CO2 in cell culture medium without FBS, containing 5 µM CellTracker^{TM} green (Molecular Probes). Stained EBs were mixed with unstained EBs to yield an EB suspension with ~33% of EBs fluorescently labeled. This solution was loaded into the sample reservoir of the LaPSD. "Positive particles" were defined as those with fluorescent label and the software was set to actuate with detection of a positive event. Sorting efficiency and enrichment ratio were determined as defined above for sorting of fluorescent beads (**Table 4.1**).

4.2.4 Cell Aggregate Viability and Functional Analysis

EBs were generated as described above [5] and were left in hanging drops for 3 days. EBs were then harvested and stained using CellTracker^{TM} green (Molecular Probes, Eugene, OR). Briefly, EBs were rinsed in 1X PBS, and next incubated for 30 minutes at 37^{o}C and 5% CO2 in cell culture medium without FBS, containing 5 µM CellTracker^{TM} green (Molecular Probes). Stained EBs were introduced into the LaPSD, optically scanned using multiphoton excitation and retrieved in the main outlet port. Collected EBs were counted, assessed for changes in morphology, and subsequently plated on culture surfaces to assess attachment and ability to form areas of spontaneous beating indicative of cardiomyocyte function.

Table 4.1 Sorting efficiency and enrichment ratio of large polystyrene beads and EBs

	Large Beads			EBs		
Trial	Input Concentration (% Fluorescent Particle of Total)	Sorting Efficiency (Output Concentration; % Fluorescent Particle of Total)	Enrichment Ratio	Input Concentration (% Fluorescent Particle of Total)	Sorting Efficiency (Output Concentration; % Fluorescent Particle of Total)	Enrichment Ratio
1	21	100	44.5	31	68	4.7
2	20	100	20.0	39	100	24.7
3	11	85	42.5	39	94	25.3
4	12	82	33.9	33	100	6.0
5	32	79	8.3	29	68	5.1
6	34	86	11.4	33	100	14.0
7	29	85	13.6	41	86	8.5
8	28	69	5.7	33	82	9.2

4.2.5 Statistical Analysis

For comparison of EB attachment, cardiomyocyte function in EBs with and without introduction into the LaPSD and for comparison of sorting efficiency and enrichment between devices and between types of large particles (i.e., beads and EBs), a normal distribution was assumed and one-way analyses of variance (ANOVA) and Student *t*-test were used. Data were reported as average $\pm$ standard deviation and were analyzed with JMP 5.0.1 for Windows (SAS Institute, Inc., Carey, NC). A 99% confidence ($P < 0.01$) interval was applied for statistical significance.

4.3 Fluid Dynamic Profiles of the LaPSD

To begin to characterize the fluid microenvironment experienced by large particles in the LaPSD, wall shear stress incurred by the fluid in the LaPSD was determined. Newtonian fluids moving along a solid wall of a microfluidic channel will sustain a shear stress near the wall surface that is proportional to the viscosity of the fluid and flow velocity and inversely proportional to the channel height. Wall shear stress has long been correlated to viability of cells that adhere to the wall surface [86] and cells that are suspended in flow channels [87-88]. The level of wall shear stress found to cause death of adherent cell types (0.1 – 1 Pa) [86] is much lower than that found to cause death of suspended cell types (100 – 500 Pa) [87-88]. This is not surprising since cells in suspension rarely and transiently occupy the space near the wall (especially in this case in which suspended particles are hydrodynamically focused to the channel center-line) and so do not experience the maximum shear stress of a channel. The maximum wall shear stress of the microfluidic sorting device is 0.08 Pa, which is two orders of magnitude lower that the wall shear stress previously found to induce death of cells in suspension [87-88]. However, large particles are prone to rolling along the base of the channel if they are not hydrodynamically focused in the z plane. In this case, wall-induced lift forces, created by squeezing of fluid between the sphere and the wall during contact, tend to increase drag in the direction of motion [89]. In addition, large particles tend to impact on each other at dense particle concentrations [89]. Although relatively dilute particle concentrations were used in these studies, particle-particle interactions are still visible. A phenomenon known as drafting, kissing and tumbling (DKT) is the dominant interaction of particles in the LaPSD [89-90]. This interaction can directly impact on the viability and functional capacity of the cells of large particles and typically occurs in channel geometries that impose a high degree of vorticity and/or tortuosity. Thus these parameters were assessed in greater detail. (Additional

microfluidic device designs were considered and these were evaluated as well (**Supplementary Figures 2, 3; Appendix**).

Vorticity is a local measure of fluid rotation with respect to adjacent fluid. SolidWorks software (Solidworks Corp, Concord, MA) models vorticity by meshing a 3D volume of fluid into small voxels and computing vorticity for each voxel. Vorticity is a vector and has velocity component and rotational components. Vorticity calculations for the device were conducted using SolidWorks Flow Simulation Software (Dassault Systemes, SolidWorks Corp, Concord, MA). The contour plot (**Figure 4.1D**) reports the vector as a positive number in rad/s (or s^{-1}). The contour plot shown in Figure 1D is a 2D section of the 3D fluid volume in the LaPSD. These sections are located at the mid-height of the channel. The fluid in the LaPSD exhibits a relatively high level of vorticity during main flow and with sorting (145 s^{-1}), but not substantially different from alternative device designs known to maintain cell viability (**Supplementary Figures 2, 3; Appendix**)

Tortuosity is a measure of the divergence of a path from a straight line and is defined here as the ratio of the length of the particle path to the length of the straight-line path from the particle inlet to the particle outlet (i.e., arc/chord ratio). A depiction of the device showing the particle path and the straight line path is shown in **Figure 4.1E**. The arc/chord ratio of the LaPSD was 1.49 and so substantially higher than alternative device designs known to preserve viability. Given the increased tortuosity of the microfluidic sorting device and the propensity for fluid dynamic forces to compromise cell viability by interrupting cell-cell and cell-matrix interactions and/or by damaging cell membranes, we sought to test the viability of cells of large particles after transit through the LaPSD.

4.4 Viability and Function of Stem Cells of Large Aggregates after Flow through the LaPSD

To test whether the additional forces imposed by the LaPSD, due to increased wall shear stress, vorticity and tortuosity, would compromise viability of cell aggregates, we introduced fluorescently labelled, stem cell aggregates (i.e., EBs; n = 21, 28, 32 in each of three separate experiments) into the sample inlet at a maximum volumetric flow rate of 800 µl/min. EBs were optically detected at the interrogation point and then collected and counted at the main outlet. It was determined that 92% $\pm$ 8% of EBs were recovered and of those EBs recovered, 97% $\pm$ 3% attached to 2%, P = 0.60, **Figure 4.2**). The stem cell line used to generate the EBs has a strong capacity for forming spontaneously beating areas (indicative of cardiomyocyte differentiation) when exposed to qualified serum. Thus, we counted the number of EBs that gave rise to beating areas after flow through the device compared to controls (no

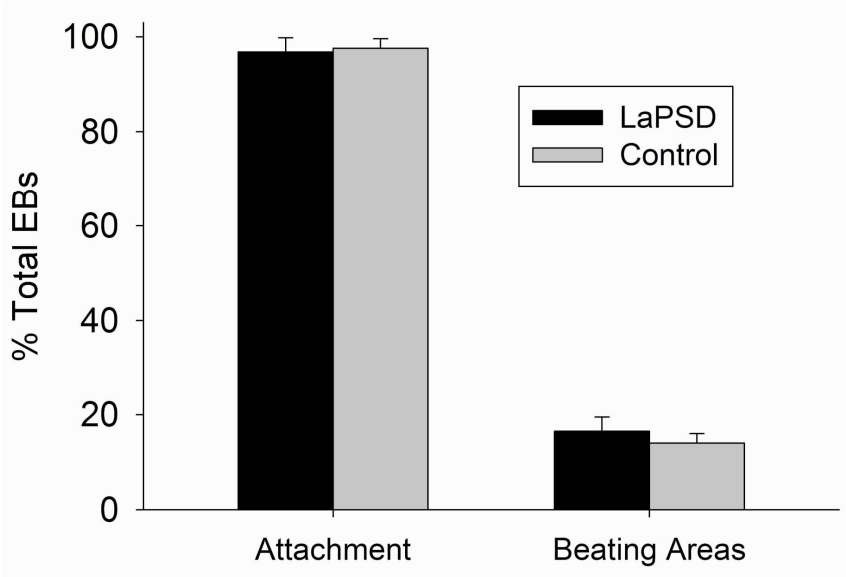

Figure 4.2 Viability and long-term function of stem cell aggregates following flow through the LaPSD. Fluorescently labelled EBs were introduced into the device through the sample inlet, optically interrogated and removed via the main outlet. After removal, EBs were placed in culture plates and the number of EBs that attached were counted and reported as a percentage of the total number of EBs plated compared to control EBs that were generated at the same time, but placed immediately in static culture dishes. In addition, EBs were tracked over time and the percentage of EBs with functional cardiomyocytes (i.e., beating areas) was determined. Attachment and beating functionality were not significantly altered with flow through the LaPSD compared to controls (P = 0.60 and 0.33 respectively). Error bars correspond to standard deviation from the mean.

flow). The capacity to form beating areas by day 8 of differentiation (5 days post plating) in EBs after flow through gelatin-coated culture plates. This percentage was not statistically different from attachment of control EBs (98% ± the LaPSD (16% ± 3%) was not statistically different from control EBs (14 ± 2%, $P = 0.33$). Thus EB attachment and differentiation potential did not differ between these groups suggesting flow through the LaPSD did not alter the viability and ultimate function of stem cells of large aggregates.

4.5 Sorting efficiency of the LaPSD

4.5.1 Sorting fluorescent vs. non-fluorescent polystyrene beads

To test the ability of the LaPSD to purify populations of large particles we introduced bead populations with a known fraction of fluorescent and non-fluorescent beads. The size distribution of the polystyrene beads, based on specifications of the manufacturer, was 158 ± 3 µm, with a coefficient of variation of 2.2%. We measured the cross sectional area of the beads using the oval tool in ImageJ [60] , in a similar fashion to measurement of cell aggregate size, and determined the average diameter to be 157 ± 3 µm, with a coefficient of variation of 1.9%. The measured bead diameters were displayed in a histogram to demonstrate the relative uniformity of the samples (**Figure 4.3A, B**). As a result, tight focusing is accomplished in the LaPSD, with spheres of relatively uniform size and shape (**Figure 4.3C) .** The valve corresponding to the sorting inlet was actuated upon detection of a fluorescent bead and the final fraction of fluorescent particles in the sorting outlet was reported as the sorting efficiency ("positive" selection) and was the concentration used to determine the enrichment ratio. Sorting efficiencies of 92 ± 10% (solution 1, n = 4 trials), and 80 ± 8% (solution 2, n = 4 trials) were attained using the LaPSD. Moreover, enrichment ratios of 35.2 ± 11.1 (for solution 1), and 9.7 ± 3.5 (for solution 2) were achieved (**Figure 4.3D**).

4.5.2 Sorting Fluorescent vs. Non-Fluorescent EBs

To test the ability of the LaPSD to purify populations of large cellular aggregates, we generated a mixed suspension of fluorescently labelled and unlabelled EBs (33% fluorescent:67% nonfluorescent, similar to bead solution 2 above). Two separate EB suspensions (or groups) were generated in this way and prior to each trial (n = 4 trials for each group, n = ~ 75 EBs per trial) the relative size distribution of EBs was determined (group 1, mean diameter = 247 ± 20 µm; group 2, mean diameter = 295 ± 12µm) (**Figure 4.4A, B**). Size and shape of cell aggregates are the primary determinants in the ultimate particle velocity. For an estimation of particle velocity, standard curves were

made varying both volumetric flow rates and known polystyrene bead sizes(Appendix). Two separate EB groups were used to test the ability of the instrument to efficiently sort various size ranges of particles with inherent differences in particle velocities (**Figure 4.4C**). Sorting efficiency obtained for group 1 was 91 $\pm$ 15% and group 2 was 84 $\pm$ 13%. Group 1 EBs had an enrichment ratio of 15.2 $\pm$ 11.4 and group 2 EBs had an enrichment ratio of 9.2 $\pm$ 2.6 (**Figure 4.4D**). Sorting efficiencies and enrichment ratios of both groups of EBs were statistically similar to that of bead sorting results with similar starting concentrations of fluorescent particles (i.e., bead solution 2 compared to the 33% EB solution).

4.6 Discussion

Motivated by the growing need to purify populations of large cellular aggregates or microtissues, a new microfluidic, electromechanical, enhanced-throughput sorting device, termed LaPSD, was designed and evaluated based on its ability to preserve cell health and yield high sorting efficiencies. Device optimization was driven by the primary objective of our laboratory, to assess all cells within a stem cell aggregate in an enhanced-throughput way and to purify aggregate populations based on this assessment. Several other applications can be envisioned which would benefit from the ability to rapidly purify large particles in the fields of basic cell biology and clinical therapy. The LaPSD was designed with several important features to promote ease of use and elevated sorting efficiency. First, the asymmetric curving channel allowed for sheath-less particle focusing. Elimination of sheath fluid was important because it decreased the lateral distance required to divert a particle upon selection. When attempting to divert particles across the sheath stream (see alternative designs, **Appendix**), trailing particles were often diverted and so increased the percentage of contaminating or unwanted particles in the sorting outlet/reservoir. In addition, disrupted sheath flow could alter the flow path of the sample stream and thereby push subsequent particles outside of the interrogation region. In this case, wanted particles were often missed. Second, a time delay was incorporated between the time of optical detection and the time of actuation of the sorting valve to improve sorting efficiency. The time delay was necessary because channel dimensions at the point of optical interrogation (distal to the asymmetric curving channel) were increased three fold to effectively decelerate particle velocity to accommodate

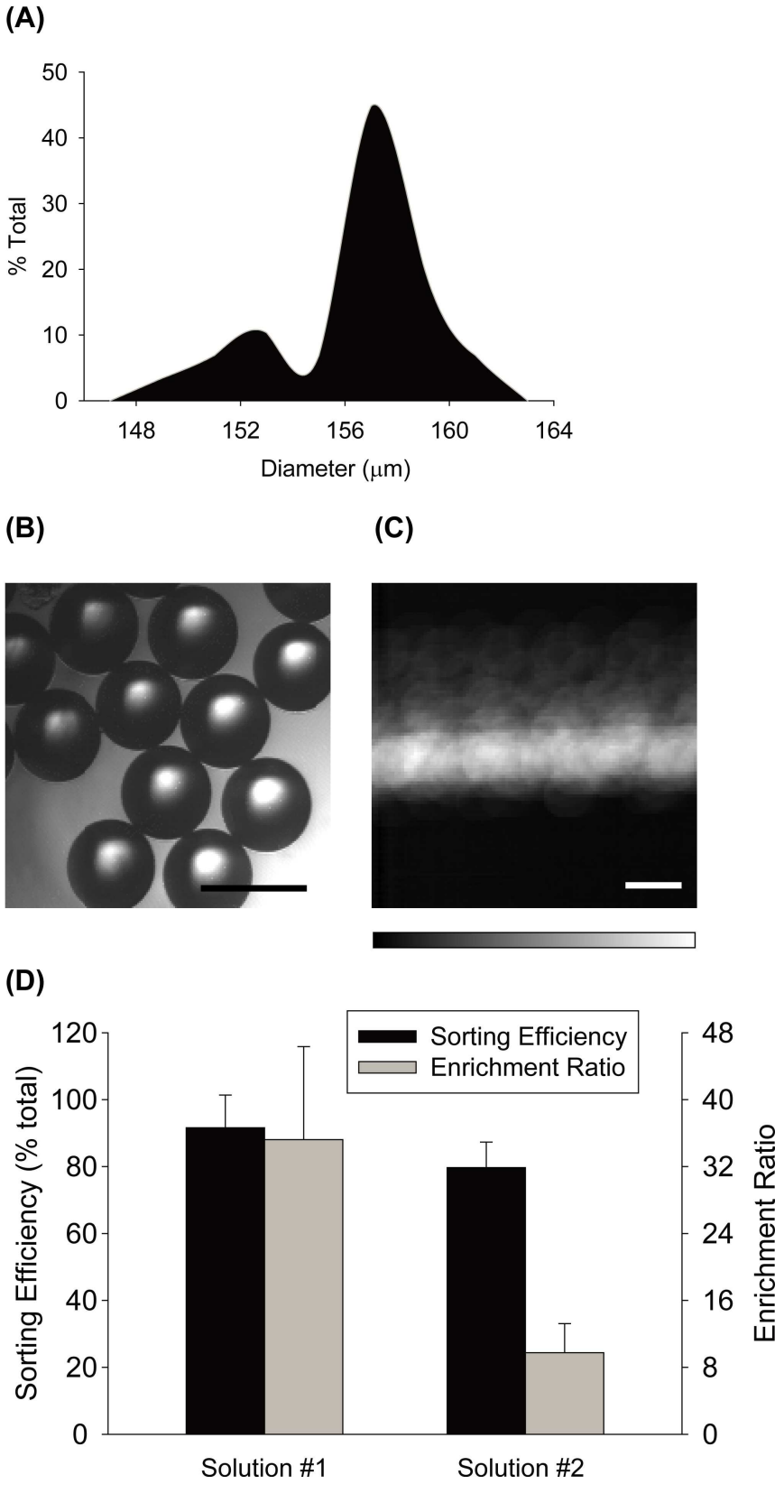
(A)
50
40
30
20
10
0
% Total
148
152
156
160
164
Diameter (μm)
(B)
(C)
(D)
Sorting Efficiency
Enrichment Ratio
120
100
80
60
40
20
0
Sorting Efficiency (% total)
48
40
32
24
16
8
0
Enrichment Ratio
Solution #1
Solution #2

Figure 4.3 Sorting efficiency and enrichment ratio of polystyrene beads. A) Histogram depicting the distribution of bead diameters in a representative fraction of fluorescent and non-fluorescent polystyrene beads. Measured bead diameter (157 $\pm$ 3 µm) did not differ statistically from manufacturer's specifications (158 $\pm$ 3 µm). B) Bright field image of polystyrene beads. Scale bar = 200 µm. C) Summation of temporal image series of beads flowing through the LaPSD. Fluorescence intensity images of beads were taken every 0.2 s and ~3000 images were merged to create the image shown. The minimal deviation of fluorescence intensity from the center sample stream line conveys the ability of the LaPSD to effectively focus particles with uniform size. Scale bar = 200 µm. D) Sorting efficiency and enrichment ratio of bead populations consisting of fluorescent and nonfluorescent beads. Solution 1 attained significantly higher enrichment ratios due to a low starting concentration of fluorescent beads; this result demonstrates the ability of the LaPSD to effectively purify particles from relatively dilute starting concentrations akin to rare cell populations. Error bars correspond to standard deviation from the mean.

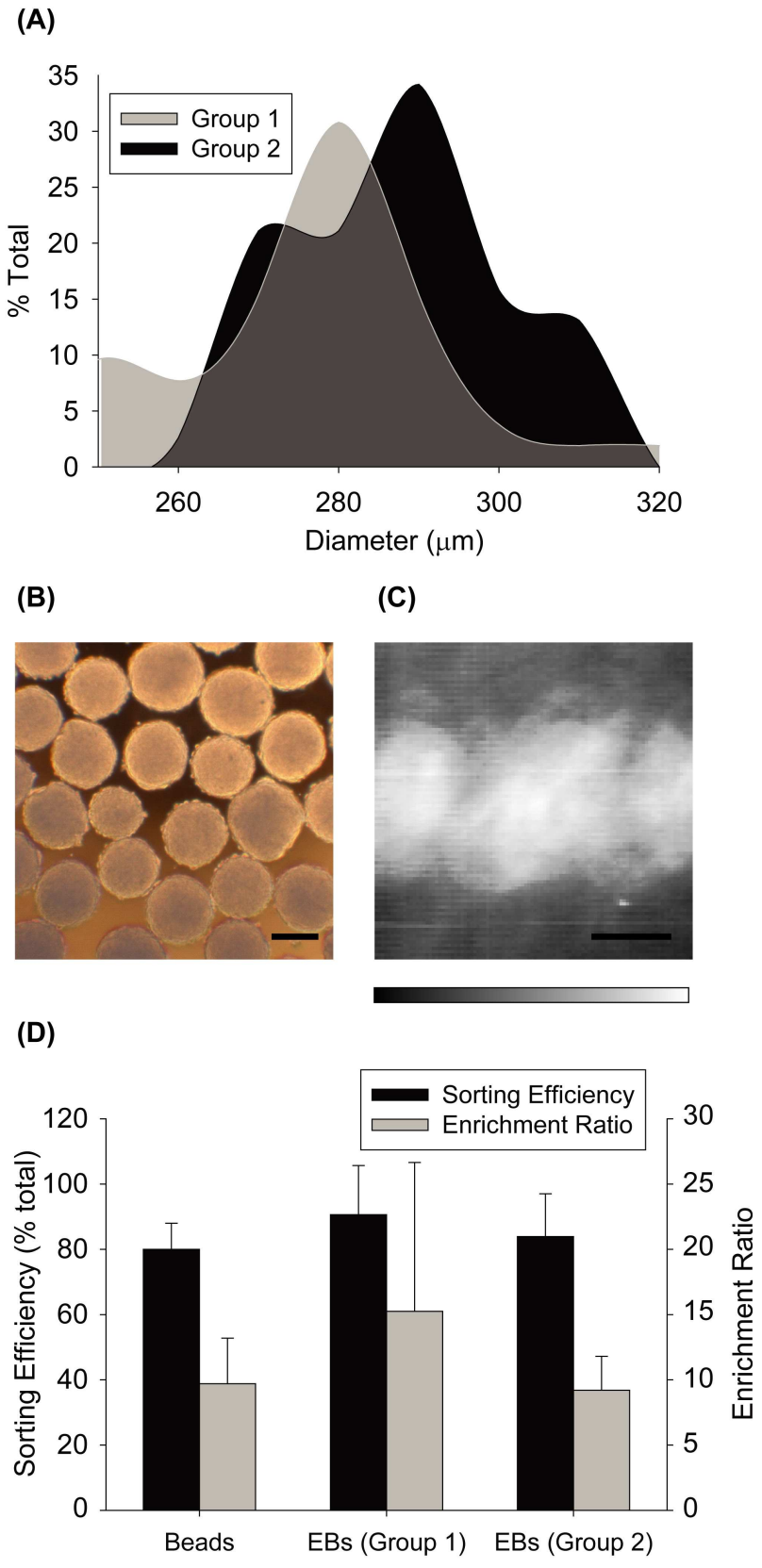
(A)
Group 1
Group 2
% Total
Diameter (μm)
(B)
(C)
(D)
Sorting Efficiency
Enrichment Ratio
Sorting Efficiency (% total)
Enrichment Ratio
Beads
EBs (Group 1)
EBs (Group 2)

Figure 4.4 Sorting efficiency and enrichment ratio of embryoid bodies. A) Histograms depicting measured EB diameters for two separate groups of EBs. Measured mean EB diameter were 247 ± 20 µm for group 1, and 295 ± 12 µm for group 2. B) Bright field images of EBs. Scale bar = 200 µm. C) Summation of temporal image series of EBs flowing through the LaPSD. Fluorescence intensity images of EBs were taken every 0.2 s and ~2000 images were merged to create the image shown. The deviation of fluorescence intensity from the center sample stream line is more diffuse than that observed for beads reflecting the higher variability of size of EBs and therefore greater perturbation of flow. Scale bar = 200µm. D) Sorting efficiency and enrichment ratio of EB groups compared to that of bead solution 2. There was no significant difference between sorting efficiency or enrichment ratios when comparing beads to either group of EBs. Error bars correspond to standard deviation from the mean.

the relatively slow scan speeds (~5 frames/sec) of the MPFC system. Channel dimensions were subsequently decreased to accelerate particle velocity and decrease the volume of fluid that would change direction during a sorting pulse. In addition, a 5 mm separation distance from the interrogation region to the sorting bifurcation ensured that a sorting pulse would not alter the flow path of particles at the optical interrogation point. Third, the LaPSD functions without an additional pressure source to divert the particles, thereby reducing unnecessary stress that may be harmful to the structure of cellular aggregates. Instead, particles are diverted by simply switching the direction of the particle path while maintaining a uniform internal pressure within the microfluidic device and consistent particle positioning along natural streamlines. The exclusion of a pressure source to divert particles also reduces manufacturing complexity, reduces volumes of reagents needed and improves accessibility or the ability to be replicated in other laboratories.

One potential drawback of the LaPSD is the requirement of precise particle velocity to define the time delay from interrogation to sorting. If precise geometrical measurements can be made on the devices and inlet pressures can be tightly controlled, theoretical calculations may suffice, as was the case in these studies. Alternatively, a flow probe or video capture of particles in flow may be necessary to more accurately determine particle velocities and associated variability before sorting. In addition, as populations of cells (or large particles) become more diverse in size, their respective position along the horizontal and vertical velocity profile will vary. At our current flow rates, particles tend to flow along the bottom of the flow cell. Lateral displacement will be altered with changes to the volumetric flow rate of the inlets and the size of the particles. This might be especially problematic in the case of time-delayed sorting (as described here) if particle velocities vary outside of the predicted range. To further improve sorting efficiencies of this design, 3D focusing could be implemented to more precisely control particle position in the channel and thereby particle velocities [91].

An additional consideration for implementation of the devices reported here is the design of software that is capable of defining a positive event based on an optical input. One or more signals must be relayed to a DAQ card to execute a given sorting event. To begin to study microtissues expressing non-contiguous fluorescence intensity, improvements to real-time data acquisition will include gating based on bright field images (size) to allow for spatial discrimination of fluorescence within the aggregate or microtissue. This type of detection and real-time image processing will allow for biologically relevant sorting studies including, for example, isolating aggregates with high

ratios of living cells to dead cells based on live/dead fluorescence indicators or isolating microtissues containing differentiated cell types based fluorescent reporters coupled to lineage specific genes.

CHAPTER 5

Sorting of Microtissues based on Non-Contiguous Fluorescence Intensity

5.1 Specific Objective 3: To use the MPFC system to non-invasively purify populations of stem cell aggregates and to assess the functional capacity of sorted populations. Hypothesis: Purified populations of EBs, detected and sorted on the MPFC based on fluorescent indicators of cell phenotype and viability, will have increased functional capacity when compared to unpurified populations of EBs.

Pluripotent stem cells, isolated from mammalian embryos or induced from mature cell types, are highly proliferative and can differentiate into most cell types of the body [92-94]. These attributes render them attractive for studying tissue development or the pathogenesis of disease progression as well as for drug testing and cellular therapies. Effective control of stem cell state largely dictates the utility of pluripotent stem cells for research and clinical application. Thus, significant research effort has been dedicated to delineating mechanisms that either maintain pluripotency [95] or drive differentiation [96]. The embryoid body (EB), an aggregate of pluripotent stem cells that roughly recapitulates the complex assembly of cell-cell and cell-matrix adhesions and corresponding intercellular signaling of embryogenesis, is commonly utilized to drive differentiation *in vitro*. Although more defined methods have been developed to direct differentiation of individual cell types, such as two-dimensional formats (i.e., monolayer culture) with defined soluble (e.g., growth factors, recombinant DNA encoding essential transcription factors) and/or defined insoluble substrates (e.g., extracellular matrix proteins), the EB remains an invaluable *in vitro* model to study the complex signaling interplay that impacts the state of a stem cell or stem cell progeny with: 1) development, 2) extended *ex vivo* culture or 3) following transplantation to a native tissue.

The primary challenge of studying cells of the EB is their propensity to change state after common research manipulations such as the addition of exogenous labels (e.g., antibody staining) [97] and disaggregation [1-2]. Therefore, to probe interior cells of the EB, investigators were previously limited to terminal, low throughput cell and molecular biology techniques including staining of histological sections and PCR analysis of extracted RNA. More recently, the development of fluorescent reporter constructs coupled to differentiation-specific gene expression and combined with advanced imaging modalities capable of non-invasively imaging deep within a biological specimen (e.g., confocal and multiphoton fluorescence microscopy), enables investigators to probe cells in the interior of living EBs. To enhance the throughput of this type of analysis, we recently coupled multiphoton laser

scanning microscopy [36] with a microfluidic-based flow cell, creating an imaging flow cytometry system (Multiphoton Flow Cytometer, MPFC) [5] capable of non-invasively detecting size and fluorescence properties deep in the interior of large intact multicellular aggregates, such as EBs. This was an important advance as large numbers of EBs can be quickly assessed, improving study power as well as the ability to distinguish important biological events from noise without relying on expensive arrays or time-consuming serial imaging.

Analysis of EBs for both research and clinical application would be further improved if the EBs could be purified based on characteristics that precede and/or predict a differentiation state of interest without disrupting EB organization. One relevant application pertains to the differentiation of cardiac cell types for the recovery of lost myocardial function. This application dictates a need for identifying and examining cellular aggregates with enhanced cardiac potential to understand the environment, signals and corresponding mechanisms that contribute to cardiac differentiation. For example, it has been shown that EB size can influence the proportion of cells that enter the cardiac lineage [98-99], thus identifying and segregating EBs on size soon after EB formation could provide a population of EBs with increased cardiac potential. Similarly, the presence of cardiac progenitor pools has been linked to the generation of mature cardiac cell types and not unwanted cell types *in vivo* [100]. Unknown, however, are the conditions that contribute to behaviors of these cardiac precursors, including proliferation, migration and differentiation into individual cardiac cell types. Thus, the ability to purify EBs based on characteristics early in development (i.e., size or presence of cardiac precursors) associated with generation of a particular cell type while maintaining aggregate viability and structure would provide an important tool for subsequent studies of differentiation.

Here we demonstrate the ability to purify intact EBs based on size or intensity of a fluorescent reporter corresponding to expression of NKX2-5, an early cardiac transcription factor [100]. Purified EBs were monitored over several days to determine whether developmental outcome, namely the generation of mature cardiomyocytes, corresponded to size or reporter expression. To enable this study, we enhanced the detection software of our previously described MPFC system [6] to permit sorting of EBs based on real-time measurements of size and spatially segregated fluorescence. As a result, we show that purified populations of EBs with high NKX2-5 expression at early time points in differentiation are more prone to form beating areas at later time points. Furthermore, the largest EBs within a broad size distribution have the highest potential for forming beating areas and producing the highest percentage of cardiomyocytes per EB.

5.2 Materials and Methods

5.2.1 Cell Culture

Induced pluripotent stem (iPS) cells carrying a NKX2-5 Emerald Green Fluorescent Protein (EmGFP) Bacterial Artificial Chromosome (BAC reporter), referred to as NKX2-5 GFP iPS cells [100] were cultured in Dulbecco's Modified Eagle's Medium (DMEM + Glutamax, Invitrogen) with 10% Fetal Bovine Serum (FBS; Invitrogen), 11% Non-essential amino acids, (Invitrogen) and 0.0007% (1% of a 35 ml/50 ml solution) β-mercaptoethanol (MP Biomedicals LLC, Solon, Ohio). To maintain pluripotency, media was supplemented with Leukemia Inhibitory Factor (LIF, Millipore, Billerica, MA) at 2000 U/ml. Embryoid bodies (EBs) were made via the hanging drop method (day 0) [66]. iPSCs were harvested and resuspended in DMEM + 10% FBS (no LIF or BMP-4) at 1.6 x 10^4 cells/ml. This cell suspension was used to make 30 µl hanging drops over 1x PBS in 100 mm Petri dishes, resulting in initial concentration of 500 cells per drop. For the size separation experiment, additional plates of 200 and 400 cells per drop were prepared to broaden the size distribution of the total population of EBs. EBs were harvested 3 and 4 days after formation (day 3, 4), for sorting experiments based on the fluorescent reporter, NKX2-5, and sorting based on size, respectively.

5.2.2 MPFC Operation

EBs were imaged on the MPFC with optical configuration similar to that previously reported [5-6]. Briefly, simultaneous bright field and intensity images were taken with a Plan Apo VC 10X air objective (Nikon, Mehlville, NY) at a resolution of 128 x 128 and pixel integration of 4, resulting in a scan rate of approximately 5.5 frames per second. The Ti:Sapphire laser (Spectra Physics, Santa Clara, CA) was tuned to 890 nm, resulting in an average power at the sample of approximately 20 mW. A 520/35 nm bandpass filter (Chroma Technology Corporation, Rockingham, VT) was used to collect GFP emission from the EBs. Power and gain settings were set such that less than 5% of pixels were saturated and background noise was kept to a minimum. Bright field and intensity images were collected using in-house developed software (WiscScan). Fluorescence and size measurements of EBs were made using ImageJ software. For analysis, background levels were identified such that less than 10% of pixels on a background image (i.e., containing no EBs) were saturated for all conditions.

5.2.3 Assessment for Cardiomyocyte Function and Immunofluorescence Staining

Imaged EBs were placed in an incubator overnight and analyzed for attachment on the following day. Each subsequent day, medium was replenished in the 6 well plate and the percentage of EBs displaying beating areas was recorded on day 7 of differentiation. Immediately following observation, EBs were fixed with 4% paraformaldehyde and stained for cardiac troponin (cTnT). The National Stem Cell Bank protocol (www.wicell.org, SOP-CH-210C) for immunolabeling of cardiac markers in EBs was utilized for this assessment. Mouse anti-troponin T (cardiac isoform Ab-1, cTnT, clone 13-11, Fisher Scientific, Pittsburg, PA) primary antibody and goat anti-mouse Alexa Fluor 568 (Molecular Probes/Invitrogen, Carlsbad, CA) secondary antibody were used. Fluorescence images were acquired using a Zeiss Axiovert 40CFL inverted microscope (Zeiss, Germany) with a 4X objective, using a 560/55 nm bandpass excitation filter and 645/75 bandpass emission filter.

5.2.4 Flow Cytometry Applications of WiscScan Software

All real-time particle analysis was carried out by the WiscScan acquisition software. WiscScan integrates ImageJ [101], an open source, Java-based image processing program, for all image calculations. Two primary image-processing functions were implemented on particles in flow, namely size and fluorescence intensity per unit area. A results table is displayed during an acquisition trial recording the optical imaging plane in which a particle is detected, the corresponding particle area (size), number of intensity pixels above background, the mean intensity of pixels above background (intensity), and the total intensity divided by particle area (intensity per unit area). The user can then define parameters on which to sort, by checking the corresponding box in WiscScan.

To begin acquisition, the background intensity applied to unmodified images, as well as the minimum particle size to be detected must be defined. This ensures that debris will not be detected or be sorted as a false positive event. Before performing a sorting trial, a pre-sort analysis trial is executed with a representative sample population, to acquire distributions of sample size, and intensity per unit area. From the acquired results table, the user can decide which of the parameters to sort based on, as well as the lower and upper bounds of that parameter to isolate a population of interest.

5.2.5 Timing

Sorting trials are performed in real-time, and so program timing becomes a critical factor to obtain high sorting efficiency. At current acquisition resolutions, WiscScan acquires image frames between 0.1720 and 0.1880 seconds per frame (5.31 to 5.81 frames per second), requiring all ImageJ calculations to be complete at least 30 ms before the next image frame is loaded, allowing for adequate time to signal the data acquisition card and sorting valves. The major tasks that must be completed within the 150 ms allowance are to display any required images from WiscScan in ImageJ, carry out appropriate image calculations, compare results with user-defined values, and signal capture. Over the course of 5000 frames (~15 minutes), measurement calculations in ImageJ were completed in an average time of 8.7 ms and 63.2 ms, for the size and intensity per unit area measurements, respectively. Thus, image processing algorithms are easily completed in the allotted 150 ms, and do not restrict the throughput of the MPFC.

5.2.6 Statistical Analysis

For comparison of size, NKX2-5 expression, beating areas and cardiac Troponin T expression between sorted and unsorted EB populations on day 7 of differentiation, a normal distribution was assumed and one-way analyses of variance (ANOVA) and Student *t*-test for unpaired samples were used. Data were reported as average $\pm$ standard deviation and were analyzed with JMP 5.0.1 for Windows (SAS Institute, Inc., Carey, NC). A 95% confidence ($P < 0.05$) interval was applied for statistical significance.

5.3 Utilization of a Segmentation Algorithm for Real-Time Measurement of Non-Contiguous Fluorescence Intensity

Previously, we used the MPFC to sort EBs based on contiguous fluorescence intensity within an EB [6] so that EBs could be effectively distinguished from fluorescent noise. This was accomplished by coupling our in house developed laser scanning acquisition software, WiscScan, with ImageJ [101] based analysis tools for real time large particle analysis in flow. ImageJ was chosen due to its wide array of existing analysis routines, ease of adaptability and customization and ability to run both within WiscScan at acquisition or as a standalone application for further analysis after acquisition. The ImageJ analysis routine, “Analyze Particles” was utilized to measure connected clusters of pixels above background intensity. In this way, the size and intensity of large particles with continuous

fluorescence throughout the particle could be determined. However, this implementation could not define the border of a large particle in real-time in the absence of fluorescence intensity. This was disadvantageous as it limited the utility of MPFC as different collection speeds, variable fluorescence expression levels or changes in focus can all affect detectable fluorescence at the periphery. To overcome this we wanted to exploit a beneficial optical feature of the MPFC, it not only can acquire fluorescence data through multiphoton excitation but also can simultaneously collect a bright field image through the use of a transmitted light photodetector. We decided we could use the bright field data to distinguish EB borders and thereby EB size without having to rely on the presence of fluorescence signal. To do this we modified our MPFC data collection software to take advantage of a series of pre-existing ImageJ functions to reliably define the size and spatial location of an EB within the bright field image (**Figure 5.1A**). To begin, the "Find Edges" function was used to highlight the border of the EB in the bright field image, creating an outline of the particle. To ensure that small edge scan effects don't significantly affect the robust measurement of the EB or particle border we used the "Gaussian Blur" function to smooth the highlighted borders in the image. The sigma radius input for the Gaussian blur defines the degree of smoothing. For EBs, we found that a sigma radius of 2.2 was effective for accurate estimation of particle size. A higher sigma radius resulted in a more drastic overestimation of particle size, while a lower sigma radius led to more frequent instances of discontinuities in the border, resulting in inaccurate measurements. From the resulting outline of the particle, the minimum autothreshold feature was employed, creating a mask of all pixels within the particle. This mask was approximately 10% larger than the actual area of the particle (data not shown). To correct for this overestimation an erode function was applied that strips the border pixels of the mask and minimizes error to 4.0% $\pm$ 4.6% of the total area, as determined by manual tracing. This measurement was displayed in a results table generated in real-time as area in pixels, which can be displayed as area in microns based on MPFC system calibration for the chosen optical parameters (i.e. lens magnification, zoom, etc.).

The above described analysis of the bright field data not only allows for effective robust sorting of particles, but can directly assist in the analysis of fluorescence based trends in the corresponding fluorescence intensity image. The MPFC software not only can simultaneously collect the bright field and fluorescence intensity images but can also do co-registered analysis on both so that the bright field based morphology detection can be used to directly help in fluorescence data interpretation. Masking the border of an EB in flow in the bright field image not only allows for a measurement of particle size in real time but also creates a region of interest (ROI) that

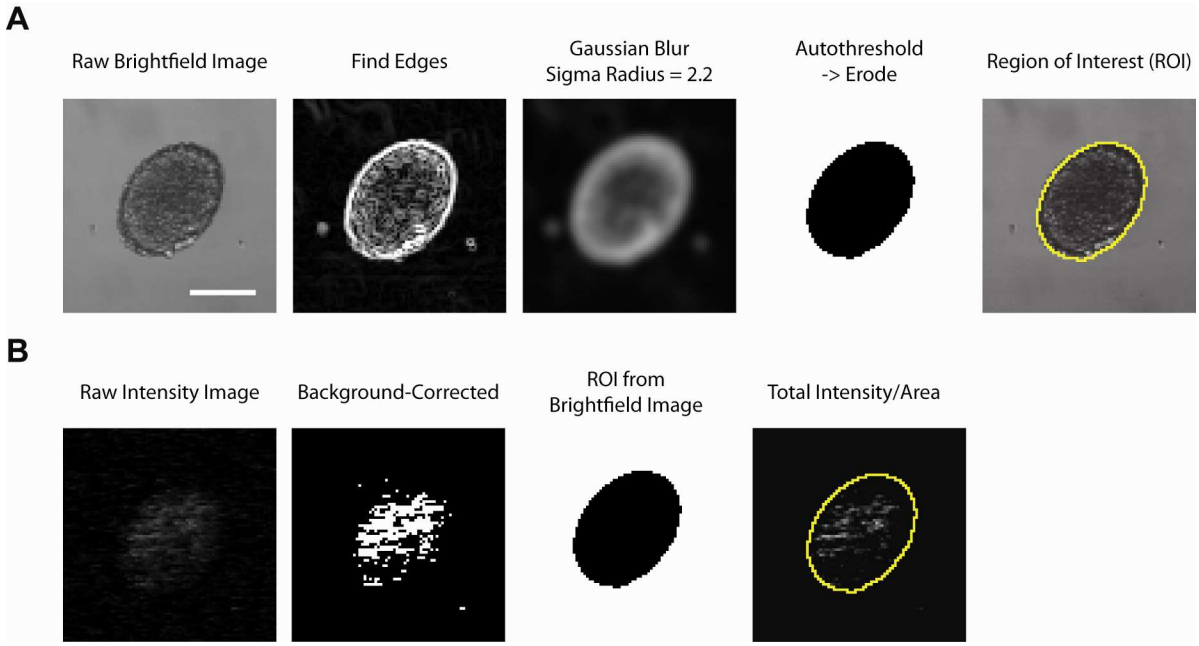

Figure 5.1 Overview of new WiscScan functionalities for the MPFC. A) Images demonstrating the sequence for real-time image segmentation including (from left to right) raw bright field image, "Find Edges", "Gaussian Blur" filter with variable sigma radius (controlled by user), applied autothreshold feature (minimum method) with "Erode" feature, and final region of interest (ROI). B) Images demonstrating the sequence for overlaying the particle ROI onto the intensity image including (from left to right) raw intensity image, background-corrected image, the final ROI acquired from the bright field image, the final intensity image per bright field area, with all pixels excluded that are not contained within the ROI, scale bar = 200 µm.

can be applied to the fluorescence image to confine and sum intensity pixels that are not contiguous, thereby permitting measurement of the fluorescence intensity per unit area. To calculate this fluorescence intensity per unit area (**Figure 5.1B**), the fluorescence intensity image acquired through WiscScan was regressed with a background threshold so that only pixels above background intensity appear on a processed intensity image. Due to additional noise produced by flowing media and cell debris, there may be fluorescent pixels outside of the particle that exceed the background threshold. To exclude these confounding pixels, the ROI created from segmentation of the bright field image was applied to the processed intensity image, resulting in an image displaying only the pixels above background intensity that were inside the particle. Each pixel within the ROI was assigned an intensity value between the background threshold and maximum detectable intensity value (255). The sum of all the pixel intensity values provided a measurement of total intensity, which was then divided by the ROI for a final measure of fluorescence intensity per unit area. Similar to the size measurement, fluorescence intensity can be displayed as both area in pixels or microns.

5.4 Purification of EBs Based on Size

To determine whether the bright field segmentation algorithm coupled to the MPFC could effectively detect and sort EBs based on calculated size, we sorted EBs into three different size ranges (**Figure 5.2A**). To this end, hanging drops were seeded at 200, 400, and 500 cells per drop, to obtain a relatively wide size distribution of EBs. EBs of different cell number were combined into a single population and the size distribution determined in a pre-sort analysis trial (**Figure 5.2B**). Consecutive sorting of a given population of EBs was performed to obtain small, medium and large EB fractions (**Figure 5.2C**). First, a threshold of 330 µm was set, separating EBs greater than 330 µm into the sorting outlet port and allowing EBs less than 330 µm to flow into the main outlet port. EBs collected in the main outlet port were further sorted such that EBs greater than 250 µm (and necessarily less than 330 µm) were diverted to the sorting outlet port. Sorting efficiency was defined as the number of EBs physically collected from the sorting port relative to the number of positive events detected in flow by the software. The enrichment ratio was defined as the ratio of the number of desired EBs to undesired EBs in the sorting output port divided by the same ratio at the sample input port [85]. Sorting efficiency of EBs greater than 330 µm in diameter (large) and of EBs between 250 and 330 µm (medium) was 94.1 $\pm$ 5.6% and 87.9 $\pm$ 19%, respectively while enrichment ratios were 18.0 $\pm$ 15.7 and 25.0 $\pm$ 22.5, respectively (**Figure 5.2D**). Therefore, real-time segmentation

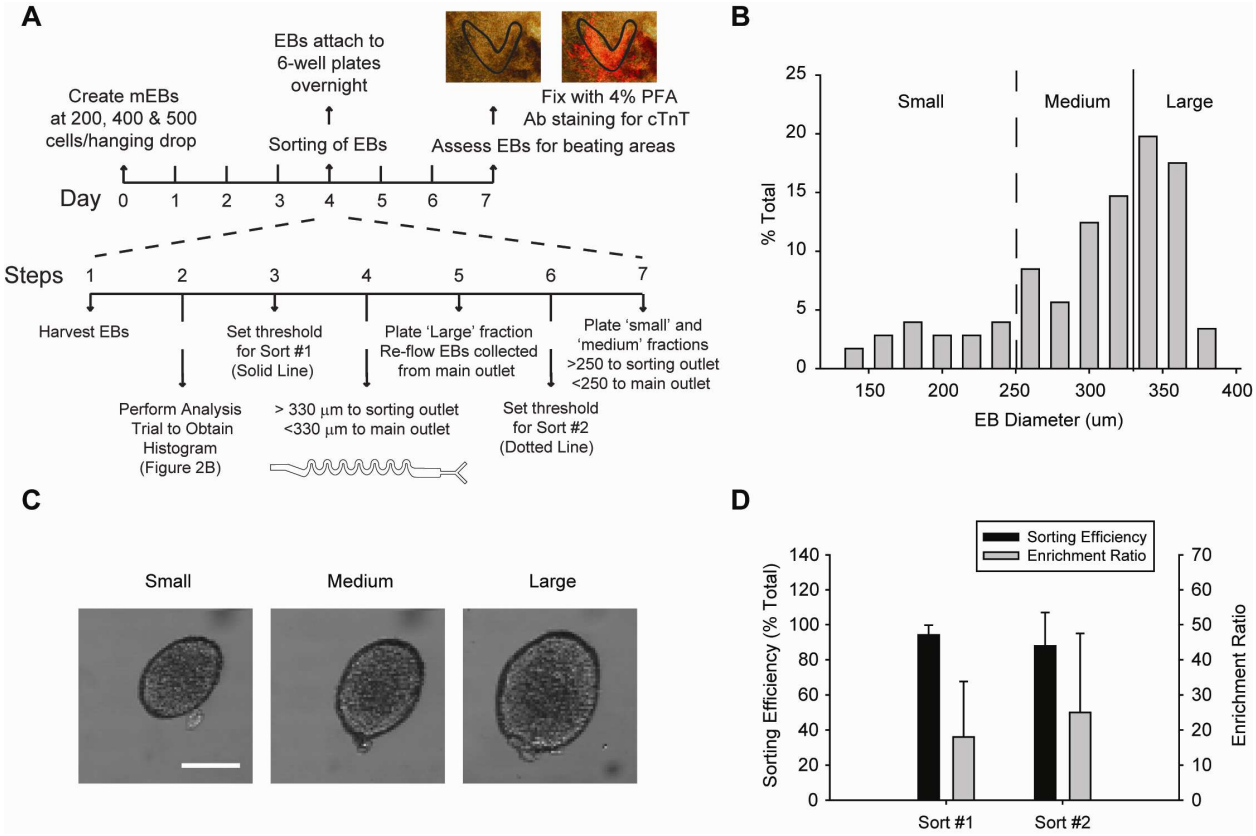

Figure 5.2 Sorting EBs based on area measurement. A) Schematic of experimental protocol. EBs were made in hanging drops with starting concentrations of 200, 400 or 500 cells per 30 µl drop. EBs of all sizes were harvested and mixed together at day 4. EBs greater than 330 µm in diameter were isolated (Large Fraction) first while those less than 330 µm were bypassed and collected in the main outlet port. The population collected in the main outlet port was then sorted by setting a sorting threshold of 250 µm in diameter. Next, the positively sorted fraction consisted of those EBs above 250 µm in diameter (Medium Fraction), while those less than 250 µm were bypassed and collected in the main outlet port (Small Fraction). EBs were maintained separately and plated onto 6-well plates. They were then assessed for beating areas and stained for cTnT on day 7 of differentiation. B) Histogram depicting the size distribution of the EBs to be sorted on the MPFC. Thresholds for positively selecting the large population (solid line) and medium population (dotted line) are displayed. C) Bright field images taken in flow of representative EBs from small, medium and large fractions separated during the consecutive sorting trials, scale bar = 200 µm. D) Sorting efficiencies and enrichment ratios for purifying the large population (n=3 trials, 184 EBs) and the medium population (n=3 trials, 81 EBs). Error bars are standard deviation of trials.

of the bright field image of an EB yields an accurate measure of size as well as subsequent sorting capabilities based on that size determination.

5.5 Sorting EBs Based on NKX-2.5 GFP Reporter Expression Indicative of Cardiac Precursor Cells

To test the ability of the MPFC to purify EBs based on varying levels of non-contiguous fluorescence intensity, we generated EBs from mouse induced pluripotent stem cells (iPSCs) carrying a NKX2-5 Emerald Green Fluorescent Protein (EmGFP) Bacterial Artificial Chromosome (BAC) reporter [100, 102]. EBs matured for 3 days in hanging drops and then were sorted based on EmGFP fluorescence intensity with the MPFC (**Figure 5.3A**). To establish a threshold such that EBs with the greatest EmGFP intensity per unit EB area (i.e., the top 25%) would be positively sorted, a histogram depicting fluorescence intensity per unit area of a test sample population of EBs was generated under analysis flow conditions (**Figure 5.3B**). During sorting flow conditions, EBs below the determined threshold were directed to the main outlet port while those above the threshold were directed to the sorting port (**Figure 5.3C**). After sorting, EBs from both the main and sorting outlet ports were collected and counted before transferring to 6-well plates for long-term culture. Sorting efficiency was defined as the ratio of the number of EBs physically collected from the sorting port, to the number of positive events detected in flow. A sorting efficiency of 89.0 $\pm$ 11.1% and an enrichment ratio of 25.4 $\pm$ 19.3 was achieved (**Figure 5.3D**), which are comparable to previously reported values corresponding to the purification of large fluorescent beads or EBs uniformly stained with CellTracker^{TM} (Molecular Probes/Invitrogen, Carlsbad CA) dye [6].

5.6 EBs Sorted at Early Time points According to Size or NKX2-5 expression Show a Higher Propensity to Develop Mature Cardiomyocytes

EB size can dictate yield of differentiated cardiomyocytes [103-105] demonstrated by studies attempting to control initial EB size with cell culture constraints. Another approach to control size of microtissue populations is to sort them after formation using mechanical barriers to microfluidic channels of prescribed dimension [106]. The primary limitation of these methodologies is the need to adjust physical dimensions of the culture vessels or sorting device to obtain a final population of EBs within specific size ranges tailored to a user-specific application. Here we have shown that the modified MPFC is capable of sorting EBs in the range of 100 - 400 µm with high efficiency.

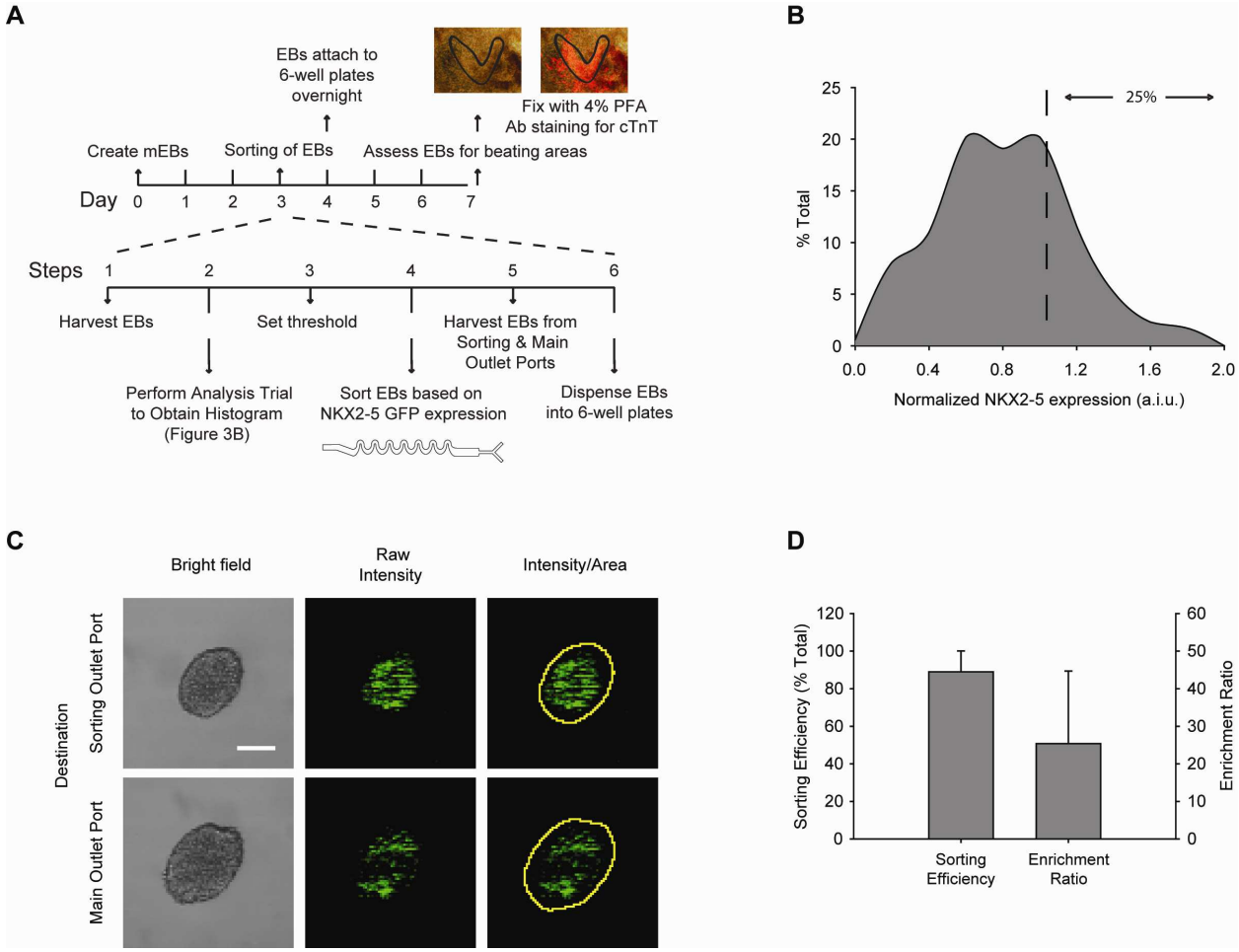

Figure 5.3 Sorting EBs based on NKX2-5 expression with the MPFC. A) Schematic depicting the experimental protocol for sorting trials. EBs were harvested on day 3 of differentiation and subsequently analyzed on the MPFC without sorting to determine the distribution of NKX2-5 expression of the population. Thresholds were set such that EBs exhibiting the top 25% fluorescence intensity per unit area were positively selected and sorted. B) Distribution of normalized NKX2-5 expression for the sample input population of EBs as determined in a pre-sort analysis trial. C) Bright field and intensity images of an EB determined to exceed the user-defined sorting threshold (top row) and an EB less than the sorting threshold value (bottom row). The processed intensity image illustrates the ROI overlaid onto the intensity pixels above background in real-time. The total intensity of all the pixels above background within the ROI was divided by the pixel area of the ROI for a final measurement of fluorescence intensity per unit area, scale bar = 200 µm. D) Sorting efficiency and enrichment ratios determined from sorting trials (n=3 trials, 226 EBs). Error bars are standard deviation of trials.

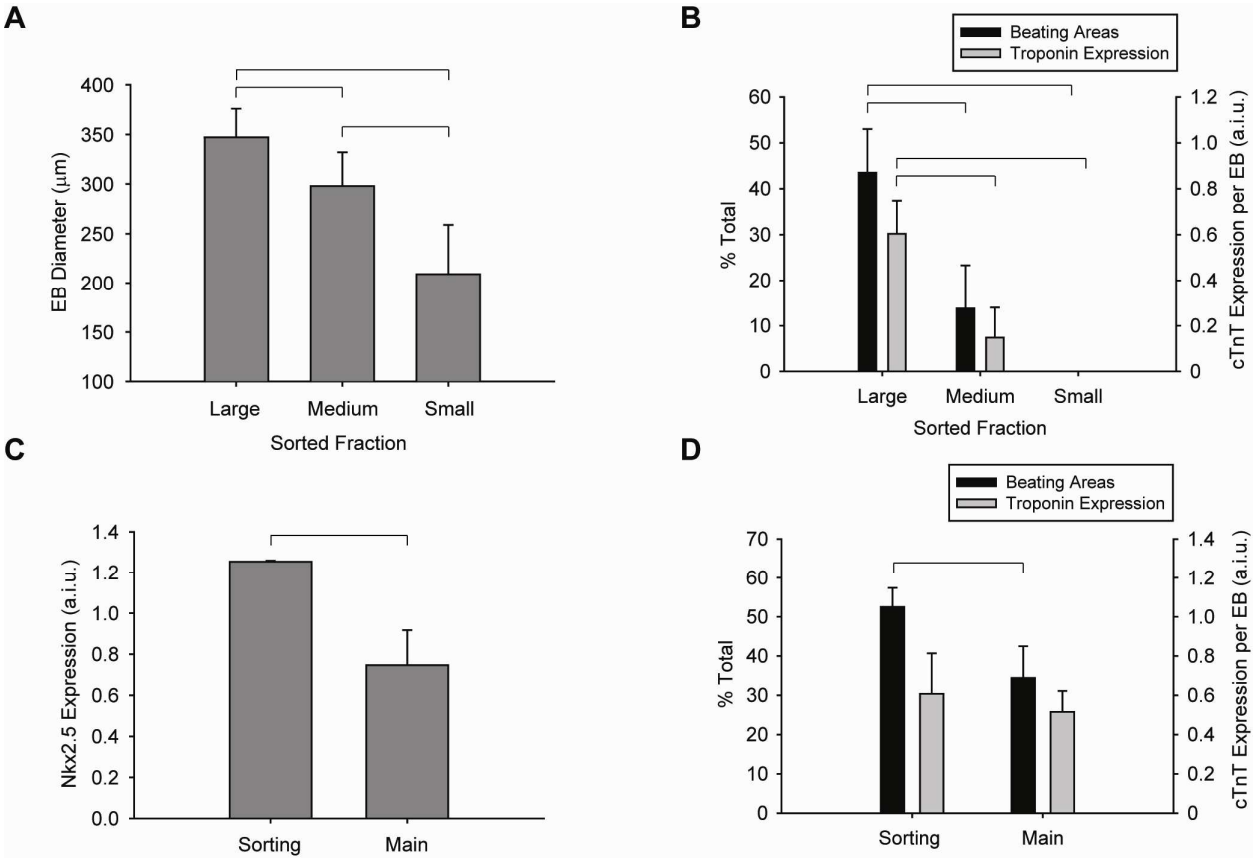

Figure 5.4 Capacity of sorted fractions of EBs to develop cardiomyocytes A) Average size of resulting EBpopulations (small, medium and large) collected after sorting with the MPFC. B) Beating areas and corresponding cTnT expression of populations sorted based on size. C) Average normalized NKX2-5 expression of EBs collected from sorting and main outlet ports, determined by static imaging after sorting. D) Beating areas and corresponding cTnT expression of EB populations sorted based on NKX2-5 expression. Brackets indicating significant differences ($P < 0.05$).

To determine whether the size of EBs sorted in our system impact their ability to produce cardiomyocytes, we isolated three distinct size ranges (small, 250 µm in diameter or less; medium, 250-330 µm; large, 330 µm or more) using the MPFC system (**Figure 5.2**). The mean diameters of the resulting sorted populations were 209 $\pm$ 50 µm, 298 $\pm$ 34 µm, and 347 $\pm$ 29 µm, which all significantly differed from one another ($P < 0.05$) (**Figure 5.4A**). The large size group of EBs produced the most beating areas on day 7 of differentiation (43.5 $\pm$ 9.5%) (**Figure 5.4B**), and significantly exceeded the number of beating areas produced by the medium (13.8 $\pm$ 9.5%; $P < 0.05$) or small fractions (0%, $P < 0.05$). Similar trends were found when quantifying cTnT, a protein marker expressed only in mature cardiomyocytes, with the large EB group (0.60 $\pm$ 0.15) having significantly greater cTnT expression per EB compared to the medium (0.14 $\pm$ .13; $P < 0.05$) and small fractions (0; $P < 0.05$) (**Figure 5.4B**). Thus, larger EBs separated on the MPFC at an early time point in differentiation exhibit enhanced potential for cardiomyocyte differentiation.

We also hypothesized that EBs expressing relatively high levels of the early cardiac transcription factor NKX2-5 at early time points in differentiation would produce significantly higher yields of mature cardiomyocytes at later time points in differentiation. As before, day 3 EBs were introduced into the MPFC and those with the top quartile of GFP fluorescence intensity were sorted. The relative amount of NKX2-5 expression in the sorted population compared to the unsorted populations was 1.25 $\pm$ 0.01 a.i.u. and 0.75 $\pm$ .17 a.i.u., respectively (**Figure 5.4C**) ($P < 0.05$). EBs were plated after sorting and at day 7 after EB generation (4 days after sorting) were assessed for beating areas and cTnT expression. Sorted EBs produced significantly more beating areas compared to the unsorted population of EBs (52.5 $\pm$ 4.9% and 34.4 $\pm$ 8.1% ($P < 0.05$), respectively, **Figure 5.4D**). Sorted EBs had higher expression levels of cTnT compared to the unsorted population (0.59 $\pm$ .19 and .50 $\pm$ .12 a.i.u., respectively), though these values were not significantly different. Thus, sorting EBs with our enhanced MPFC system at an early time point in EB development based on cardiac precursor gene expression can be used to predictively enrich for EBs with a higher propensity to form beating areas indicative of cardiac differentiation.

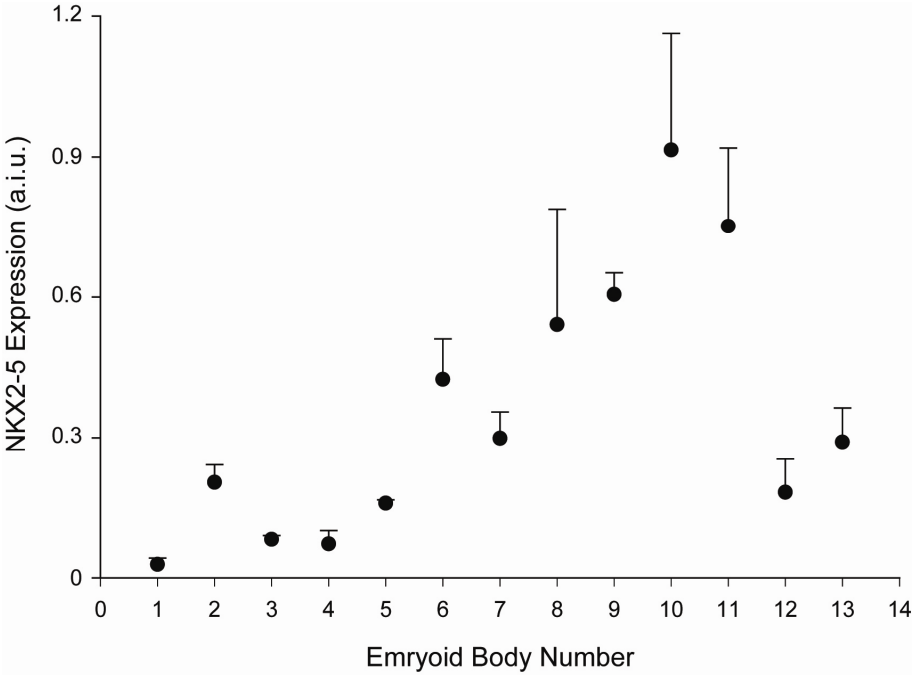

Figure 5.5 Optical sections of day 3 EBs expressing NKX2-5 at random particle rotations. Three different optical sections were imaged 35 µm deep into several different EBs (displayed as single data points). Different optical sections were attained by turning or disrupting the EBs between each image acquisition. The standard deviation of each measurement signifies the variability in measurements of optical sections taken at different positions in the 3D volume.

5.7 Discussion

Here, we take advantage of real-time image processing tools incorporated into the MPFC to sort EBs based on size as well as non-contiguous fluorescence intensity, corresponding to expression of cardiac-related transcription factor, NKX2-5, and preserve sorted populations for long term analysis of differentiated cell function. This is the first reported application of real-time image segmentation to trigger sorting in a microfluidic device for large (>100 µm) cellular particles. Although the images in this study were acquired using a mulitphoton laser scanning microscopy system, the size-sorting approach could be utilized with any imaging modality capable of producing a bright field image of large particles. It can also be utilized with other fluorescence imaging approaches such as confocal microscopy [107] that can simultaneously collect bright field and fluorescence images. Our motivation for developing such an MPFC system was driven by a desire to understand the factors that stimulate cardiomyocyte differentiation. However, the approach could be tailored to study many cell types and associated behaviors in aggregates or microtissues. Thus, we describe an accessible and versatile system that can help transform the way that adherent cell types are studied in the context of three-dimensional microenvironments.

EB size is known to influence the type and amount of differentiated cells present in the EB over time. For example, Mohr et al [98], show that smaller EBs are less likely to form beating cardiomyocytes, but those EBs with contracting areas are more highly enriched in cardiomyocytes than larger counterparts. Similarly, others found that cardiogenesis and neurogenesis were regulated by the size of the concave microwell used to generate EBs [99, 104]. These studies were accomplished by regulating size at the time of EB formation; less well studied are phenotypes emerging when EBs are sorted at points following EB formation. A microfluidic device was recently described [106] which utilized a series of appropriately spaced pillars in a microchannel to alter the fluid flow path to divert and thereby purify EBs with diameter differences of approximately 100 µm, with a maximum size of approximately 300 µm. This device is inexpensive and accessible to many labs but is limited by the physical dimensions of the device such that multiple devices would be needed depending on the cell aggregate size and range of interest. Our MPFC system can handle a large range of EB sizes, the upper limit of which is dictated by the size of the channel. For the device described here, the height is 1000 µm and represents the smallest dimension of the flow cell cross-section. Thus, this device can accommodate EBs of approximately 50 µm up to 500 µm in diameter (approximately half the height of the flow cells [6]). In addition, the MPFC can discriminate differences as low as the error corresponding to real-time size measurement (4.0% $\pm$ 4.6% of the manually measured diameter; e.g. 26 µm for a

300µm particle). We show that differences in EB size at three days after EB formation significantly alter the percentage of beating areas in a given EB population and the corresponding expression of cardiac troponin T. Studies of this type could be used to determine how factors related to size, such as diffusion of soluble molecules (e.g., growth factors or metabolites) and insoluble structural elements, such as extracellular matrix proteins, impact cardiomyocyte differentiation.

Reporter elements coupled to proteins indicative of stem cell differentiation enable identification of soluble and insoluble factors that direct differentiation. The utility of these reporter cell lines is augmented when stem cells and their progeny can be maintained in a 3D or tissue-like arrangement, as that found in an EB or similar microtissue. One could argue, however, that much progress has already been made in understanding factors that direct stem cell differentiation. Indeed, recent progress indicates gene delivery of transcription factors can directly program murine stem cells to a cardiomyocyte fate with high efficiency [100]. By comparison, the MPFC technology described here may not provide a effective means to optimize the yield of cardiomyocytes. It can, however, provide key insights into stem cell microenvironments (i.e. compositions of EBs) that are conducive to differentiation and that maintain a differentiated and functional phenotype. In this way, we can continue to improve extended *in vitro* culture conditions and perhaps better predict and promote outcomes of cell delivery *in vivo*.

The MPFC technology described here has advantages for sorting EBs based on size or reporter elements over previously described systems [19, 106], including our first generation MPFC device [5-6]. Our first generation device was accessible to laboratories with access to microfabrication capabilities and imaging systems with real time data acquisition capabilities. It was unique in that it allowed for sheathless particle focusing with minimal damage to the large particle as a consequence of flow. It could also do sorting of intact EBs based on intrinsic or extrinsic fluorescence signals. The current generation MPFC described here maintains these advantages and adds the ability to analyze non-contiguous fluorescence of an EB in real time and sort based on those fluorescence parameters. The sorting efficiency is comparable to the first generation sorting device, with average efficiency of 85-95%. Future iterations of the MPFC will seek to take advantage of the images acquired of each EB in flow. Because an image is obtained, it will be possible to utilize ImageJ functionality to utilize image processing approaches to sort based on distribution of fluorescence, and so associated protein or molecule, within an EB (or other large particle).

Sorting efficiency of the first generation MPFC as well as the current generation is limited by false positive sorting events, which most often reflect coincidence events when two or more particles are detected in the same

image frame. In our device, coincidence occurs in approximately 7% of events detected by the software (data not shown). Coincidence increases with particle-particle interactions. We attempt to limit particle-particle interactions by separating them with inertial lift forces imposed by the asymmetric curving channels [83] present in the microfluidic device. However, coincidence does still occur and changes as a consequence of differences in particle velocity. Additional factors that may increase the false positive rate may include the unpredictability of the velocity of smaller EBs in microfluidic devices. Velocity variability can also result in false negative events if EBs are diverted outside the interrogation region and therefore never trigger a sorting pulse. We have empirically verified that as particle size decreases the corresponding velocity range broadens. Most of the sorting errors evident in our system could be reduced or alleviated if particle velocity was increased because the increase in velocity would improve particle focusing and separation within the microfluidic device [84]. Currently, we are limited by a relatively low maximum image acquisition speed (~5.5 frames/sec) and corresponding low resolution (128x128) of our optical arrangement and so flow velocities cannot exceed approximately 2 mm/s. To this end, we are investigating line scanning and other high-speed software and hardware scanning approaches to improve imaging acquisition rates and thereby improve both throughput and sorting efficiency.

Another consideration when analyzing spatially segregated fluorescence intensity within a microtissue on the MPFC, is the variability corresponding to each detected optical section. As a microtissue traverses the interrogation region, multiple planes will be measured based on the rotational position of the EB at the instant of an image scan. To determine the approximate variability of NKX2-5 GFP expression in our EBs, we obtained images of optical sections at random 3D orientations of single EBs in static mode, in an attempt to simulate the various possible optical planes detected in flow. We found that the coefficient of variation for a measurement of NKX2-5 fluorescence of a single EB is approximately 25 $\pm$ 13% (n=13). As expression levels of NKX2-5 increase, there is more variability in the measurement (**Figure 5.5**), which is not surprising considering "pockets" of differentiating cells are typically present in EBs, and not uniformly distributed throughout the volume. Here, the impact of sorting based on one z-plane measurement did not drastically affect the outcome of this specific population of EBs and associated reporter element, but could have a greater affect on other cell types and associated reporter elements if expression of the reporter is localized to one side of the EB, or expressed as a gradient from one side to another. Future MPFC software improvement will include the ability to average measurements from multiple z-planes of an EB or other large particle. At current flow rates EBs are most commonly detected in three consecutive frames as

they traverse the interrogation region. Averaging intensity measurements from these three frames would provide a more representative quantification of the total fluorescence intensity throughout the volume of the large particle.

Our results demonstrate that MPFC technology can be used to effectively sort EBs based on fluorescence of cells within the EB, even if fluorescent cells are separated from one another. The technology can help advance our understanding of the factors that impact on behavior of cells within the EB which should translate to a better understanding of what happens to differentiated or differentiating stem cells after transplantation to a tissue bed or with extended culture ex vivo. In addition, the MPFC could be used to augment the study of stem cell behavior in other engineered 3D constructs or the behavior of other cell types in aggregate or microtissue formats by increasing throughput and utilizing unique features of multiphoton excitation microscopy to probe endogenous fluorescent structures including collagen and autofluorescent metabolites.

CHAPTER 6

Noninvasive detection of cell death with Multiphoton Laser Scanning Microscopy (MPLSM)

6.1 Specific Objective 3: To use the MPFC system to non-invasively purify populations of stem cell aggregates and to assess the functional capacity of sorted populations. Hypothesis: Purified populations of EBs, detected and sorted on the MPFC based on fluorescent indicators of size, cell phenotype and viability, will have higher percentages of cells adopting a cardiac phenotype (Chapters 5 & 6) than unsorted populations of EBs (thereby addressing criterion C).

Continued advances in stem cell biology and stem cell transplantation rely on noninvasive biomarkers to characterize cells and stem cell aggregates. The noninvasive quality of such biomarkers is essential, since exogenous labels, probes or reporters can unintentionally and dramatically alter stem cell state as can disruption of cell-cell and cell-matrix interactions. Here the autofluorescent metabolite, nicotinamide adenine dinucleotide (NADH) is investigated as a noninvasive, intrinsic biomarker of cell death when detected with multiphoton optical-based approaches.

NADH plays a key role as a carrier of electrons and is involved in many important metabolic pathways, such as glycolysis [108]. NADH has two forms in cells: free and protein bound. Most bound NADH is found in the mitochondria while free NADH exists in both the cytoplasm and the mitochondria [109-111]. NADH fluorescence intensity changes have been used to study cell metabolic activity *in vivo* for many years [112-117]. As well, recent studies have used MPLSM to characterize NADH and the intrinsic metabolite flavin adenine dinucleotide (FAD) in cancer cells and characterize the metastatic potential [71, 74, 118]. These studies and others [73, 77-78] have helped define the experimental conditions for our MPFC trials to examine NADH. For example, the metabolic state of carcinoma cells, as detected by endogenous fluorescent metabolic intermediates, has been correlated with the identification and metastatic potential of cancers, in both animal and human models [118].

Cell death is essential for the development, homeostasis and repair of tissues (reviewed in [119-120]). Recent studies suggest cell death is equally important for pluripotent stem cells and “quasi-developmental” events that occur with differentiation [121-126]. For example, inhibition of prostate apoptosis response-4 (PAR-4) in pluripotent stem cells limits differentiation of cells of endoderm, mesoderm and ectoderm lineages [127]. However, greatly limiting the study of the significance of stem cell death has been the inability to distinguish dead from viable

cells without application of exogenous labels that might alter stem cell state. Thus methods for noninvasive detection of cell death are necessary. Furthermore, stem cells are maintained and differentiate most efficiently in stem cell aggregates and so it is crucial to assess cell death without disrupting the aggregate [128].

The intensities of autofluorescent metabolites have been used as biomarkers of cell viability in yeast [129], primary epithelial cells [130] and kidney tissue [131]. Moreover, fluorescence lifetime of intrinsic fluorophores has been utilized as an indicator of cell death [132-133] and as a means for distinguishing between modes of cell death [134-135] (Reviewed in [136]). Of particular interest is the metabolite nicotinamide adenine dinucleotide (NADH), a critical coenzyme in cell energy metabolism. NADH is a primary electron transporter, especially in oxidative phosphorylation through which significant ATP is produced [137]. Given this role, the concentration of NADH in the cell cytoplasm (including mitochondria) would likely decrease with oxidative injury. Flow cytometry, spectroscopy and fluorescence imaging-based studies indicate that NADH levels do decrease with reversible hypoxic injury (i.e., when oxygen is restored, the cells recover native function) [129-131]. However, with irreversible injury, there is actually a sharp, transient increase, followed by a variable decrease in NADH levels [129]. Compelling fluorescence image data suggests increases in NADH correspond to a subpopulation of mitochondria which occupy the perinuclear space [130]. These mitochondria are thought to mobilize in response to apoptotic stimuli and may provide the energy or other as yet undefined functions needed to complete apoptosis. This direct correlation between cell death and changes in NADH levels, which can be assessed though changes in endogenous fluorescence of living cells, suggest that this endogenous fluorescence could be utilized as a non-invasive tool for monitoring viability of individual cells and aggregates, including the viability of stem cells.

Just as therapeutic application of stem cell aggregates would benefit from a non-invasive means to analyze viability, so might other cell aggregates or microtissues such as pancreatic islets. Type I Diabetes Mellitus (TIDM) is an autoimmune disease resulting in the destruction of insulin producing beta cells within the pancreatic islets of Langerhans. Currently, islet transplantation is an emerging clinical therapy with the potential to completely restore beta cell function in TIDM patients [138-139]. The efficacy of therapeutic procedures involving re-implantation of islets into diabetic patients depends primarily on the ability of islets to engraft and survive in the body and secondarily to produce insulin in response to elevated blood glucose levels [140]. A current limitation of the procedure is the need to pick healthy islets of a specific size (150 μm in diameter) from the explanted population. This procedure is time consuming and subject to inter- and intra- reader variability [23]. The number of healthy

explanted islets is variable due the removal of the microtissues from their native vasculature, thereby depriving those cells in the aggregate that are past the diffusion barrier of oxygen and essential nutrients [141]. Survival and function of transplanted islets require that the initial population are relatively healthy and void of copious amount of dead cells. Isolation of this healthy population is currently performed manually, and would greatly benefit from a technology that could perform the same task, non-invasively, in an enhanced throughput fashion.

Therefore, the goal of this study was first to determine whether changes in intensity of NADH fluorescence correlate with cell death in stem cell aggregates and second to determine the physiological impact of early-stage death of stem cells on long-term function of stem cell progeny. Next, we sought to validate the ability of our prototype MPFC system to non-invasively purify populations of EBs based on viability via detection of NADH at early time points in differentiation. Finally, as a more immediately clinically relevant application for the MPFC, we performed static experiments in an attempt to correlate NADH fluorescence intensity to functional islet secretion, and conducted initial sorting experiments on pancreatic islets based on NADH fluorescence.

6.2 Materials and Methods

6.2.1 Stem Cell Culture

HM1 mouse embryonic stem cells were cultured as previously described [5]. ESCs were harvested and resuspended in DMEM + 10% FBS (no LIF or BMP-4) at 1.6 x 10^4 cells/ml. This cell suspension was used to make 30 µl hanging drops over 1X PBS in 100 mm Petri dishes. EBs were harvested 3 days after formation (day 3); this stage served as the time point for initiation of all studies described here.

6.2.2 Drug Treatment and Exogenous Viability Staining of EBs

For induction of cell death, staurosporine (Sigma Aldrich, St. Louis, MO) was applied to EB populations at concentrations ranging from 100 – 500 nM for 2 hours. EBs were stained with LIVE/DEAD® Fixable Dead Cell Stain Kit (L23101, excitation, 495; emission, 520; Invitrogen) at a 1:1000 dilution in 1X PBS for 10 minutes at room temperature on a rocking platform. EBs were rinsed once with 1X PBS and resuspended in DMEM + 10% FBS. This probe penetrates dead or dying cells and binds to intracellular amines throughout the cell volume. The probe also binds extracellular amines of live cells, but is restricted to the cell border and so generates a signal approximately 100-fold lower than that of dead cells (Manufacturer's specifications, Invitrogen). After staining,

individual EBs were plated on 0.1% gelatin-coated 9 x 2 microslides (ibidi, Martinsried, Germany) for imaging and for subsequent tracking for beating cardiomyocytes.

6.2.3 Isolation of Mouse Pancreatic Islets and Islet Cell Culture

Intact pancreatic islets were isolated from mice using a collagenase digestion procedure as previously described [142-143]. Briefly, the pancreas was perfused with a 0.5 mg/ml collagenase type XI (Sigma Aldrich, St. Louis, MO) solution in Hanks Balanced Salt Solution (HBSS, Life Technologies, Carlsbad, CA) with 0.02% radioimmunoassay grade BSA. The disaggregated tissue suspension was first subjected to a 1000 µm polyethylene mesh (Spectrum Laboratories, Rancho Dominguez, CA) to remove large debris and secondly to a Ficoll gradient (Sigma Aldrich), to separate islets from surrounding acinar tissue. Islets were handpicked under stereomicroscopic observation and subsequently cultured overnight (16-18 Hours) in RPMI 1640 containing 11.1mM glucose and supplemented with 10% heat inactivated FBS and 1% Pen/Strep. The islets were placed into a 60mm Petri dish (non Tissue Culture treated) containing 5mL of fresh RPMI 1640 supplemented media. From 60mm Petri dishes, single mouse pancreatic islets were placed into individual 9x2 ibidi microwells for imaging of NADH fluorescence intensity on the MPLSM. Following image collection, islets were labeled and carefully placed into a 96 well plate, grouping islets with similar NADH fluorescence intensity for subsequent insulin assay analysis.

6.2.4 MPLSM Imaging

EBs and pancreatic islets were imaged using MPLSM with optical configuration similar to that previously reported [5]. To view the live/dead probe, the Ti:Sapphire laser was tuned to 890 nm with a 520/35 nm emission filter. To view NADH intensity, the Ti:Sapphire laser was tuned to 780 nm excitation with a 457/50 nm bandpass emission filter. Average power measurements were taken at the sample, and determined to be 21 mW and 37 mW, for 890 nm and 780 nm excitation conditions, respectively, which is within a reported range supportive of cell viability [144]. Images were taken with a Plan Apo VC 20X air, 0.75 NA, 1.0 mm WD objective (Nikon, Melville, NY) at a resolution of 512 x 512 with a one second exposure time for EBs, and a 10X air, 0.75 NA 1.2 mm WD objective (Nikon) for pancreatic islets. Power and gain settings were set such that less than 5% of pixels were saturated and background noise was kept to a minimum. Bright field and intensity images were collected using in-house developed software (WiscScan). Fluorescence and size measurements of EBs and pancreatic islets were

made using ImageJ software [101]. For analysis, background levels were identified such that less than 10% of pixels on a background image (i.e., containing no islets or EBs) were saturated for all conditions. Background fluorescence intensity levels were subtracted from each pixel of the EB or islet image (BC, background-corrected). For live/dead extrinsic staining of EBs, a region of interest (ROI) was created to match the border of EB cross-section of the background-corrected intensity image. The percentage of viable cells of an EB was determined by first identifying the fluorescence intensity level of a living cell. The fluorescence intensity level of living cells was then subtracted (LCC, live cell-corrected) from each pixel of the ROI defined above. The percentage of viable cells of the EB was defined as the fraction of pixels without intensity after LCC divided by the total number of pixels per ROI. The percentage of dead cells of the EB was defined as the fraction of pixels with intensity after LCC divided by the total number of pixels per ROI. The mean intensity per pixel was defined as the total intensity of the ROI divided by the total number of pixels in the ROI.

6.2.5 Spectrofluorometry

A Fluorolog-3 Spectrofluorometer (Horiba Scientific, Kyoto, Japan) was utilized to determine the fluorescence emission spectrum of unmanipulated mESCs. The excitation wavelength was set at 350 nm, corresponding to the excitation peak of NADH, while intensity measurements were recorded within a range of 400-600 nm, corresponding to the emission spectrum of NADH. HM1 mESCs were harvested and resuspended in 1X PBS before measurement. β-NADH (Sigma-Aldrich, St. Louis, Missouri) was reconstituted in 1X PBS at a concentration of 7 mM.

6.2.6 Sorting of EBs Based on NADH fluorescence Intensity on the MPFC

EBs harvested at day 3 of differentiation were either treated (500nM) or not treated with staurosporine as previously described [7]. Similar to static experiments, the Ti:Sapphire laser was tuned to 780 nm, and a 457/50 nm emission filter was used to exclude confounding autofluorescence. Treated and untreated populations were analyzed separately on the MPFC before the sorting trials to determine their respective distribution of NADH fluorescence intensities. The real-time fluorescence intensity calculation described in chapter 5 was used to make the measurement in this experiment, as NADH expression is non-contiguous and must be assigned to an ROI. Next, a, sorting threshold was set such that 95% or more of the treated population would be positively selected in the sorting

trials. In this way, EBs with high NADH intensity were positively selected and diverted into the sorting outlet port while those with relatively low NADH intensity flowed directly to the main outlet port. After sorting, EBs from each outlet port were collected and counted to determine sorting efficiency and enrichment ratio. Finally, EBs were plated onto gelatin coated polystyrene dishes for long-term culture and assessment of beating areas.

6.2.7 Assessment for Cardiomyocyte Function and Immunofluorescence Staining

EBs from static or sorting experiments were placed in an incubator overnight and analyzed for attachment on the following day (day 4). Each subsequent day, medium was replenished in the microwell slides or 6-well plates and each EB was scored for formation of beating areas. On day 12 of differentiation, EBs were fixed with 4% paraformaldehyde and stained for cardiac troponin (cTnT). The National Stem Cell Bank protocol (www.wicell.org, SOP-CH-210C) for immunolabeling of cardiac markers in EBs was utilized for this assessment. Mouse anti-troponin T (cardiac isoform Ab-1, cTnT, clone 13-11, Fisher Scientific, Pittsburg, PA) primary antibody and goat anti-mouse Alexa Fluor 568 (Molecular Probes/Invitrogen) secondary antibody were used. Fluorescence images were acquired using a Zeiss Axiovert 40CFL inverted microscope with a 4X objective, excitation filter 560/55 nm and emission filter 645/75.

6.2.8 Sorting of Pancreatic Islets Based on NADH fluorescence Intensity on the MPFC

Islets were harvested from mice and cultured as described above. Similar to static experiments, the Ti:Sapphire laser was tuned to an excitation wavelength of 780nm, and a 457/50 nm emission filter was used to exclude confounding autofluroescence. One population of islets was analyzed, without sorting, to determine the size and fluorescence intensity distribution for a representative fraction. For each sorting trial, approximately 100 islets were loaded into the sample reservoir in 7 ml of culture media. From the histogram depicting NADH fluorescence intensity, a threshold was set such that the islets with the highest NADH expression (i.e. top 25%) would be positively sorted. In this way, islets with high NADH intensity were positively selected and diverted into the sorting outlet port, while those with relatively low NADH intensity flow directly to the main outlet port. After sorting, islets from each outlet port were collected and counted to determine sorting efficiency and enrichment ratio.

6.2.9 Assessment of Insulin Secretion from Pancreatic Islets

Islets were placed in groups of 4 based on similarity of NADH fluorescence intensity and placed into mesh baskets made from 12 x 75 mm borosilicate tubes (mesh tubes). The mesh tubes were then transferred to a 16 x 100 mm tube containing 1.0ml Kreb's ringer bicarbonate buffer containing 1.7mM glucose, and 0.5% radioimmunoassay grade BSA at 37C for 45 minutes (pre-incubation period). Islets were then incubated for an additional 45 minutes in new Kreb's ringer bicarbonate buffer containing 1.7mM (low) glucose (incubation period). Mesh tubes were then transferred to a fresh 16X100mm tube containing 1.0ml of the Kreb's ringer bicarbonate buffer containing 16.7mM (high) glucose at 37C for 45 minutes. The basal insulin response was determined by the insulin release of islets exposed to 1.7mM glucose during the 45 minute incubation period, while the stimulated insulin response was determined by the insulin release of islets exposed to 16.7mM glucose. Insulin release was expressed as a "fold stimulation" determined by the ratio of insulin secreted at high glucose versus low glucose levels.

Insulin secretion ELISA assays were performed as previously described [142-143]. Briefly, the ELISA plate was coated with monoclonal capture antibody (Fitzgerald, Acton, MA) and washed with 4% BSA solution to prevent non-specific binding of the insulin antibody. Next, standards and aliquots of culture media from islet incubations were added to the 96 well plates for 1 hour, to bind to the monoclonal capture antibody. Next, the biotinylated anti-insulin detecting antibody (Fitzgerald, Acton, MA) was added to the plates, followed by streptavidin conjugated to horseradish peroxidase. Absorbance measurements were taken on a plate reader (Tecan, Männedorf, Switzerland), and analyzed with Magellan software to generate the standard curve and calculate sample concentrations.

6.2.10 Statistical Analysis

For comparison of intrinsic (NADH) and extrinsic (Live/Dead Probe) fluorescence intensity levels of cell aggregates at early and late time points, a normal distribution was assumed and one-way analyses of variance (ANOVA) and Student *t*-test for paired samples were used. For comparison of the percentage of beating areas between sorted and unsorted populations, time of beating area formation, and relative cTnT expression in sorted populations, Student *t*-Test for unpaired samples were used. Data were reported as average $\pm$ standard deviation and were analyzed with JMP 5.0.1 for Windows (SAS Institute, Inc., Carey, NC). Pearson correlation coefficient (r) and confidence interval (*P*) were used to determine whether linear correlations existed between paired values

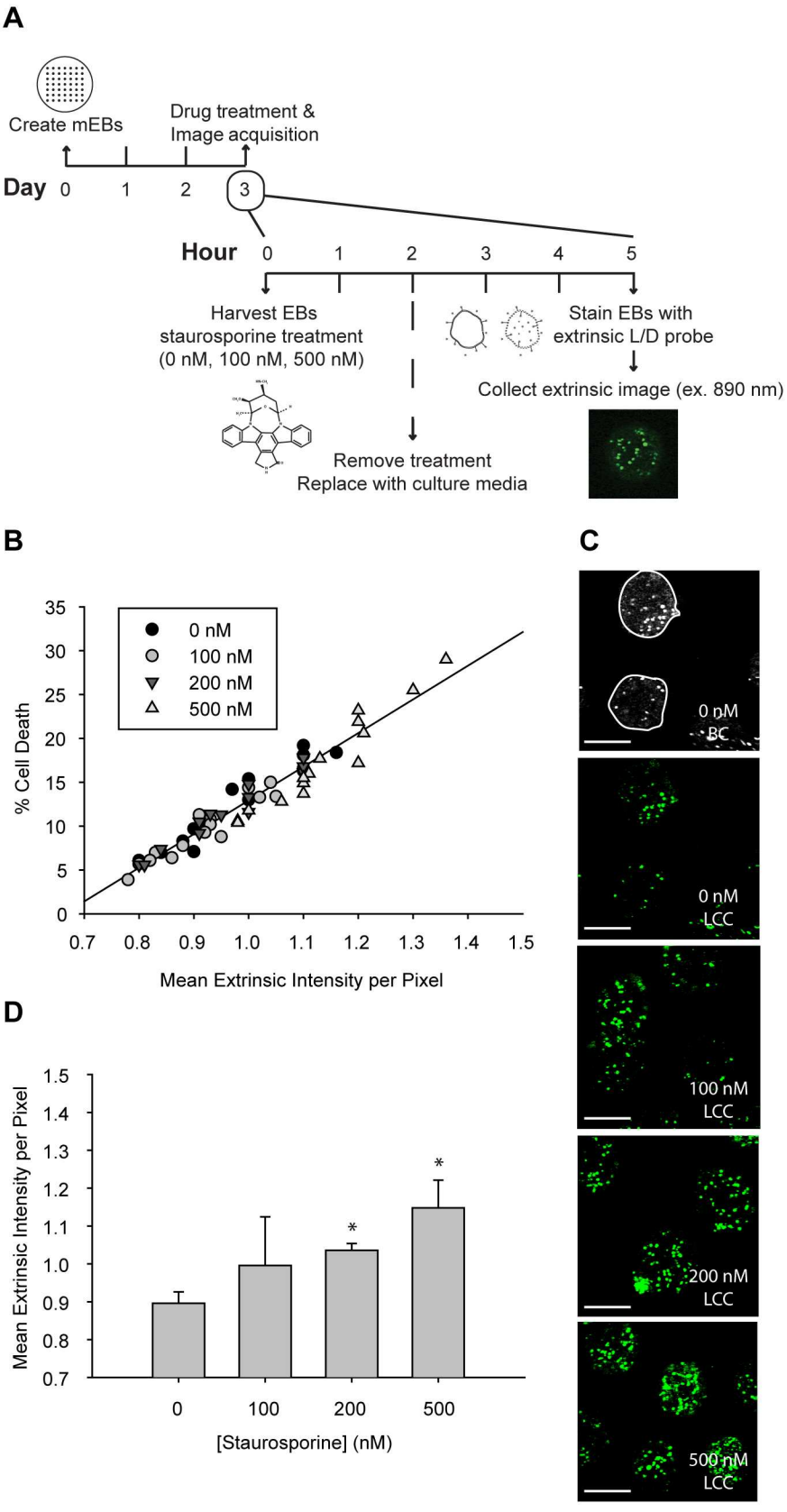
A
Create mEBs
Drug treatment &
Image acquisition
Day 0 1 2 3
Hour 0 1 2 3 4 5
Harvest EBs
staurosporine treatment
(0 nM, 100 nM, 500 nM)
Stain EBs with
extrinsic L/D probe
Collect extrinsic image (ex. 890 nm)
Remove treatment
Replace with culture media
B
% Cell Death
Mean Extrinsic Intensity per Pixel
0 nM
100 nM
200 nM
500 nM
C
0 nM
BC
0 nM
LCC
100 nM
LCC
200 nM
LCC
500 nM
LCC
D
Mean Extrinsic Intensity per Pixel
[Staurosporine] (nM)

Figure 6.1 Induction of cell death via staurosporine. A) Schematic depicting the experimental approach used to determine whether cell death could be reliably induced with staurosporine. EBs were generated from HM1 embryonic stem cells and treated with staurosporine 3 days after EB formation. Following treatment, EBs were imaged at a single time point to detect extrinsic fluorescence of the live/dead probe from a single optical section using MPLSM. B) A strong positive correlation existed between the percentage of dead cells of the EB and the mean intensity per pixel ($r = 0.87$; $P < 0.0001$). Each dot represents a single EB. The percentage of dead cells of the EB and the mean intensity per pixel were determined as described in the materials and methods section. C) Representative images of live/dead staining of EBs with and without staurosporine treatments. BC, background correction, indicates background fluorescence levels have been subtracted from the image. White lines indicate the outline of an EB. LCC, live cell correction, indicates fluorescence associated with living cells has been subtracted from the image. Scale bar = 200 µm. D) Mean intensity of the live/dead probe increased with increasing concentrations of staurosporine. $^{*}P < 0.05$ when compared to the intensity of EBs without staurosporine treatment.

corresponding to 1) the percentage of viable cells in an EB and mean extrinsic fluorescence intensity (live/dead probe) per pixel and 2) mean intrinsic (NADH) fluorescence intensity and mean extrinsic (live/dead probe) fluorescence intensity. A 95% confidence ($P < 0.05$) interval was applied for statistical significance.

6.3 Induction of Cell Death in EBs via ATP-competitive Kinase Inhibition

To assess the relationship between cell death and increased live/dead probe intensity we controllably increased the degree of cell death of murine ESC-derived EBs by treating with graded concentrations of staurosporine, ranging from 0 nM to 500 nM. Staurosporine is an alkaloid compound produced by *Streptomyces staurosporeus* that acts as an ATP-competitive kinase inhibitor, thus promoting caspase 3 expression and inducing apoptosis in a variety of cell types [145]. It should be noted that although staurosporine is a potent inducer of apoptosis, it is very likely that other types of cell death, such as necrosis and autophagy, which also occur within the cell aggregates with and without staurosporine treatment. Here, EBs were treated with staurosporine 3 days after EB formation. Following treatment, EBs were imaged at a single time point to detect extrinsic fluorescence of the live/dead probe from a single optical section using MPLSM (**Figure 6.1A**). A strong correlation existed between the percentage of dead and dying cells of the EB and the mean intensity per pixel ($r = 0.87$; $P < 0.0001$), that is, the intensity of the probe (mean intensity per pixel) increased as the percentage of dead cells increased (**Figure 6.1B**, **C**). Therefore subsequent comparisons between groups were based on mean intensity per pixel for each EB as a measure of cell death. Next, to determine whether cell death within an EB could be predictably altered with staurosporine treatment, the dose response was determined by measuring the mean intensity per pixel of the live/dead probe in EBs either without treatment or with 100 nM, 200 nM and 500 nM staurosporine exposure. Mean intensity per pixel increased with increasing staurosporine exposure, indicating that staurosporine can be used to reproducibly induce cell death in EBs (**Figure 6.1D**).

6.4 NADH Fluorescence Intensity Increases with Increased Cell Death in EBs

Using staurosporine treatment to induce cell death, we tested whether levels of intracellular NADH endogenous intensity were indicative of cell death in EBs, using a well-established, extrinsic, live/dead probe as the gold standard to assess cell death. Others have shown that NADH autofluorescence increases dramatically in the first few hours after induced cell death and subsequently drops below baseline levels [129]. We found the same to be

true for cells of EBs and, specifically, that NADH intensity peaked approximately three hours following staurosporine treatment (**Figure 6.2**). Thus, in order to monitor changes at or near the peak levels of NADH intensity, EBs were imaged at three hours following staurosporine (0 nM, 100 nM and 500 nM) treatment to induce cell death. Just prior to imaging, the extrinsic live/dead probe was applied and then EBs were placed into individual wells of gelatin-coated, multiwell microscopy slides. Each EB was imaged on the MPLSM at 890 nm with a 520/35 bandpass filter for the live/dead probe and next imaged at 780 nm with a 457/50 bandpass filter for NADH expression at the same optical plane (**Figure 6.3**). Independent spectrofluorometric analysis indicated NADH is the principal contributor to fluorescence emission under these conditions (**Figure 6.4**) [71, 146]. Although flavin adenine dinucleotide and lipoamide dehydrogenase could be excited at 780 nm [147] and contribute to the intrinsic intensity of the EBs, the 457/50 emission filter used in these studies helps ensure the contribution is overwhelmingly from NADH and again matches known spectral profiles for NADH. In addition, extensive testing of control cultures revealed no overlap of fluorescence intensity between fluorophores (**Figure 6.5**). Mean intensity per pixel was determined for both NADH (intrinsic intensity) and live/dead probe (extrinsic intensity) and plotted relative to each other (**Figure 6.3B**). To determine statistical dependence of NADH expression on the presence of dead cells (as defined by the live/dead extrinsic probe), a Pearson's correlation coefficient was calculated and found to be statistically significant ($r = 0.69$; $P < 0.0001$). This trend was maintained when individual treatment groups were considered separately. Thus NADH intensity reflected cell death similar to the live/dead probe and therefore could be used as a noninvasive biomarker of cell death in EBs.

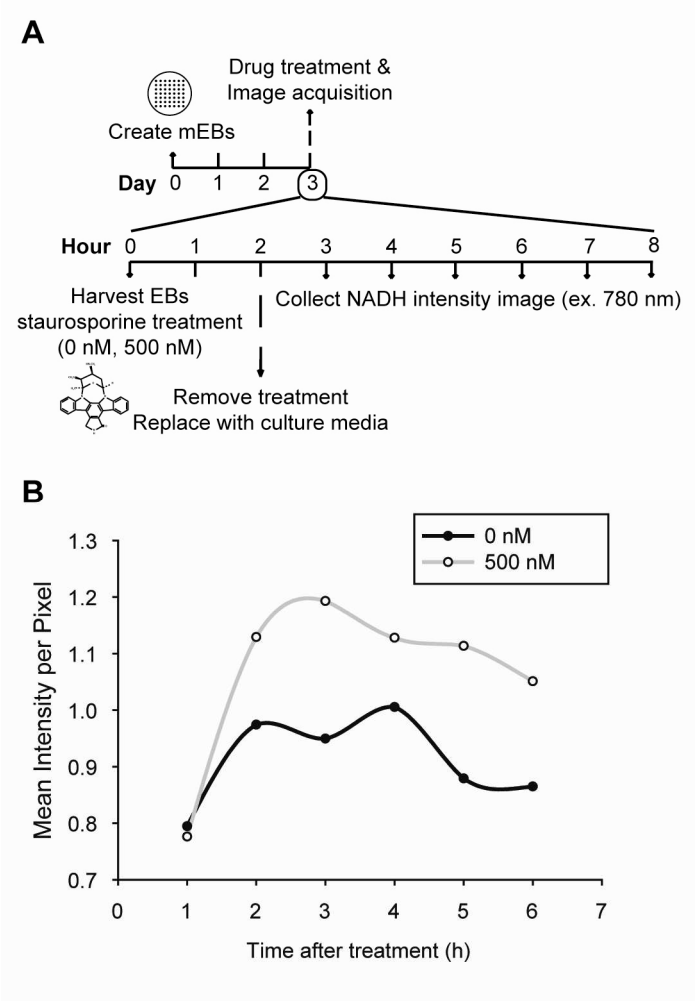

Figure 6.2 Kinetic profile of intrinsic fluorescence intensity of NADH following exposure to 500 nM staurosporine. A) Schematic depicting the experimental approach for determining the kinetics of NADH fluorescence intensity after staurosporine treatment. EBs were treated with staurosporine 3 days after EB formation. Following treatment, EBs were imaged for NADH once per hour for 6 hours. B) Maximum levels of NADH intensity were observed ~3 hours after treatment. When compared to the initial measurement at 1h following staurosporine treatment, the control condition showed a maximum increase in NADH expression of 27%, while the staurosporine treated condition exhibited a maximum increase of 54%. The increase in NADH intensity in the control population likely reflects repeated exposure to the laser, and/or repeated changes in environmental conditions with imaging (e.g. CO_2, temperature).

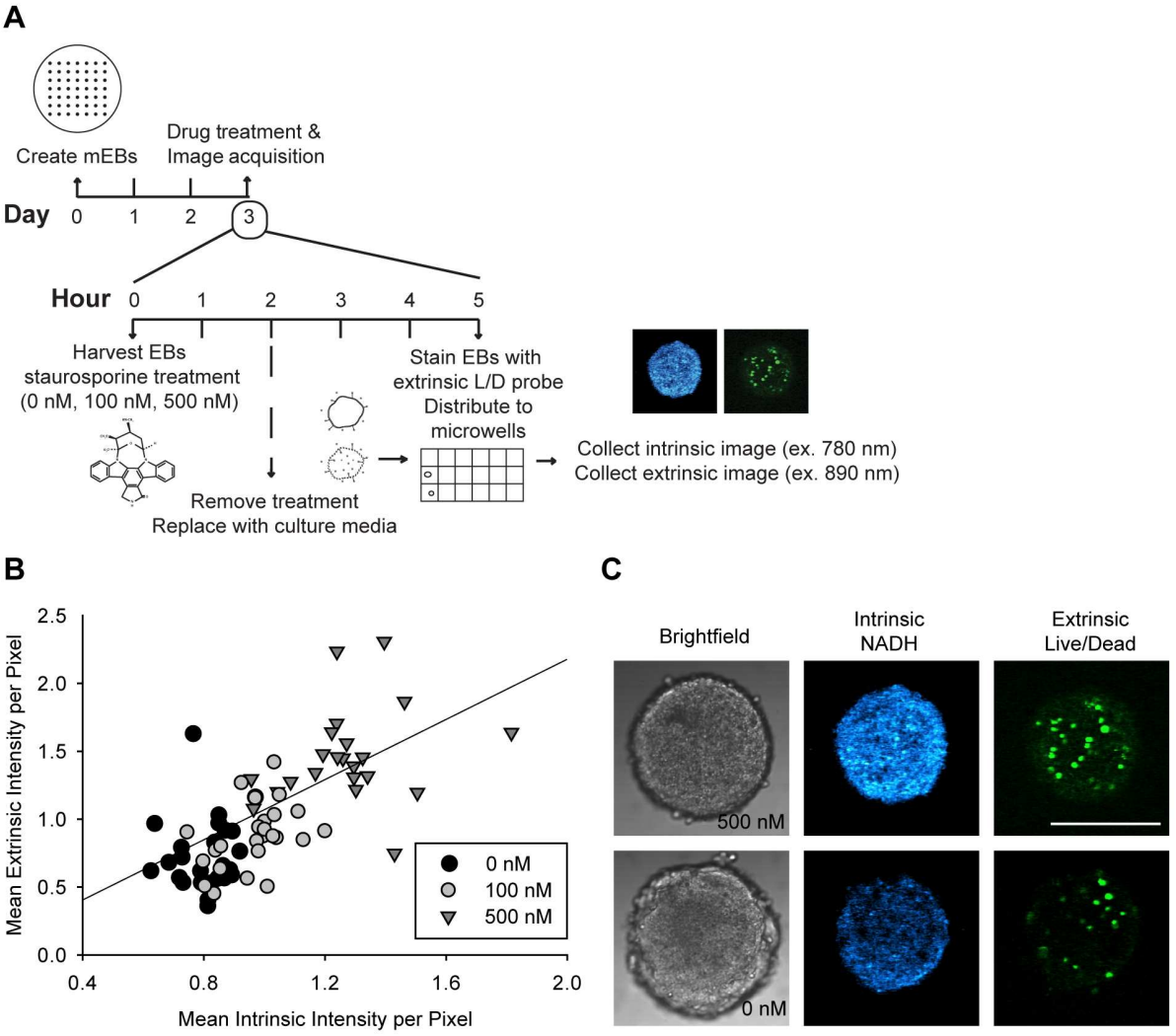
A
Create mEBs
Drug treatment &
Image acquisition
Day 0 1 2 3
Hour 0 1 2 3 4 5
Harvest EBs
staurosporine treatment
(0 nM, 100 nM, 500 nM)
Stain EBs with
extrinsic L/D probe
Distribute to
microwells
Remove treatment
Replace with culture media
Collect intrinsic image (ex. 780 nm)
Collect extrinsic image (ex. 890 nm)
B
Mean Extrinsic Intensity per Pixel
Mean Intrinsic Intensity per Pixel
0 nM
100 nM
500 nM
C
Brightfield
Intrinsic
NADH
Extrinsic
Live/Dead
500 nM
0 nM

Figure 6.3 Relationship between extrinsic fluorescence intensity of a live/dead probe and intrinsic fluorescence intensity of NADH. A) Schematic depicting the experimental approach designed to determine whether NADH intensity correlates with cell death. EBs were generated and treated with staurosporine 3 days after EB formation. Just prior to imaging, the extrinsic live/dead probe was applied and then EBs were placed into individual wells of gelatin-coated, multiwell microscopy slides. Each EB was imaged on the MPLSM at 890 nm with a 520/35 bandpass filter for the live/dead probe and next imaged at 780 nm with a 457/50 bandpass filter for NADH expression at the same optical plane. B) Correlation between mean intrinsic fluorescence intensity per pixel of EBs and mean extrinsic fluorescence intensity per pixel. A strong correlation ($r = 0.69$; $P < 0.0001$) exists between the known indicator of cell death (live/dead probe) and NADH fluorescence intensity. Each dot represents a single EB imaged at the same plane for both intrinsic and extrinsic fluorescence using MPLSM. C) Representative images of NADH intensity of EBs and live/dead staining with (500 nM) and without (0 nM) staurosporine treatment. Bright field image is wide field and fluorescent images are optical sections. Scale bar = 200 µm.

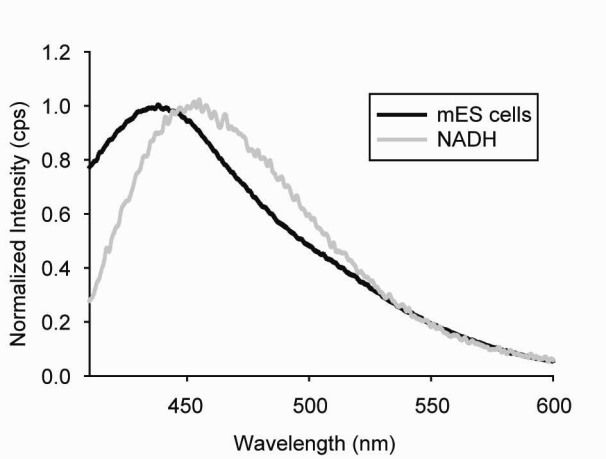

Figure 6.4 Spectrofluorometric analysis of emitted fluorescence of mouse embryonic stem cells following excitation at 350 nm. Fluorescence emission corresponding to the stem cells showed significant overlap with the emission profile of free NADH. The slight shift to the left of the emission profile corresponding to the stem cells reflects the contribution of bound NADH (emission maxima of 430 nm; free NADH emission maxima is 460 nm) [148].

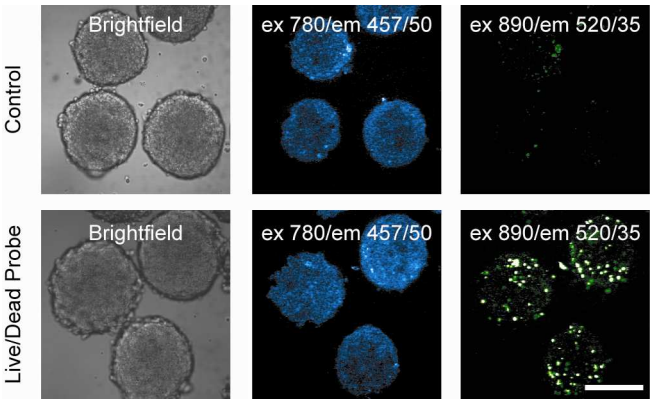

Figure 6.5 Assessment of intrinsic fluorescence intensity of NADH and extrinsic fluorescence intensity of the live/dead probe. To ensure fluorescence intensity did not overlap between imaging conditions defined for measures of intrinsic fluorescence intensity (excitation 780 nm, emission 457/50 nm) and extrinsic fluorescence intensity (excitation 890 nm, emission 520/35 nm), control EBs (top row) and those stained with the live/dead probe (bottom row) were imaged under both conditions. Almost no overlap was detected between conditions. Scale bar = 200 µm.

6.5 Low Levels of NADH Fluorescence Intensity of EBs Soon After Formation are Predictive of Functional Differentiation of Cardiomyocytes

Cell death is crucial for development and homeostasis *in vivo*, including in the heart [149-151]. The physiological relevance of cell death with the "quasi" development that occurs with stem cell differentiation *in vitro* has not been investigated. This is an especially challenging task since, unlike development, not all embryoid bodies give rise to the same cell types and the arrangement varies substantially. Thus a noninvasive biomarker of cell death in intact EBs, as we have shown above, is particularly useful for discerning the impact of cell death (especially at early phases) on the subsequent development of particular cell types and tissues. Here we investigate the impact of early cell death on cardiomyocyte differentiation and function. To this end, EBs were treated with staurosporine 3 days after EB formation. Following treatment, EBs were imaged at a single time point to detect extrinsic fluorescence of the live/dead probe and intrinsic fluorescence of NADH from a single optical section of individual EBs using MPLSM (**Figure 6.6A**). Each EB was then monitored daily for 9 days (12 days after EB formation) for the presence of beating areas indicative of cardiomyocyte differentiation. At day 12 after EB formation, EBs were probed for cardiac troponin T (cTnT) expression via immunofluorescence, to confirm the cardiomyocyte phenotype (**Figure 6.6B, C**). All beating areas detected exhibited corresponding positive staining for cTnT. EBs that formed beating areas comprised 44% of the total population. The mean intrinsic and extrinsic fluorescence intensity of each EB were plotted and those EBs that formed beating areas were distinguished from those that did not (**Figure 6.6D**). The EBs that gave rise to beating areas appeared to have low levels of both intrinsic and extrinsic fluorescence intensity. Indeed, both the intrinsic and extrinsic fluorescence intensity levels of EBs that formed beating areas versus those that did not form beating areas were statistically different ($P < 0.01$). Interestingly, if an arbitrary intensity level of 1.0 (normalized a.i.u.) was selected, 88% of EBs that formed beating areas had a mean NADH intensity per pixel, at day 3, below that level and similarly, 84% of EBs that formed beating areas had a mean live/dead probe intensity per pixel, at day 3, below that level. Thus, the population of EBs that formed beating areas could be enriched two fold by selecting EBs with low endogenous fluorescence intensity. Of note, EBs from all three treatment groups (0 nM, 100 nM and 500 nM) contributed to the total number of beating areas (75%, 22% and 3% of beating EBs respectively; $n > 20$ EBs for each concentration). Furthermore, within the group of EBs that developed beating areas, those with lower levels of either intrinsic or extrinsic fluorescence (i.e., less cell death) were likely to form beating areas sooner. EBs imaged on day 3 that formed beating areas by day 6 exhibited

statistically lower levels of NADH and live/dead fluorescence intensity than EBs that formed EBs on day 12 or did not form beating areas. Similarly, EBs imaged on day 3 that formed beating areas by day 9 exhibited statistically different levels of NADH and live/dead fluorescence intensity than EBs that did not form beating areas (**Figure 6.6E**). This trend was maintained even without treatment with staurosporine when comparing EBs that formed beating areas by day 6 (mean intrinsic intensity/pixel 0.78 $\pm$ 0.11) to those that did not form beating areas by day 6 (mean intrinsic intensity/pixel, 0.81 $\pm$ 0.07). Thus, NADH levels determined at early time points may be predictive of the temporal onset of functionally differentiated cells of EBs and so might be used as a biomarker for noninvasive analysis and purification of stem cell aggregates for both research and clinical application.

6.6 Sorting EBs based on NADH Fluorescence Intensity

To demonstrate the use of NADH as a non-invasive biomarker to detect a distinct cell fate within a three dimensional tissue, STS treated (500nM) and non-treated day 3 EBs were introduced into the MPFC in equal parts with the intent of positively sorting EBs undergoing trauma (**Figure 6.7A**). Previously, we have shown that the global fluorescence intensity of NADH peaks approximately 3h after STS treatment, therefore sorting on the MPFC was performed at this time. Before sorting, control populations were analyzed without sorting, both treated and non-treated EBs were analyzed on the MPFC (**Figure 6.7B**). The fluorescence intensity threshold was set such that 95% of treated EBs would be positively selected. The fluorescence intensity was normalized to the mean of the total sample input population for a given experiment, due to biological and instrumental variability between experiments. Post flow static imaging was performed for one of six trials to determine the relative NADH fluorescence intensity of the resulting populations. This ensured that those EBs selected in flow display the same degree of fluorescence intensity when measured statically. Normalized mean fluorescence intensity detected in flow of sorted compared to main outlet populations were not statistically different from static measurements of the isolated EB populations after flow (1.6 $\pm$ 0.2 and 0.7 $\pm$ 0.2, 1.5 $\pm$ 0.3 and 0.8 $\pm$ 0.2, respectively, **Figure 6.7C**). Moreover, sorting efficiency was determined by dividing the number of positively sorted EBs that were collected by the number of EBs detected in flow, and was determined to be 80% $\pm$ 18% (n=3). The experiments yielded a total enrichment ratio of 13 $\pm$ 16.6 (**Figure 6.7D**).

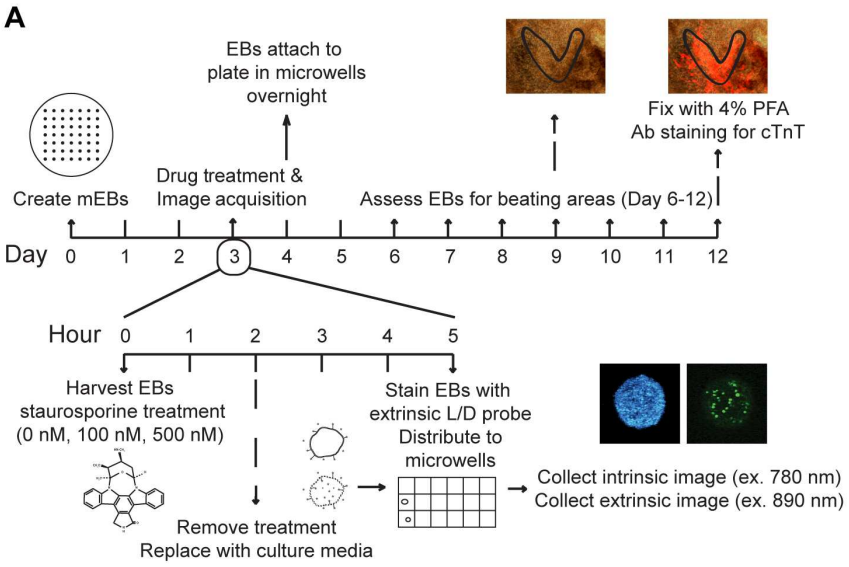
A
EBs attach to plate in microwells overnight
Fix with 4% PFA
Ab staining for cTnT
Create mEBs
Drug treatment & Image acquisition
Assess EBs for beating areas (Day 6-12)
Day 0 1 2 3 4 5 6 7 8 9 10 11 12
Hour 0 1 2 3 4 5
Harvest EBs
staurosporine treatment
(0 nM, 100 nM, 500 nM)
Stain EBs with extrinsic L/D probe
Distribute to microwells
Collect intrinsic image (ex. 780 nm)
Collect extrinsic image (ex. 890 nm)
Remove treatment
Replace with culture media

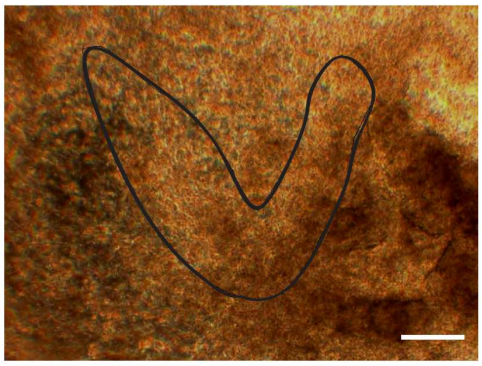
B

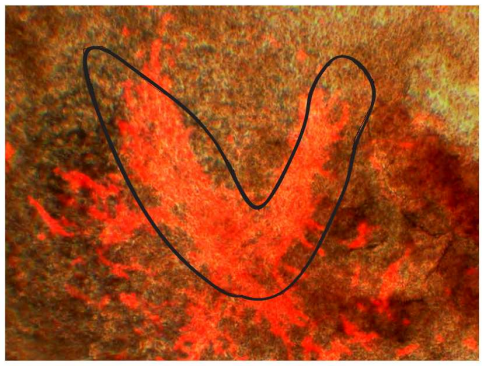
C

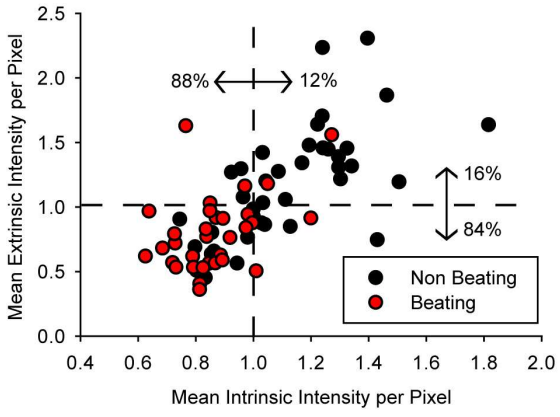
D
Mean Extrinsic Intensity per Pixel
Mean Intrinsic Intensity per Pixel
88%
12%
16%
84%
Non Beating
Beating

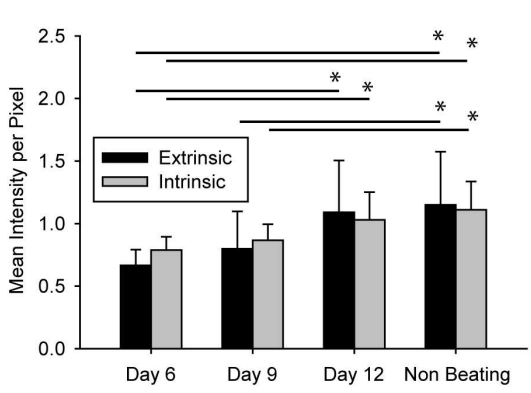
E
Mean Intensity per Pixel
Extrinsic
Intrinsic
Day 6
Day 9
Day 12
Non Beating

Figure 6.6 Intrinsic fluorescence intensity of NADH as a predictive index of cardiomyocyte differentiation. A) Schematic depicting the experimental approach designed to determine whether NADH intensity levels at an early time point after EB formation are indicative of later function of differentiated cardiomyocytes. EBs were treated with staurosporine 3 days after EB formation. Following treatment, EBs were imaged at a single time point to detect extrinsic fluorescence of the live/dead probe and intrinsic fluorescence of NADH from a single optical section of individual EBs using MPLSM. Each EB was then monitored daily for 9 days (up to 12 days after EB formation) for the presence of beating areas indicative of cardiomyocyte differentiation. B) Microscopic observation of a beating area. Shown is a bright field image with the beating region outlined in black. C) Cardiac troponin T (cTnT) staining corresponds to microscopic observation of beating behavior. EBs were formed and plated in 9 x 2 microslides. Upon observation of beating areas, immunofluorescence staining for cTnT was performed. In all cases where beating cells were observed, cTnT staining was also observed. Shown is the outline of the beating area and corresponding cTnT staining (red) superimposed on the bright field image. Scale bar = 200 µm. D) Distribution of EBs which give rise to beating areas at 6 – 12 days after EB formation and corresponding levels of intrinsic fluorescence intensity of NADH and extrinsic fluorescence of the live/dead probe detected 3 days after EB formation. E) Comparison of mean intrinsic fluorescence intensity of NADH of EBs and the time after EB formation that beating areas appear. EBs with low mean intensity per pixel of intrinsic fluorescence intensity of NADH soon after EB formation are more likely to give rise to beating cardiomyocytes at later time points than those with high levels early on ($*P < 0.05$).

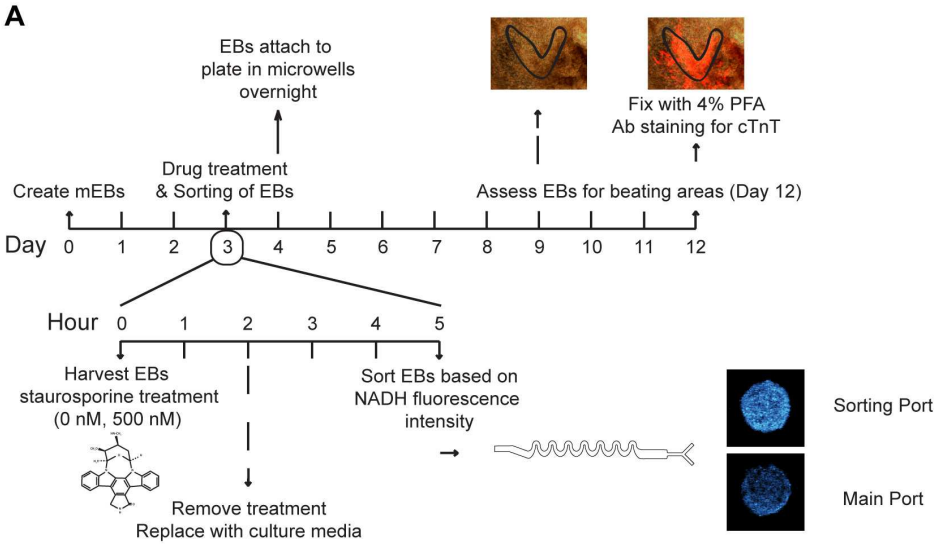
A
EBs attach to plate in microwells overnight
Fix with 4% PFA
Ab staining for cTnT
Drug treatment & Sorting of EBs
Create mEBs
Assess EBs for beating areas (Day 12)
Day 0 1 2 3 4 5 6 7 8 9 10 11 12
Hour 0 1 2 3 4 5
Harvest EBs staurosporine treatment (0 nM, 500 nM)
Sort EBs based on NADH fluorescence intensity
Remove treatment
Replace with culture media
Sorting Port
Main Port

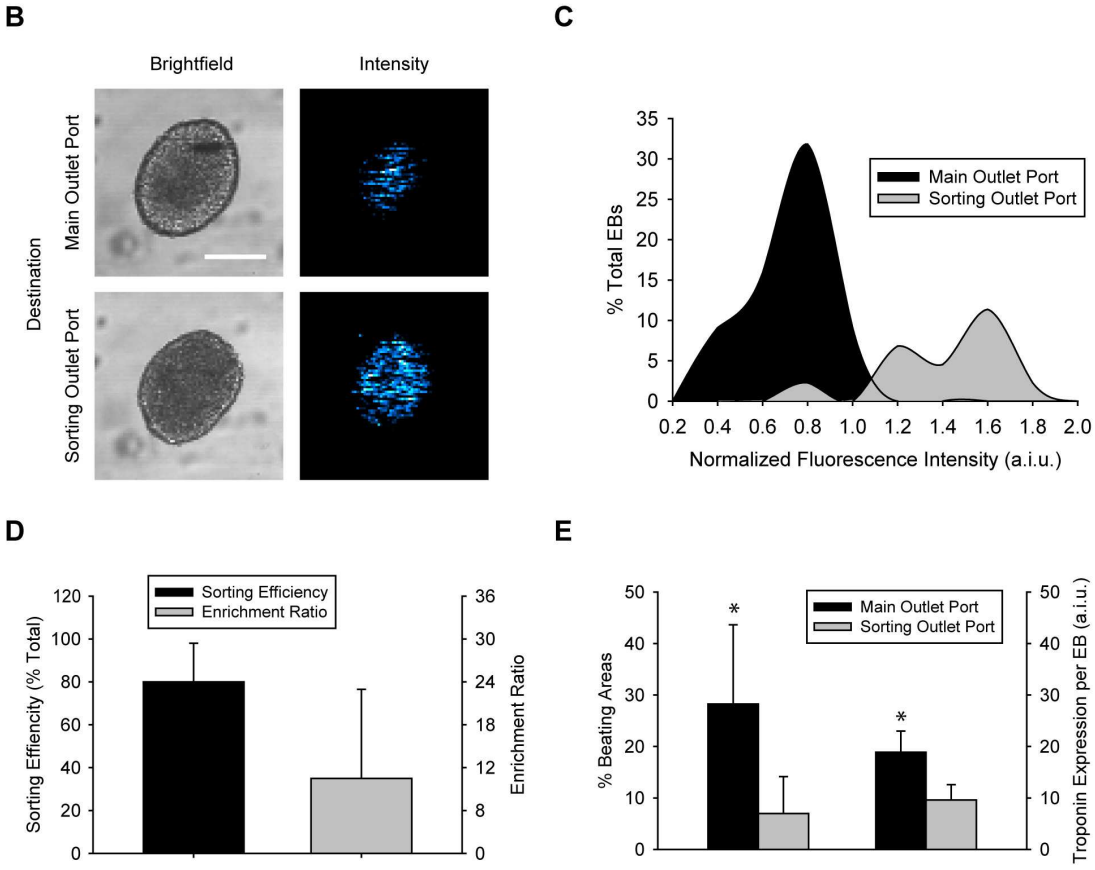
B
Brightfield
Intensity
Destination
Main Outlet Port
Sorting Outlet Port
C
% Total EBs
Normalized Fluorescence Intensity (a.i.u.)
Main Outlet Port
Sorting Outlet Port
D
Sorting Efficiency
Enrichment Ratio
Sorting Effiencity (% Total)
Enrichment Ratio
E
% Beating Areas
Troponin Expression per EB (a.i.u.)
Main Outlet Port
Sorting Outlet Port

Figure 6.7 Sorting HMI EBs based on NADH fluorescence intensity. (A) EBs were harvested on day 3 of differentiation and either treated with staurosporine (500nM) or not treated (0 nM) for 2 hours. EBs were then sorted based on NADH fluorescence intensity 3 hours post treatment, and subsequently plated onto polystyrene dishes and cultured. On day 12 of differentiation, EBs were assessed for beating areas and fixed to stain for cTnT. (B) Those EBs with NADH intensity greater than 1.1 a.i.u. (i.e. the sorting threshold) were positively selected and directed to the sorting outlet port, while those with less than 1.1 a.i.u. naturally flowed to the main outlet port. (C) Fluorescence distributions of resulting sorted populations. (D) Sorting efficiency and enrichment ratio of 3 separate experiments. (E) The percentage of beating areas and cTnT expression per EB of resulting sorted populations (*$P < 0.05$).

Finally, to demonstrate the utility of this method for purifying functional differentiated phenotypes, we quantified the percentage of EBs that formed beating cardiomyocytes by plating the sorted populations of EBs and observing the development of beating areas up until day 13 of differentiation when they were fixed and stained for cardiac troponin (cTnT). The default population had a significantly higher percentage of beating areas (30.7 $\pm$ 5.6%) compared to the sorted population (7.0 $\pm$ 7.1%). This qualitative assessment was confirmed with significantly higher cTnT expression per EB (18.9 $\pm$ 4.1 a.i.u. and 9.6 $\pm$ 3.0 a.i.u.) for the main and sorting populations, respectively (**Figure 6.7E**).

6.7 Sorting Pancreatic Islets based on NADH fluorescence Intensity

To test the ability of the MPFC to non-invasively purify a healthy population of pancreatic islets we analyzed and sorted the microtissues based on NADH expression a short time after explanted from mice (approximately 3h). NADH expression per islet was calculated on the MPFC by employing our real-time fluorescence intensity per unit area measurement such that the intensity for each islet was normalized based on size. A pre-sort analysis trial was conducted to determine the size and fluorescence intensity distribution of a representative islet fraction (**Figure 6.8A, B**). We were interested in the size distribution because large microtissues of varying size and shape have very unique flow characteristics within our microfluidic device. As a consequence, the sorting pulse (i.e. duration of time the sorting outlet port is open for a single detected event) must be increased to accommodate a wider range of particle velocities. From the histogram depicting NADH fluorescence intensity, a threshold was set such that the islets with the highest NADH expression (i.e. top 25%) would be positively sorted (**Figure 6.8B**). In this way, we sought to remove a population with a high degree of cell death. After sorting, islets from both the main and sorting outlet ports were collected and counted (**Figure 6.8C**). Sorting efficiency was determined by comparing the number of islets physically collected from the sorting port, to the number of positive events detected in flow. A sorting efficiency of 77.1 $\pm$ 12.0% and enrichment ratio of 20.7 $\pm$ 12.0 were achieved (**Figure 6.8D**). Thus, sorting parameters (i.e. pulse and time delay) and imaging settings were properly set to accommodate a very broad size range of islets.

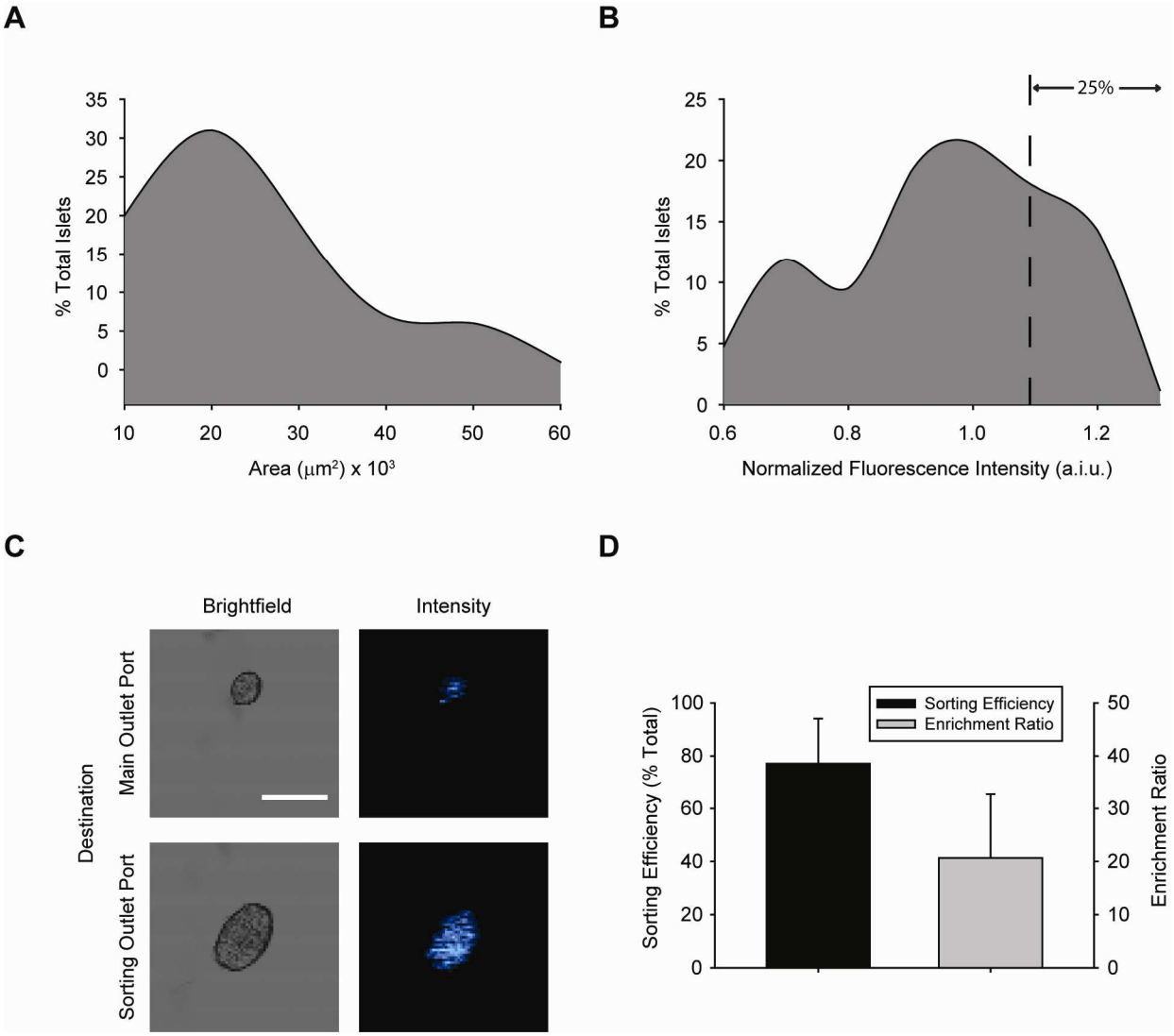

Figure 6.8 Sorting of pancreatic islets based on NADH fluorescence intensity. (A) Size distribution of pancreatic islets measured during pre-sort analysis trial (n=84). (B) NADH fluorescence intensity distribution measured in pre-sort analysis trial (n=84). (C) Islets with NADH intensity greater than 1.1 a.i.u. (i.e. the sorting threshold) were positively selected and directed to the sorting outlet port, while those with less than 1.1 a.i.u. flowed to the main outlet port. (D) Sorting efficiency and enrichment ratio of 5 separate sorting trials.

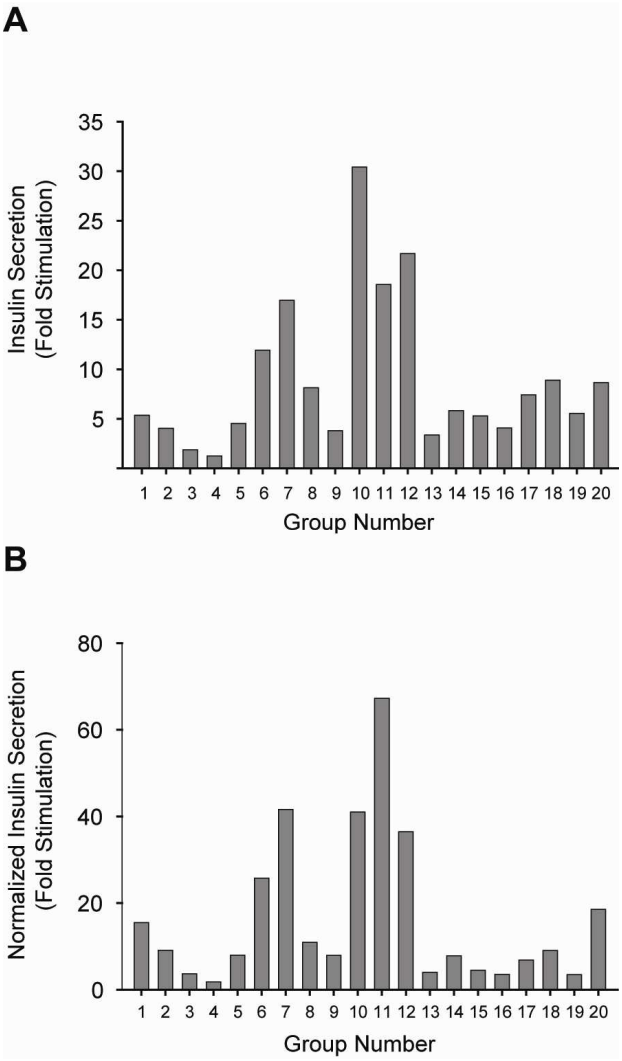

Figure 6.9 Insulin secretion response of islets grouped according to increasing (1 – 20) NADH fluorescence intensity. (A) Fold stimulation (ratio of stimulated to basal secretion of insulin) of islets grouped based on their relative expression of NADH fluorescence intensity as measured in microwells on the MPLSM. Group 1 is made up of 4 islets with the lowest NADH intensity of the 80 islets imaged, while group 20 contains 4 islets with highest NADH intensity relative to the entire group. (B) Fold stimulation normalized to the area of islets as measured on the MPLSM.

Table 6.1 Insulin secretion response of islets grouped according to increasing NADH fluorescence intensity

Group	NADH Intensity	Insulin Secretion	Normalized Insulin Secretion
1	0.64	15	5
2	0.73	9	4
3	0.77	4	2
4	0.80	2	1
5	0.84	8	5
6	0.87	26	12
7	0.90	42	17
8	0.92	11	8
9	0.95	8	4
10	0.97	41	30
11	0.99	67	19
12	1.02	36	22
13	1.03	4	3
14	1.06	8	6
15	1.09	4	5
16	1.15	4	4
17	1.18	7	7
18	1.24	9	9
19	1.32	3	6
20	1.56	19	9

6.8 Detection of NADH Fluorescence Intensity in Pancreatic Islets soon after Explantation can be Predictive of Insulin Secreting Capacity

To determine whether metabolic activity of islets, as measured by the NADH fluorescence intensity is indicative of the ability to secrete insulin in response to glucose stimulation, we imaged and subsequently grouped islets based on the NADH expression on the MPLSM soon after isolation from mice. Islets were placed into 9x2 ibidi microwells and excited at 780 nm to measure NADH fluorescence intensity. Next, images were analyzed by measuring fluorescence intensity per unit area using ImageJ software. Based on these measurements, islets were ordered according to their relative NADH intensity from lowest to highest and assigned to groups of 4. Group 1 contains the four islets with the lowest NADH intensity, and each subsequent group has a higher mean NADH intensity than the preceding group (**Table 6.1**). Basal insulin secretion was defined as response of islets to low glucose concentration (1.7mM), while stimulated insulin secretion was defined as response of islets to high glucose concentration (16.7mM). Fold stimulation was determined by taking the ratio of stimulated to basal insulin secretion. Fold stimulation was plotted according to groups of islets (increasing from 1-20) defined by increasing NADH fluorescence intensity (**Figure 6.9A, B**). Interestingly, islets with the greatest fold-stimulation and thus those most able to respond to glucose stimulation were groups 7, 10, 11, 12 (gray rows, **Table 6.1**), corresponding to normalized NADH intensities of 0.9, 0.97, 0.99, and 1.01, respectively. Groups 1-6 and Groups 13-20, corresponding to NADH intensities of 0.64-0.87 and 1.03-1.56, respectively, registered minimal fold-stimulations (<20). Therefore, islets with medium levels of NADH fluorescence intensity, relative to the whole population, have a higher potential for secreting insulin in response to glucose stimulation. These data can now be used to inform studies aimed to purify functional islets for transplantation.

6.9 Discussion

In this study we show that the intensity of NADH fluorescence changes in response to staurosporine-induced cell death in murine EBs and so might be used to reliably and noninvasively assess viability of EBs and other microtissues. Increased NADH expression after induction of cell death has been observed in other cell types [129-131], though this is the first study to show such a response in intact cell aggregates. Furthermore, we utilized real-time imaging processing tools to sort a mixed population of treated and non-treated EBs based on NADH

fluorescence intensity and isolated a population that yields a significantly higher percentage of beating areas than the unsorted population.

We have focused here on analysis of EBs, since there is still much to learn from these aggregates in terms of the spatial and temporal cues that give rise to particular differentiated cell types [152-155]. We were particularly interested in the impact of severe cellular stress on later, long-term function of mature cells types. Future studies could more effectively tap the ability to track intrinsic fluorescence of the same EB over time, by assessing the progressive contribution of cell death to the developing EB. It is possible that cell death at localized and low levels may be beneficial and not detrimental in the developing EB. Similar approaches could be applied to any cell aggregate, including tumor spheroids, pancreatic islets, neurospheres, cardiospheres, lymphoblastoid cells and perhaps most interestingly to *in vitro*, three-dimensional (3D) engineered tissue models. One primary goal of engineered tissue models is to present cues in a more defined manner than that of the heterogeneous EB (reviewed in [156-157]) and noninvasive assessment of cell death could advance these efforts tremendously. We emphasize here the utility of NADH as a biomarker of stem cell death in cell aggregates, however the approach is certainly applicable to analysis of single stem cells as well. In this case single photon fluorescence microscopy and traditional flow cytometry techniques might be effectively employed since sample thickness is relatively small. In all cases, the spectral profiles in both excitation and emission should be carefully considered and experimental method accordingly adjusted so as to avoid signal from alternative sources of intrinsic fluorescence that could include cellular elements, extracellular elements or even certain small molecules used to induce cell death (i.e., camptothecin) that fluoresce in the same region of the emission spectrum as NADH.

Changes in NADH intensity with cell death are time dependent and so would most effectively align with changes in cell death soon after induction of trauma or exposure to signaling molecules that promote cell death. Time-dependence of NADH expression is beneficial in conditions of induced cell stress, since analyses can be orchestrated to correspond with peak expression. However, in the course of typical culture, stem cell aggregates exhibit constant, low level, cell death that should be detectable at any given time point. In other words, the large number of cells analyzed (as opposed to a single cell), ensures a high probability of accurately capturing the global health of the EB. Indeed, EBs without staurosporine treatment that ultimately give rise to beating areas exhibit the same trend of lower mean intrinsic fluorescence intensity than EBs that do not generate beating areas.

It should be noted that the distribution pattern of fluorescence intensity of the intrinsic fluorophores and extrinsic markers are not alike. The extrinsic dye yields a punctate pattern while the intrinsic fluorescence is diffuse. This difference likely reflects the difference not only in binding target but also in the temporal window of cell death associated with each "probe". The extrinsic marker identifies cells with permeable membranes, likely at the later stages of cell death. In contrast, the autofluorescent intensity corresponds to fluctuations of NADH that can occur at both early and late stages of cell death and does not necessarily imply a compromised cell membrane. Additionally, the heterogeneity of cell types comprising the aggregates may be more or less resistant to cell death and associated membrane permeability (extrinsic probe), while even those cell types more resistant to cell death will exhibit fluctuations in NADH in response to stressful stimuli (i.e., staurosporine treatment).

Another important consideration is that NADH amount and state in healthy stem cells and their progeny can be altered as a consequence of other cell functions [158], especially differentiation [79-80, 159-163]. A variety of studies suggest that pluripotent stem cells are metabolically distinct from differentiated cells [164-167]. As one example, pluripotent stem cells can proliferate, and may preferentially maintain pluripotency, in a hypoxic environment [168]. These studies suggest that stem cells are preferentially using, or at least are capable of using, non-oxidative pathways as opposed to oxidative phosphorylation predominantly employed by most mature cell types. Thus, we and others have begun to investigate the concept that intrinsic fluorescence signatures, including fluorescence intensity and fluorescence lifetime [44] of bound and free NADH [117] in particular, could be used to identify changes with stem cell differentiation [49]. Specifically, human mesenchymal stem cells (MSCs) show an increase in NADH fluorescence intensity and the fluorescence lifetime of bound NADH as they differentiate toward bone and fat lineages [161]. In addition, discernible differences in fluorescence intensity and lifetime can be identified with differentiation of salivary gland stem cells [160]. Thus it is clear that intrinsic fluorescence of metabolites can serve to distinguish viable cells from dead cells and mature cells from progenitors. Lacking are comprehensive studies and robustly defined parameters to distinguish each stem cell state (e.g., viable, proliferative, migratory and differentiating) and sub-state (e.g., cell death due to apoptosis, necrosis and autophagy). However, the work presented here takes one clear step toward defining parameters for viability of stem cells at time points when the majority of cells of EBs are still in a pluripotent or at least multipotent state.

Here, consistent increases in NADH fluorescence intensity are evident with induced cell death in EBs and it was demonstrated that the percentage of EBs that give rise to functional cardiomyocytes is higher in EBs that had

lower fluorescence intensity, either endogenous (corresponding to NADH) or exogenous (corresponding to a commercially available live/dead fluorescent probe), soon after EB formation. To further demonstrate the utility of NADH as an indicator of cell death, we sorted EBs on the MPFC based on their endogenous fluorescence. Consistent with static experiments, those EBs with low NADH fluorescence intensity were more likely to adopt functional cardiomyoctes during differentiation. This technology, and others like it (reviewed in [169]), coupled with the knowledge gained in this study, have tremendous potential for both basic research and clinical cellular transplantation in that the structure of the aggregate can be maintained, exogenous labels avoided and purification achieved in an enhanced-throughput fashion.

Pancreatic islets have been identified as a microtissue population that endure stressful explantation procedures that result in variable amounts of cell death. Re-implantation of these pancreatic islets have clinical potential for treating type I diabetes through restoration of beta cell function within islets if the islets can be effectively managed ex vivo [170]. Such a clinical procedure would greatly benefit from a means to non-invasively purifying microtissues exhibiting higher percentages of viable cells. We have taken initial steps in determining the potential of using NADH as an indicator of cell death in pancreatic islets, and studied how that will impact on functional capacity and potential for re-implantation into mice. Grouping islets based on relative expression levels of NADH fluorescence, we sought to investigate a possible correlation with functional potential (i.e. insulin secretion). We found, those islets with a mid-level expression of NADH fluorescence had the highest ratio of stimulated to basal insulin secretion (fold stimulation) in response to glucose stimulation, whether or not islet size was used to normalize measured secretion values (**Figure 6.9A, B**). We have also shown the ability to sort pancreatic islets with high NADH expression, in an attempt to remove islets with a high percentage of dead cells. Certainly, cell death contributes to the metabolic signature of the pancreatic islets as a whole, and it is very likely that NADH fluorescence will increase with increasing cell death, however more studies will be necessary to clarify this relationship. To further investigate this relationship, the relative contributions of cell death to the overall NADH fluorescence intensity could be determined with static experiments performed where NADH expression is compared to an extrinsic live/dead probe (similar to those performed on EBs). Additionally, we will investigate NADH fluorescence intensity at incremental time points soon after explantation to determine when analysis and/or sorting should be performed and whether islets exhibit a similar profile to stem cell aggregates after staurosporine treatment.

Further complicating the relationship between insulin secretion and NADH intensity of intact islets is their heterogeneous cell composition. Mouse pancreatic islets are composed of roughly 75% insulin secreting beta cells, 15% glucagon secreting alpha cells, as well as smaller percentages of delta, epsilon and pancreatic polypeptide cells [171]. Alpha cells have a higher basal metabolic rate than beta cells, secreting glucagon at low blood glucose levels, and are inhibited when blood glucose levels rise [172]. Recently, co-localization studies elucidated the relationship between alpha cells (detected by a EYFP reporter controlled by a glucagon promoter) and NADH intensity within intact islets with two photon excitation [172-173]. Similar studies detecting the presence of beta cells and other cell types making up the pancreatic islet will contribute to the understanding of the overall islet metabolic signature. Indeed, NADH fluorescence intensity drastically increases in response to glucose stimulation [115, 174], primarily as a result of the increase in metabolic demand from pancreatic beta cells to secrete insulin. However, measurement of NADH intensity in future sorting trials will be performed at low (basal) glucose levels, where we hypothesize that a high degree of cell death within islets will induce a discernible increase in NADH intensity compared to those islets with minimal cell death. Future studies will shed light on the many contributors of the metabolic profile of pancreatic islets, and potentially enable the MPFC to non-invasively purify healthy fractions of islets for transplantation.

CHAPTER 7
Discussions, Future Directions and Recommendations

The ultimate goal of this project was to develop a microfluidic device that could be coupled to a standing multiphoton laser scanning microscope, and would provide a platform to analyze and sort microtissues based on a variety of characteristics, most notably endogenous properties. To this end, the MPFC has been validated to measure and subsequently sort EBs based on size and fluorescence intensity originated from exogenous (e.g. genetic reporter constructs) and endogenous (e.g. NADH) fluorophores. Although experimental goals have been met, there are still many improvements to be made that would further increase the utility of the system. Future modifications to all three primary components of the MPFC (i.e. fluidics, optics and data acquisition) would contribute to improving the quality of results and user experience. Such modifications would be made with the focus on 1) increasing the speed of acquisition while improving 2) the accuracy of the measurement on microtissues, and 3) further automating the system with an enhanced user-interface.

7.1 Fluidics

Modifications to the fluidic component of the MPFC would improve the accuracy of the measurement and sorting efficiency of microtissues. The purpose of the fluidic component is to precisely and reproducibly deliver microtissues to a defined spatial position to be analyzed, and additionally, to sort all particles that are selected by the software. In a perfect world, particles of varying size and shape would flow in a single file line past the interrogation region at a constant velocity, such that no particles align on the edge of the image display (i.e. interrogation region), or miss it completely. Many confounding factors such as size, shape, adhesion, and agglomeration can impact microtissue position and velocity within the flow cell. One way to address these problems and improve the performance of the fluidic component is simply to increase flow rate. In preliminary studies, we have shown that increasing the flow rate of the system will more tightly focus particles of varying sizes toward the center line of the channel while also decreasing the range of velocities at which the particles travel. Moreover, the particle separation along the long axis of the channel is improved, reducing the number of particle-particle interactions and coincidence events [84]. As particles are more precisely delivered to the interrogation region, imaging constraints like using low optical zoom and low resolution may be reduced, thus improving the quality of the image and measurement. Currently flow rates are limited by the speed of image acquisition. As

scanning technology improves, increasing flow rates of the system is a simple adjustment that will allow for more accurate measurements, increased throughput and higher sorting efficiencies. Another attractive solution for more efficient focusing of microtissues in flow, is to not only focus them laterally, but also vertically, such that particles are focused in two dimensions.

This so called 2-D focusing has been accomplished for small particles and single cells, but could be designed to accommodate larger 3-D microtissues as well. Howell Jr. *et. Al*[91] proposed an easily fabricated design requiring only two inputs that requires carving chevron features into the top and bottom of a flow channel. The chevrons effectively transport fluid flowing on the sides to the middle along the top and bottom of the channel, compressing the sample stream vertically. Each additional chevron that is added to the design will produce a greater vertical focusing affect as well as a slight expansion in the horizontal direction. Sheath to sample flow rates ratios, as well as number of chevron pairs will ultimately determine the area and shape of the cross sectional area of the sample stream. We have performed preliminary experiments with focusing fluorescein dye both laterally and horizontally, with the use of chevrons in a scaled up microfluidic channel that could accommodate large particles (**Supplementary Figure 4**, **Appendix**). As throughput of the system is able to improve, implementing a 2-D focusing mechanism would both improve the accuracy of particle detection and improve sorting efficiency by providing more predictable particle velocities.

Modeling of microtissue interactions in microfluidic devices would provide a platform for optimizing conditions in microtissue analysis and sorting experiments. One extensive study modeled particle-particle interactions in flow with various force coupling methods (one-way, two-way and four-way), that was dependent on the volume ratio of particles in flow [89]. These studies and others [175-176] have shed light on key concepts such as drafting, kissing, tumbling effects (DKT), wall-induced lift forces, and rotational effects of spherical particles in two-phase particulate flows. In light of the many forces imposed on large particles in the context of flow, it is important to understand the implications of input parameters (i.e. particle concentration, size) on the performance of the device or instrument. Currently, two-phase particulate flow modeling can be computationally intensive, and simulations have been limited to spherical particles. As simulations are typically performed on spheres, it would be beneficial to extend simulations to other types of 3-D tissues of different shapes like cubes, disks, or tubes that are often engineered in the lab. Currently, flow rates on the MPFC create highly diverse fluidic interactions when introducing non-spherical shapes of microtissues that make analysis and sorting difficult. Future modeling efforts

investigating alternative flow cell designs that would complement various types of tissue constructs would further enhance the capabilities of the MPFC, and increase the number of applications available to users.

7.2 Optics

Improvements to the optical scanning electronics component of the MPFC would greatly increase speed of image acquisition. The MPFC uses a laser scanning control system that is mostly limited in acquisition speed by the galvanometer mirrors which are driven with a linear sawtooth control waveform at the rate of several microseconds per pixel. This results in a effective scan rate ranging from 500 ms to 2 s depending on image dimensions. This scanning system is ideal for high resolution conventional multiphoton but not for the MPFC where speed is critical. For future MPFC development there are several strategies we are investigating for faster image acquisition. These fall into two general categories: 1) alternative scanning approaches with the current galvanometer mirrors such as line scanning and faster waveform patterns 2) alternative scanning mirror approaches such as resonant scanning mirrors that can collect 30 frames/second or higher by allowing the beam to be raster-scanned across the specimen at higher speeds. Increased scanning speeds would allow the volumetric flow rates to be increased by an order of magnitude, greatly reducing the variability of particle position and velocity within the flow cell. Consequently, this would allow for the user to increase zoom and/or use objective lenses with a higher numerical aperture, further improving the resolving power of the system. Finally, image scanning speeds would allow for higher throughput and sorting rates of the system, allowing the MPFC to take one step closer to becoming a clinically relevant instrument.

Another important improvement to the optical setup of the MPFC will be to add one or more PMTs for the ability to simultaneously detect and sort based on two or more fluorescent markers present in an EB. By increasing the number of detection parameters, users will be able to target specific cells that necessitate the detection of more than one surface marker (e.g. CD profile for Mesenchymal Stem Cells) within 3D microtissues. Similarly, one could envision sorting based on the presence of transcriptional reporter lines as well as metabolic intermediates such as NADH to at once separate viable cells (NADH) with a propensity to become a particular cell type (transcriptional reporter) in microtissues in an enhanced throughput fashion.

7.3 Software

Future modifications to the software component of the MPFC will strive to develop a fully automated system. In the current version of the Flow Cytometry software in WiscScan, many functionalities and options are now available that have partially automated experiments and improved results. For instance, Wiscscan completely controls the fluidic component by allowing the user to start and stop flow, toggle outlet pins, and rinse all lines. Additionally, the MPFC software allows the user to define a number of parameters to sort based on, including size, mean intensity and total intensity, and displays measurements of all of these parameters in real-time. Despite the improvements that have been made, the software will require more improvements to fully maximize the applicability of this technology. Future efforts should seek to design a real-time graph display, a common feature in single cell flow cytometers for a more user-friendly visualization of the data. Commonly, such features allow for adjusting sorting thresholds in real-time while displaying percentages of cells present in regions of interest. This feature helps the user make decisions on the fly, and easily remove unwanted outliers from their data. Additionally, implementing automated sample handling programs will provide much more user-friendly setup and collection procedures for operation of the MPFC. In its current state, the MPFC requires the user to manually remove samples from collection tubes. In the future, sample and collection reservoirs should be equipped with precise fittings to connect to the fluidic network to enable more system checkpoints, and remove the necessity of a "skilled" user to run the MPFC. The software improvements along with slight modifications to the fluidic assembly will provide a more sound experimental experience for the user, and allow more investigators to use the instrument.

7.4 Investigations of intrinsic fluorophores and utility for study of 3D microtissues

Advanced optical techniques accessible on the MPFC can yield information related to the physiological state and molecular environment of cells or microtissues [39]. We have already utilized the MPFC for detection of intrinsic fluorophores, such as NADH and FAD. As previously described, NADH and FAD are important metabolic intermediates that can provide information about cell and tissue viability and even differentiation potential. If image scanning speeds were increased such that single cell resolution was feasible, EBs could theoretically be sorted based on the number of pluripotent cells [49] or differentiation potential. Another very interesting application unique to two-photon excitation is second harmonic generation [177]. This non linear optical phenomenon has the capability of detecting biological structures such as collagen I, myosin, and microtubules [178-179]. Static experiments

attempting to correlate the presence of these structures and their biological impact may provide more applications for sorting 3D tissues on the MPFC in a non-invasive manner. For instance, detection of SHG on the MPFC could provide a platform for new 3D model systems such as mesenspheres [180] that are known to produce collagen and other ECM proteins during differentiation. In this way, expression levels of various ECMs could be predictive of differentiated progeny of mesenchymal stem cells. Similarly, the ECM could be probed on the MPFC in explanted tissues such as pancreatic islets, where the presence of such proteins are critical to survival, functional insulin secretion and overall architecture of islets [181].

CHAPTER 8

Bibliography

1. Giobbe, G.G., et al., *Confined 3D microenvironment regulates early differentiation in human pluripotent stem cells.* Biotechnol Bioeng, 2012. **109**(12): p. 3119-32.

2. Schmeichel, K.L. and M.J. Bissell, *Modeling tissue-specific signaling and organ function in three dimensions.* Journal of cell science, 2003. **116**(12): p. 2377-2388.

3. Kajiwara, K., et al., *A synthetic peptide corresponding to residues 301-320 of human Wnt-1 promotes PC12 cell adhesion and hippocampal neural stem cell differentiation.* Peptides, 2008. **29**(9): p. 1479-85.

4. Elknerova, K., et al., *Growth inhibitory effect of the antibody to hematopoietic stem cell antigen CD34 in leukemic cell lines.* Neoplasma, 2007. **54**(4): p. 311-20.

5. Buschke, D.G., et al., *Multiphoton Flow Cytometry to Assess Intrinsic and Extrinsic Fluorescence in Cellular Aggregates: Applications to Stem Cells.* Microsc Microanal, 2010: p. 1-16.

6. Buschke, D.G., et al., *Microfluidic sorting of microtissues.* Biomicrofluidics, 2012. **6**(1): p. 14116-1411611.

7. Buschke, D.G., et al., *Cell death, non-invasively assessed by intrinsic fluorescence intensity of NADH, is a predictive indicator of functional differentiation of embryonic stem cells.* Biology of the Cell, 2012. **104**(6): p. 352-364.

8. Van Dilla, M.A., et al., *Cell microfluorometry: a method for rapid fluorescence measurement.* Science, 1969. **163**(872): p. 1213-4.

9. Xuan, X. and D. Li, *Focused electrophoretic motion and selected electrokinetic dispensing of particles and cells in cross-microchannels.* Electrophoresis, 2005. **26**(18): p. 3552-60.

10. Lancaster, C., et al., *Rare cancer cell analyzer for whole blood applications: Microcytometer cell counting and sorting subcircuits.* Methods, 2005. **37**(1): p. 120-127.

11. Lin, C.H., et al., *Vertical focusing device utilizing dielectrophoretic force and its application on microflow cytometer.* Journal of Microelectromechanical Systems, 2004. **13**(6): p. 923-932.

12. Goddard, G. and G. Kaduchak, *Ultrasonic particle concentration in a line-driven cylindrical tube.* Journal of the Acoustical Society of America, 2005. **117**(6): p. 3440-3447.

13. Goddard, G., et al., *Single particle high resolution spectral analysis flow cytometry.* Cytometry A, 2006. **69**(8): p. 842-51.

14. Shi, J., et al., *Three-dimensional continuous particle focusing in a microfluidic channel via standing surface acoustic waves (SSAW).* Lab on a Chip. **11**(14): p. 2319-2324.

15. Perfetto, S.P., P.K. Chattopadhyay, and M. Roederer, *Seventeen-colour flow cytometry: unravelling the immune system.* Nature Reviews Immunology, 2004. **4**(8): p. 648-655.

16. Bonner, W.A., et al., *Fluorescence activated cell sorting.* Rev Sci Instrum, 1972. **43**(3): p. 404-9.

17. Hulett, H.R., et al., *Development and application of a rapid cell sorter.* Clin Chem, 1973. **19**(8): p. 813-6.

18. Stovel, R., *The influence of particles on jet breakoff.* Journal of Histochemistry and Cytochemistry, 1977. **25**(7): p. 813.

19. HANSEN, W.P., R.J. GERSHMAN, and P.B. KRAULEDAT, *AXIAL PATTERN ANALYSIS AND SORTING INSTRUMENT FOR MULTICELLULAR ORGANISMS EMPLOYING IMPROVED LIGHT SCATTER TRIGGER*. 1999, Google Patents.

20. Peeters, J.C., et al., *Optical plankton analyser: a flow cytometer for plankton analysis, I: Design considerations.* Cytometry, 1989. **10**(5): p. 522-8.

21. Dubelaar, G.B., et al., *Optical plankton analyser: a flow cytometer for plankton analysis, II: Specifications.* Cytometry, 1989. **10**(5): p. 529-39.

22. Gray, D.W., et al., *Separation of pancreatic islets by fluorescence-activated sorting.* Diabetes, 1989. **38 Suppl 1**: p. 133-5.

23. Fernandez, L.A., et al., *Validation of large particle flow cytometry for the analysis and sorting of intact pancreatic islets.* Transplantation, 2005. **80**(6): p. 729-37.

24. Odorico, J., B. Kahan, and N. Treff, *Differentiation of stem cells to endoderm and pancreatic lineage*. 2009, Google Patents.

25. Chen, A.A., G.H. Underhill, and S.N. Bhatia, *Multiplexed, high-throughput analysis of 3D microtissue suspensions.* Integrative Biology, 2010. **2**(10): p. 517-527.

26. Furlong, E.E., D. Profitt, and M.P. Scott, *Automated sorting of live transgenic embryos.* Nat Biotechnol, 2001. **19**(2): p. 153-6.

27. Catteruccia, F., J.P. Benton, and A. Crisanti, *An Anopheles transgenic sexing strain for vector control.* Nat Biotechnol, 2005. **23**(11): p. 1414-7.

28. Sprando, R.L., et al., *A method to rank order water soluble compounds according to their toxicity using Caenorhabditis elegans, a Complex Object Parametric Analyzer and Sorter, and axenic liquid media.* Food Chem Toxicol, 2009. **47**(4): p. 722-8.

29. Wei, H., et al., *Particle sorting using a porous membrane in a microfluidic device.* Lab Chip, 2011. **11**(2): p. 238-45.

30. Nieuwstadt, H.A., et al., *Microfluidic particle sorting utilizing inertial lift force.* Biomedical Microdevices, 2011. **13**(1): p. 97-105.

31. Johansson, L., et al., *On-chip fluorescence-activated cell sorting by an integrated miniaturized ultrasonic transducer.* Anal Chem, 2009. **81**(13): p. 5188-96.

32. Huh, D., et al., *Gravity-driven microfluidic particle sorting device with hydrodynamic separation amplification.* Anal Chem, 2007. **79**(4): p. 1369-76.

33. Holmes, D., et al., *On-chip high-speed sorting of micron-sized particles for high-throughput analysis.* IEE Proc Nanobiotechnol, 2005. **152**(4): p. 129-35.

34. Applegate, R.W., Jr., et al., *Particle size limits when using optical trapping and deflection of particles for sorting using diode laser bars.* Opt Express, 2009. **17**(19): p. 16731-8.

35. Lillehoj, P.B., et al., *Continuous sorting of heterogeneous-sized embryoid bodies.* Lab Chip, 2010. **10**(13): p. 1678-82.

36. Denk, W., J.H. Strickler, and W.W. Webb, *Two-photon laser scanning fluorescence microscopy.* Science, 1990. **248**(4951): p. 73-6.

37. Squirrell, J.M., et al., *Long-term two-photon fluorescence imaging of mammalian embryos without compromising viability.* Nat Biotechnol, 1999. **17**(8): p. 763-7.

38. Centonze, V.E. and J.G. White, *Multiphoton excitation provides optical sections from deeper within scattering specimens than confocal imaging.* Biophys J, 1998. **75**(4): p. 2015-24.

39. Schenkeâ€□Layland, K., *Nonâ€□invasive multiphoton imaging of extracellular matrix structures.* Journal of biophotonics, 2008. **1**(6): p. 451-462.

40. Lisby, S., R. Gniadecki, and H.C. Wulf, *UV-induced DNA damage in human keratinocytes: quantitation and correlation with long-term survival.* Exp Dermatol, 2005. **14**(5): p. 349-55.

41. Campagnola, P.J. and L.M. Loew, *Second-harmonic imaging microscopy for visualizing biomolecular arrays in cells, tissues and organisms.* Nat Biotechnol, 2003. **21**(11): p. 1356-60.

42. Chen, X., et al., *Second harmonic generation microscopy for quantitative analysis of collagen fibrillar structure.* Nature Protocols, 2012. **7**(4): p. 654-669.

43. Bastiaens, P.I. and A. Squire, *Fluorescence lifetime imaging microscopy: spatial resolution of biochemical processes in the cell.* Trends in Cell Biology, 1999. **9**(2): p. 48-52.

44. Lakowicz, J.R., et al., *Fluorescence lifetime imaging.* Analytical Biochemistry, 1992. **202**(2): p. 316-30.

45. Wang, X.F., Periasamy, A., and Herman, B., *Fluorescence lifetime imaging microscopy (FLIM): instrumentation and applications.* Crit. Rev. Anal. Chem, 1992. **23**: p. 365-369.

46. Gadella, T.W.J., Jovin, T.M., and Clegg, R.M., *Fluorescence lifetime imaging microscopy (FLIM): Spatial resolution of microstructures on the nanosecond time scale.* Biophys. Chem, 1993. **48**: p. 221-239.

47. Stringari, C., et al., *Metabolic trajectory of cellular differentiation in small intestine by Phasor Fluorescence Lifetime Microscopy of NADH.* Sci Rep, 2012. **2**: p. 568.

48. Stringari, C., et al., *Label-free separation of human embryonic stem cells and their differentiating progenies by phasor fluorescence lifetime microscopy.* J Biomed Opt, 2012. **17**(4): p. 046012.

49. Squirrell, J.M., et al., *Endogenous fluorescence signatures in living pluripotent stem cells change with loss of potency.* PloS one, 2012. **7**(8): p. e43708.

50. Wright, B.K., et al., *NADH Distribution in Live Progenitor Stem Cells by Phasor-Fluorescence Lifetime Image Microscopy.* Biophysical journal, 2012. **103**(1): p. L07-L09.

51. Zhong, C.F., et al., *Quantitative two-photon flow cytometry--in vitro and in vivo.* J Biomed Opt, 2008. **13**(3): p. 034008.

52. Chang, Y.C., et al., *Fiber-optic multiphoton flow cytometry in whole blood and in vivo.* Journal of Biomedical Optics, 2010. **15**(4): p. 047004-047004-9.

53. He, W., et al., *In vivo quantitation of rare circulating tumor cells by multiphoton intravital flow cytometry.* Proceedings of the National Academy of Sciences, 2007. **104**(28): p. 11760-11765.

54. Dittrich, P.S. and P. Schwille, *An integrated microfluidic system for reaction, high-sensitivity detection, and sorting of fluorescent cells and particles.* Anal Chem, 2003. **75**(21): p. 5767-74.

55. Studer, V.J., R.; Pellereau, E.; Pepin, A.; Chen, Y., *A microfluidic mammalian cell sorter based on fluorescence detection.* Microelectronic Engineering 2004. **73**: p. 852-857.

56. Huh, D., et al., *Microfluidics for flow cytometric analysis of cells and particles.* Physiol Meas, 2005. **26**(3): p. R73-98.

57. Blake, A.J., et al., *Multilayer PDMS microfluidic chamber for controlling brain slice microenvironment.* Lab Chip, 2007. **7**(7): p. 842-9.

58. Yu, L., et al., *Simple, fast and high-throughput single-cell analysis on PDMS microfluidic chips.* Electrophoresis, 2008. **29**(24): p. 5055-60.

59. Haubert, K., T. Drier, and D. Beebe, *PDMS bonding by means of a portable, low-cost corona system.* Lab Chip, 2006. **6**(12): p. 1548-9.

60. Collins, T.J., *ImageJ for microscopy.* Biotechniques, 2007. **43**(1 Suppl): p. 25-30.

61. Lee, G.C., C.; Huang, S.; Yang, R., *The hydrodynamic focusing effect inside rectangular microchannels.* Journal of Micromechanical Microengineering, 2006. **16**: p. 1024-1032.

62. Miller-Hance, W.C., et al., *In vitro chamber specification during embryonic stem cell cardiogenesis. Expression of the ventricular myosin light chain-2 gene is independent of heart tube formation.* J Biol Chem, 1993. **268**(33): p. 25244-52.

63. Martinez-Fernandez, S., et al., *Pitx2c overexpression promotes cell proliferation and arrests differentiation in myoblasts.* Dev Dyn, 2006. **235**(11): p. 2930-9.

64. Fijnvandraat, A.C., et al., *Cardiomyocytes purified from differentiated embryonic stem cells exhibit characteristics of early chamber myocardium.* J Mol Cell Cardiol, 2003. **35**(12): p. 1461-72.

65. Ying, Q.L., et al., *BMP induction of Id proteins suppresses differentiation and sustains embryonic stem cell self-renewal in collaboration with STAT3.* Cell, 2003. **115**(3): p. 281-92.

66. Maltsev, V.A., et al., *Embryonic stem cells differentiate in vitro into cardiomyocytes representing sinusnodal, atrial and ventricular cell types.* Mech Dev, 1993. **44**(1): p. 41-50.

67. Berthier, E. and D.J. Beebe, *Flow rate analysis of a surface tension driven passive micropump.* Lab Chip, 2007. **7**(11): p. 1475-8.

68. White, J.G., J.M. Squirrell, and K.W. Eliceiri, *Applying multiphoton imaging to the study of membrane dynamics in living cells.* Traffic, 2001. **2**(11): p. 775-80.

69. Wokosin, D.L., et al., *Optical workstation with concurrent, independent multiphoton imaging and experimental laser microbeam capabilities.* Rev Sci Instrum, 2003. **74**(1): p. 193-201.

70. Bird, D.K., et al., *Simultaneous two-photon spectral and lifetime fluorescence microscopy.* Appl Opt, 2004. **43**(27): p. 5173-82.

71. Bird, D.K., et al., *Metabolic mapping of MCF10A human breast cells via multiphoton fluorescence lifetime imaging of the coenzyme NADH.* Cancer Res, 2005. **65**(19): p. 8766-73.

72. Gill, E.M., et al., *Relationship between collagen autofluorescence of the human cervix and menopausal status.* Photochem Photobiol, 2003. **77**(6): p. 653-8.

73. Provenzano, P.P., et al., *Nonlinear optical imaging and spectral-lifetime computational analysis of endogenous and exogenous fluorophores in breast cancer.* J Biomed Opt, 2008. **13**(3): p. 031220.

74. Skala, M.C., et al., *In vivo multiphoton microscopy of NADH and FAD redox states, fluorescence lifetimes, and cellular morphology in precancerous epithelia.* Proc Natl Acad Sci U S A, 2007. **104**(49): p. 19494-9.

75. Bayas, M.V., et al., *Lifetime measurements reveal kinetic differences between homophilic cadherin bonds.* Biophys J, 2006. **90**(4): p. 1385-95.

76. Haussinger, D., et al., *Proteolytic E-cadherin activation followed by solution NMR and X-ray crystallography.* EMBO J, 2004. **23**(8): p. 1699-708.

77. Kirkpatrick, N.D., M.A. Brewer, and U. Utzinger, *Endogenous optical biomarkers of ovarian cancer evaluated with multiphoton microscopy.* Cancer Epidemiol Biomarkers Prev, 2007. **16**(10): p. 2048-57.

78. Conklin, M.W., et al., *Fluorescence lifetime imaging of endogenous fluorophores in histopathology sections reveals differences between normal and tumor epithelium in carcinoma in situ of the breast.* Cell Biochem Biophys, 2009. **53**(3): p. 145-57.

79. Uchugonova, A. and K. Konig, *Two-photon autofluorescence and second-harmonic imaging of adult stem cells.* J Biomed Opt, 2008. **13**(5): p. 054068.

80. Guo, H.W., et al., *Reduced nicotinamide adenine dinucleotide fluorescence lifetime separates human mesenchymal stem cells from differentiated progenies.* J Biomed Opt, 2008. **13**(5): p. 050505.

81. Gong, J., et al., *Effects of extracellular matrix and neighboring cells on induction of human embryonic stem cells into retinal or retinal pigment epithelial progenitors.* Exp Eye Res, 2008. **86**(6): p. 957-65.

82. Evseenko, D., et al., *Identification of the Critical Extracellular Matrix Proteins that Promote Human Embryonic Stem Cell Assembly.* Stem Cells and Development, 2009. **18**(6): p. 919-927.

83. Di Carlo, D., et al., *Continuous inertial focusing, ordering, and separation of particles in microchannels.* Proceedings of the National Academy of Sciences, 2007. **104**(48): p. 18892.

84. Di Carlo, D., *Inertial microfluidics.* Lab Chip, 2009. **9**(21): p. 3038-46.

85. Gossett, D.R., et al., *Label-free cell separation and sorting in microfluidic systems.* Analytical and Bioanalytical Chemistry, 2010. **397**(8): p. 3249-3267.

86. Stathopoulos, N.A. and J.D. Hellums, *Shear stress effects on human embryonic kidney cells in Vitro.* Biotechnol Bioeng, 1985. **27**(7): p. 1021-6.

87. Augenstein, D.C., A.J. Sinskey, and D.I. Wang, *Effect of shear on the death of two strains of mammalian tissue cells.* Biotechnol Bioeng, 1971. **13**(3): p. 409-18.

88. McQueen, A.M., E; Bailey, JE, *Flow Effects on the Viability and Lysis of Suspended Mammalian Cells.* Biotechnology Letters, 1987. **9**(12): p. 831-836.

89. Lomholt, S., B. Stenum, and M.R. Maxey, *Experimental verification of the force coupling method for particulate flows.* International Journal of Multiphase Flow, 2002. **28**(2): p. 225-246.

90. Fortes, A.F., D.D. Joseph, and T.S. Lundgren, *Nonlinear Mechanics of Fluidization of Beds of Spherical-Particles.* Journal of Fluid Mechanics, 1987. **177**: p. 467-483.

91. Howell, P.B., Jr., et al., *Two simple and rugged designs for creating microfluidic sheath flow.* Lab Chip, 2008. **8**(7): p. 1097-103.

92. Takahashi, K. and S. Yamanaka, *Induction of pluripotent stem cells from mouse embryonic and adult fibroblast cultures by defined factors.* Cell, 2006. **126**(4): p. 663-676.

93. Thomson, J.A., et al., *Embryonic stem cell lines derived from human blastocysts.* Science, 1998. **282**(5391): p. 1145-1147.

94. Yu, J., et al., *Induced pluripotent stem cell lines derived from human somatic cells.* Science, 2007. **318**(5858): p. 1917-1920.

95. Shenghui, H., D. Nakada, and S.J. Morrison, *Mechanisms of stem cell self-renewal.* Annual Review of Cell and Developmental, 2009. **25**: p. 377-406.

96. Zhang, J., et al., *Extracellular matrix promotes highly efficient cardiac differentiation of human pluripotent stem cells: the matrix sandwich method.* Circ Res, 2012. **111**(9): p. 1125-36.

97. Zannettino, A.C.W., et al., *Specificity and functional effects of antibodies to human stem cell factor.* Growth Factors, 1997. **14**(1): p. 67-79.

98. Mohr, J.C., et al., *The microwell control of embryoid body size in order to regulate cardiac differentiation of human embryonic stem cells.* Biomaterials. **31**(7): p. 1885-1893.

99. Choi, Y.Y., et al., *Controlled-size embryoid body formation in concave microwell arrays.* Biomaterials. **31**(15): p. 4296-4303.

100. van Laake, L.W., et al., *Reporter-Based Isolation of Induced Pluripotent Stem Cell- and Embryonic Stem Cell-Derived Cardiac Progenitors Reveals Limited Gene Expression Variance.* Circulation Research, 2010. **107**(3): p. 340-347.

101. Schneider, C.A., W.S. Rasband, and K.W. Eliceiri, *NIH Image to ImageJ: 25 years of image analysis.* Nat Methods, 2012. **9**(7): p. 671-5.

102. Hsiao, E.C., et al., *Marking embryonic stem cells with a 2A self-cleaving peptide: a NKX2-5 emerald GFP BAC reporter.* PLoS One, 2008. **3**(7): p. e2532.

103. Bauwens, C.L., et al., *Control of human embryonic stem cell colony and aggregate size heterogeneity influences differentiation trajectories.* Stem Cells, 2008. **26**(9): p. 2300-2310.

104. Hwang, Y.S., et al., *Microwell-mediated control of embryoid body size regulates embryonic stem cell fate via differential expression of WNT5a and WNT11.* Proceedings of the National Academy of Sciences, 2009. **106**(40): p. 16978-16983.

105. Carpenedo, R.L., C.Y. Sargent, and T.C. McDevitt, *Rotary suspension culture enhances the efficiency, yield, and homogeneity of embryoid body differentiation.* Stem Cells, 2007. **25**(9): p. 2224-2234.

106. Lillehoj, P.B., et al., *Continuous sorting of heterogeneous-sized embryoid bodies.* Lab Chip. **10**(13): p. 1678-82.

107. White, J.G., W.B. Amos, and M. Fordham, *An evaluation of confocal versus conventional imaging of biological structures by fluorescence light microscopy.* J Cell Biol, 1987. **105**(1): p. 41-8.

108. Berg, S., R.L. Delude, and M.P. Fink, *Increased glycolysis maintains ATP levels after hypoxia and cytokine stimulation in rat enterocytes.* Intensive Care Medicine, 2002. **28**: p. S64-S64.

109. Wakita, M., G. Nishimura, and M. Tamura, *Some characteristics of the fluorescence lifetime of reduced pyridine nucleotides in isolated mitochondria, isolated hepatocytes, and perfused rat liver in situ.* J Biochem, 1995. **118**(6): p. 1151-60.

110. Blinova, K., et al., *Distribution of mitochondrial NADH fluorescence lifetimes: steady-state kinetics of matrix NADH interactions.* Biochemistry, 2005. **44**(7): p. 2585-94.

111. Belenky, P., K.L. Bogan, and C. Brenner, *NAD+ metabolism in health and disease.* Trends Biochem Sci, 2007. **32**(1): p. 12-9.

112. Chance, B., V. Legallais, and B. Schoener, *Metabolically linked changes in fluorescence emission spectra of cortex of rat brain, kidney and adrenal gland.* Nature, 1962. **195**: p. 1073-5.

113. Pappajohn, D.J., R. Penneys, and B. Chance, *NADH spectrofluorometry of rat skin.* J Appl Physiol, 1972. **33**(5): p. 684-7.

114. Zhang, B., et al., *Experimental study on plasticity of proliferated neural stem cells in adult rats after cerebral infarction.* Chin Med Sci J, 2006. **21**(3): p. 184-8.

115. Zhang, Q., D.W. Piston, and R.H. Goodman, *Regulation of corepressor function by nuclear NADH.* Science, 2002. **295**(5561): p. 1895-7.

116. Ramanujam, N., et al., *Cervical precancer detection using a multivariate statistical algorithm based on laser-induced fluorescence spectra at multiple excitation wavelengths.* Photochem Photobiol, 1996. **64**(4): p. 720-35.

117. Lakowicz, J.R., et al., *Fluorescence lifetime imaging of free and protein-bound NADH.* Proc Natl Acad Sci U S A, 1992. **89**(4): p. 1271-5.

118. Skala, M.C., et al., *Multiphoton microscopy of endogenous fluorescence differentiates normal, precancerous, and cancerous squamous epithelial tissues.* Cancer Res, 2005. **65**(4): p. 1180-6.

119. Doseff, A.I., *Apoptosis: the sculptor of development.* Stem Cells Dev, 2004. **13**(5): p. 473-83.

120. Meier, P., A. Finch, and G. Evan, *Apoptosis in development.* Nature, 2000. **407**(6805): p. 796-801.

121. Nicolaije, C., M. Koedam, and J.P. van Leeuwen, *Decreased oxygen tension lowers reactive oxygen species and apoptosis and inhibits osteoblast matrix mineralization through changes in early osteoblast differentiation.* J Cell Physiol, 2012. **227**(4): p. 1309-18.

122. Kawamura, T., et al., *Linking the p53 tumour suppressor pathway to somatic cell reprogramming.* Nature, 2009. **460**(7259): p. 1140-4.

123. Li, J., et al., *A novel method to inhibit apoptosis and promote differentiation of induced pluripotent stem cells in transplantation therapy for myocardial infarction.* Med Hypotheses, 2011. **76**(2): p. 264-5.

124. Marion, R.M., et al., *A p53-mediated DNA damage response limits reprogramming to ensure iPS cell genomic integrity.* Nature, 2009. **460**(7259): p. 1149-53.

125. Edel, M.J., et al., *Rem2 GTPase maintains survival of human embryonic stem cells as well as enhancing reprogramming by regulating p53 and cyclin D1.* Genes Dev, 2010. **24**(6): p. 561-73.

126. Zhao, Y., et al., *Two supporting factors greatly improve the efficiency of human iPSC generation.* Cell Stem Cell, 2008. **3**(5): p. 475-9.

127. Bieberich, E., et al., *Selective apoptosis of pluripotent mouse and human stem cells by novel ceramide analogues prevents teratoma formation and enriches for neural precursors in ES cell-derived neural transplants.* J Cell Biol, 2004. **167**(4): p. 723-34.

128. Ohgushi, M., et al., *Molecular pathway and cell state responsible for dissociation-induced apoptosis in human pluripotent stem cells.* Cell Stem Cell, 2010. **7**(2): p. 225-39.

129. Liang, J., et al., *Study the oxidative injury of yeast cells by NADH autofluorescence.* Spectrochim Acta A Mol Biomol Spectrosc, 2007. **67**(2): p. 355-9.

130. Levitt, J.M., et al., *Intrinsic fluorescence and redox changes associated with apoptosis of primary human epithelial cells.* J Biomed Opt, 2006. **11**(6): p. 064012.

131. Luger-Hamer, M., et al., *Renal viability evaluated by the multiprobe assembly: a unique tool for the assessment of renal ischemic injury.* Nephron Clin Pract, 2009. **111**(1): p. c29-38.

132. Yu, J.S., et al., *Increase of reduced nicotinamide adenine dinucleotide fluorescence lifetime precedes mitochondrial dysfunction in staurosporine-induced apoptosis of HeLa cells.* J Biomed Opt, 2011. **16**(3): p. 036008.

133. Guo, H.W., Y.H. Wei, and H.W. Wang, *Reduced nicotinamide adenine dinucleotide fluorescence lifetime detected poly(adenosine-5'-diphosphate-ribose) polymerase-1-mediated cell death and therapeutic effect of pyruvate.* J Biomed Opt, 2011. **16**(6): p. 068001.

134. Wang, H.W., et al., *Differentiation of apoptosis from necrosis by dynamic changes of reduced nicotinamide adenine dinucleotide fluorescence lifetime in live cells.* J Biomed Opt, 2008. **13**(5): p. 054011.

135. Su GC, W.Y., Wang HW, *NADH fluorescence as a photobiological metric in 5-aminolevlinic acid (ALA)-photodynamic therapy.* Optics Express, 2011. **19**(22).

136. Wang, H.W., Y.H. Wei, and H.W. Guo, *Reduced nicotinamide adenine dinucleotide (NADH) fluorescence for the detection of cell death.* Anticancer Agents Med Chem, 2009. **9**(9): p. 1012-7.

137. Ying, W., *NAD+/NADH and NADP+/NADPH in cellular functions and cell death: regulation and biological consequences.* Antioxid Redox Signal, 2008. **10**(2): p. 179-206.

138. Shapiro, A.M.J., et al., *Islet transplantation in seven patients with type 1 diabetes mellitus using a glucocorticoid-free immunosuppressive regimen.* New England Journal of Medicine, 2000. **343**(4): p. 230-238.

139. Shapiro, A.M.J., et al., *International trial of the Edmonton protocol for islet transplantation.* New England Journal of Medicine, 2006. **355**(13): p. 1318-1330.

140. Korsgren, O., et al., *Optimising islet engraftment is critical for successful clinical islet transplantation.* Diabetologia, 2008. **51**(2): p. 227-232.

141. MacGregor, R., et al., *Small rat islets are superior to large islets in in vitro function and in transplantation outcomes.* American Journal of Physiology-Endocrinology And Metabolism, 2006. **290**(5): p. E771-E779.

142. Kimple, M.E., et al., *Gαz negatively regulates insulin secretion and glucose clearance.* Journal of Biological Chemistry, 2008. **283**(8): p. 4560-4567.

143. Kimple, M.E., et al., *Deletion of GαZ Protein Protects against Diet-induced Glucose Intolerance via Expansion of β-Cell Mass.* Journal of Biological Chemistry, 2012. **287**(24): p. 20344-20355.

144. Dela Cruz, J.M., et al., *Feasibility of using multiphoton excited tissue autofluorescence for in vivo human histopathology*. Biomed Opt Express, 2010. **1**(5): p. 1320-1330.

145. Karaman, M.W., et al., *A quantitative analysis of kinase inhibitor selectivity.* Nat Biotechnol, 2008. **26**(1): p. 127-32.

146. Lakowicz, J.R., *Principles of Fluorescence Spectroscopy*. Third ed. 2006, New York: Springer. 954.

147. Huang, S., A.A. Heikal, and W.W. Webb, *Two-photon fluorescence spectroscopy and microscopy of NAD(P)H and flavoprotein.* Biophys J, 2002. **82**(5): p. 2811-25.

148. Vishwasrao, H.D., et al., *Conformational dependence of intracellular NADH on metabolic state revealed by associated fluorescence anisotropy.* J Biol Chem, 2005. **280**(26): p. 25119-26.

149. Yeh, W.C., et al., *FADD: essential for embryo development and signaling from some, but not all, inducers of apoptosis.* Science, 1998. **279**(5358): p. 1954-8.

150. Sheng, Z., et al., *Cardiotrophin 1 (CT-1) inhibition of cardiac myocyte apoptosis via a mitogen-activated protein kinase-dependent pathway. Divergence from downstream CT-1 signals for myocardial cell hypertrophy.* J Biol Chem, 1997. **272**(9): p. 5783-91.

151. Poelmann, R.E., et al., *Apoptosis in cardiac development.* Cell Tissue Res, 2000. **301**(1): p. 43-52.

152. Durrans, A. and H. Stuhlmann, *A role for Egfl7 during endothelial organization in the embryoid body model system.* J Angiogenes Res, 2010. **2**: p. 4.

153. Shukla, S., et al., *Synthesis and organization of hyaluronan and versican by embryonic stem cells undergoing embryoid body differentiation.* J Histochem Cytochem, 2010. **58**(4): p. 345-58.

154. Mochizuki, H., Y. Ohnuki, and H. Kurosawa, *Effect of glucose concentration during embryoid body (EB) formation from mouse embryonic stem cells on EB growth and cell differentiation.* J Biosci Bioeng, 2011. **111**(1): p. 92-7.

155. Takei, S., et al., *Bone morphogenetic protein-4 promotes induction of cardiomyocytes from human embryonic stem cells in serum-based embryoid body development.* Am J Physiol Heart Circ Physiol, 2009. **296**(6): p. H1793-803.

156. Lund, A.W., et al., *The natural and engineered 3D microenvironment as a regulatory cue during stem cell fate determination.* Tissue Eng Part B Rev, 2009. **15**(3): p. 371-80.

157. Lutolf, M.P., P.M. Gilbert, and H.M. Blau, *Designing materials to direct stem-cell fate.* Nature, 2009. **462**(7272): p. 433-41.

158. Heikal, A.A., *Intracellular coenzymes as natural biomarkers for metabolic activities and mitochondrial anomalies.* Biomark Med, 2010. **4**(2): p. 241-63.

159. Hronik-Tupaj, M., et al., *Osteoblastic differentiation and stress response of human mesenchymal stem cells exposed to alternating current electric fields.* Biomed Eng Online, 2011. **10**(1): p. 9.

160. Konig, K., A. Uchugonova, and E. Gorjup, *Multiphoton fluorescence lifetime imaging of 3D-stem cell spheroids during differentiation.* Microsc Res Tech, 2011. **74**(1): p. 9-17.

161. Rice, W.L., D.L. Kaplan, and I. Georgakoudi, *Two-photon microscopy for non-invasive, quantitative monitoring of stem cell differentiation.* PLoS One, 2010. **5**(4): p. e10075.

162. Rice, W.L., D.L. Kaplan, and I. Georgakoudi, *Quantitative biomarkers of stem cell differentiation based on intrinsic two-photon excited fluorescence.* J Biomed Opt, 2007. **12**(6): p. 060504.

163. Reyes, J.M., et al., *Metabolic changes in mesenchymal stem cells in osteogenic medium measured by autofluorescence spectroscopy.* Stem Cells, 2006. **24**(5): p. 1213-7.

164. Wang, J., et al., *Dependence of mouse embryonic stem cells on threonine catabolism.* Science, 2009. **325**(5939): p. 435-9.

165. Cho, Y.M., et al., *Dynamic changes in mitochondrial biogenesis and antioxidant enzymes during the spontaneous differentiation of human embryonic stem cells.* Biochem Biophys Res Commun, 2006. **348**(4): p. 1472-8.

166. Ezashi, T., P. Das, and R.M. Roberts, *Low O2 tensions and the prevention of differentiation of hES cells.* Proc Natl Acad Sci U S A, 2005. **102**(13): p. 4783-8.

167. Kondoh, H., et al., *A high glycolytic flux supports the proliferative potential of murine embryonic stem cells.* Antioxid Redox Signal, 2007. **9**(3): p. 293-9.

168. Francis, K.R. and L. Wei, *Human embryonic stem cell neural differentiation and enhanced cell survival promoted by hypoxic preconditioning.* Cell Death Dis, 2010. **1**(2): p. e22.

169. Buschke DG, H.D., Wliceiri KW, Ogle BM, *Screening Approaches for Stem Cells*, in *Stem Cell-Based Tissue Repair*, R.S. R Goradetsky, Editor. 2010, RSC Publishing. p. 55-140.

170. Shapiro, A., et al., *Islet transplantation in seven patients with type 1 diabetes mellitus using a glucocorticoid-free immunosuppressive regimen.* New England Journal of Medicine, 2000. **343**(4): p. 230.

171. Unger, R.H., *The milieu interieur and the islets of Langerhans.* Diabetologia, 1981. **20**(1): p. 1-11.

172. Le Marchand, S.J. and D.W. Piston, *Glucose suppression of glucagon secretion: metabolic and calcium responses from alpha-cells in intact mouse pancreatic islets.* J Biol Chem, 2010. **285**(19): p. 14389-98.

173. Le Marchand, S.J. and D.W. Piston, *Glucose decouples intracellular ca(2+) activity from glucagon secretion in mouse pancreatic islet alpha-cells.* PloS one, 2012. **7**(10): p. e47084.

174. Patterson, G.H., et al., *Separation of the glucose-stimulated cytoplasmic and mitochondrial NAD (P) H responses in pancreatic islet β cells.* Proceedings of the National Academy of Sciences, 2000. **97**(10): p. 5203-5207.

175. Sharma, N. and N.A. Patankar, *A fast computation technique for the direct numerical simulation of rigid particulate flows.* Journal of Computational Physics, 2005. **205**(2): p. 439-457.

176. Uhlmann, M., *An immersed boundary method with direct forcing for the simulation of particulate flows.* Journal of Computational Physics, 2005. **209**(2): p. 448-476.

177. Zoumi, A., A. Yeh, and B.J. Tromberg, *Imaging cells and extracellular matrix in vivo by using second-harmonic generation and two-photon excited fluorescence.* Proceedings of the National Academy of Sciences, 2002. **99**(17): p. 11014-11019.

178. Liu, H., et al., *Myofibrillogenesis in live neonatal cardiomyocytes observed with hybrid two-photon excitation fluorescence-second harmonic generation microscopy.* J Biomed Opt, 2011. **16**(12): p. 126012.

179. Xie, J., J. Ferbas, and G. Juan, *Three-Dimensional Second-Harmonic Generation Imaging of Fibrillar Collagen in Biological Tissues.* Current Protocols in Cytometry, 2012: p. 6.33. 1-6.33. 11.

180. Baraniak, P.R. and T.C. McDevitt, *Scaffold-free culture of mesenchymal stem cell spheroids in suspension preserves multilineage potential.* Cell and Tissue Research, 2012. **347**(3): p. 701-711.

181. Stendahl, J.C., D.B. Kaufman, and S.I. Stupp, *Extracellular matrix in pancreatic islets: relevance to scaffold design and transplantation.* Cell Transplant, 2009. **18**(1): p. 1-12.